TECHNISCHE UNIVERSITÄT MÜNCHEN
FAKULTÄT FÜR INFORMATIK

Lehrstuhl für Echtzeitsysteme und Robotik

Compliant Modular Worm-like Robotic Mechanisms with Decentrally Controlled Fluid Actuators

Martin Eder

Vollständiger Abdruck der von der Fakultät für Informatik der Technischen Universität München zur Erlangung des akademischen Grades eines

Doktor-Ingenieurs (Dr.-Ing.)

genehmigten Dissertation.

Vorsitzender:	Univ.-Prof. Bernd Brügge, Ph.D.
Prüfer der Dissertation:	1. Univ.-Prof. Dr.-Ing. habil. Alois Knoll
	2. Univ.-Prof. Dr.-Ing. habil. Boris Lohmann

Die Dissertation wurde am 22.09.2014 bei der Technischen Universität München eingereicht und durch die Fakultät für Informatik am 12.03.2015 angenommen.

Abstract

Whereas in the past, robotics was mainly an issue within industrial environments, today robots advance more and more into everyday scenarios which deal with human interaction. Thus the question about safe human-robot cooperation and solutions for how to solve this issue arise. Two different strategies to come up with human-friendly behavior are currently being pursued.

First, a control system can be implemented which tries to guarantee anthropomorphic system properties. These active stiffness systems are based on adequate control algorithms assuring that the movements of all joints of the robot cannot hazard anybody in its workspace. Therefore, usually additional sensors, such as second rotary encoders, force and torque sensors or even tactile sensors, are utilized. The idea behind this kind of setup is that the power supply of the robot is partially limited such that the human is not injured in case of contact.

Second, a compliant robot can be built if components are used that have a severely limited stiffness, i.e. a mechanical support structure combined with drive elements that are already flexible due to their material. In this context, pneumatic artificial muscles (PAMs) are a comparably cost-efficient way to meet the demands in terms of safety, as already mentioned before. Due to their elastic properties, an inherently soft robotic arm can be set up which is automatically safe in terms of human-robot interaction regulations. However, the challenging part of the control of these flexible actuators is their nonlinear characteristics.

Ensuing from that position, this thesis introduces novel robotic mechanisms that are inherently compliant, but have numerous advantages compared to state-of-the-art constructions. The crucial contribution of this work is the development of machinery that are based on a centrally fed actuator arrangement, which makes them comparatively easy to control with precision. Moreover, the developed prototypes have clearly defined mechanical, electrical and software interfaces that lead to enhanced modularity. As a matter of principle, the developed compliant mechanisms can be used for safe applications of human-robot interaction.

Zusammenfassung

Während in der Vergangenheit Robotik hauptsächlich in industriellen Umgebungen vorzufinden war, werden Roboter heutzutage zunehmend in alltäglichen Einsatzszenarien mit menschlicher Interaktion eingesetzt. Demzufolge erhebt sich die Frage nach einem sicheren Zusammenspiel von Mensch und Roboter und nach der Lösung dieses Problems. Zwei verschiedene Strategien werden derzeit verfolgt, um menschenfreundliches Verhalten abzubilden.

Einerseits kann eine Ansteuerung aufgesetzt werden, welche menschenfreundliche Systemeigenschaften garantiert. Solche Systeme mit aktiver Steifigkeit basieren auf entsprechenden Kontrollalgorithmen, die dafür Sorge tragen, dass die Bewegungen sämtlicher Gelenke des Roboters niemanden innerhalb seines Arbeitsraumes gefährden können. Dabei werden üblicherweise zusätzliche Sensoren wie etwa Drehgeber, Kraft-Momenten-Sensoren oder sogar taktile Sensoren eingesetzt. Die Idee hinter dieser Art Aufbau ist, dass die Leistung des Roboters teilweise limitiert wird, so dass der Mensch im Falle eines Kontakts bzw. einer Kollision nicht verletzt wird.

Andererseits kann ein nachgiebiger Roboter aufgebaut werden, indem Komponenten eingesetzt werden, welche eine stark begrenzte Steifigkeit aufweisen, d.h. eine mechanische Stützstruktur gepaart mit Antriebselementen, die materialbedingt flexibel sind. In diesem Zusammenhang stellen künstliche pneumatische Muskeln eine kosteneffiziente Lösung dar, um die zuvor bereits erwähnten Anforderungen hinsichtlich Sicherheit zu erfüllen. Aufgrund ihrer elastischen Eigenschaften kann ein inhärent nachgiebiger Roboterarm konzipiert werden, welcher Richtlinien zur Sicherheit bei der Mensch-Roboter-Interaktion einhält. Die Herausforderung bei der Steuerung dieser flexiblen Aktoren ist jedoch deren nichtlineare Charakteristik.

Von diesem Standpunkt ausgehend stellt diese Arbeit neuartige Roboter-Mechanismen vor, welche inhärente Nachgiebigkeit und zahlreiche Vorteile gegenüber den Konstruktionen aus dem Stand der Technik aufweisen. Entscheidendster Aspekt im Rahmen dieser Arbeit ist die Entwicklung von Mechanismen, welche auf eine zentrale Versorgung der Aktoren beruhen und dabei eine vergleichsweise einfache und präzise Ansteuerung ermöglichen. Die entwickelten Prototypen besitzen klar definierte mechanische, elektrische und softwaretechnische Schnittstellen, so dass eine ausgeprägte Modularität resultiert. Prinzipbedingt können die entwickelten nachgiebigen Mechanismen entsprechend innerhalb Applikationen mit Mensch-Roboter-Interaktion eingesetzt werden.

Acknowledgments

I gratefully acknowledge the contribution of Robotics Technology Leaders GmbH München for technical and financial support, Festo AG and Co. KG Esslingen for the donation of PAMs, and ams AG for the donation of rotary encoders.

Moreover, this thesis would not have been possible without the encouragement of Prof. Dr.-Ing. Alois Knoll and Dr. Stefan Riesner. Special thanks goes to Maximilian Karl, Felix Schultheiß, Johannes Schürmann and Markus Händl who also gave invaluable support during various stages of the development work.

I also thank Dr. Gerhard Schrott, Marie-Luise Neitz and Dr. Reinhard Lafrenz for administrative support during the years at the chair for robotics and embedded systems.

Lastly, my thanks go to my colleague M. Ali Nasseri for all the substantive debates and to Richard Haensch for his manufacturing capabilities in the RBG workshop of TUM Informatics Department.

Contents

List of Figures

List of Tables

Chapter 1

Introduction

The field of robotics is undergoing rapid change, widening to new areas with different requirements regarding system behavior, and consequently pushing up sales numbers. According to reports from 2012 [67], worldwide industrial robot sales in 2011 rose by 38 % compared with the previous year. This level, the highest peak since 1961, was driven by the automotive and electronics industries, mainly located in Europe and Asia, with Japan and Republic of Korea leading the way. Reports from 2013 [70] indicated the second highest number of robots sold. Within Europe, Germany is the largest robot market, and so it plays an important role in robotics-related domains. A worldwide average growth of about 6 % per year was estimated for the years between 2014 and 2016, which shows a continued increase but lower growth rates. As stated above, the field of robotics changes in terms of both applications and system behavior. Service robotics and flexible manipulators become more and more important. The following sections intend to identify this change in application scenarios and reveal their challenges, in particular safety problems that are coupled with these issues. The technical problem itself is also defined. Furthermore, specific terms are declared in order to come up with a common linguistic basis for a better understanding. An outline of the thesis concludes this initial chapter.

1.1 Development in robotics

Besides purely industrial applications, the field of service robotics is on the rise as well. In 2011 the number of professional service robots increased by 9 %, which means total sales of 16,408 units [68]. This number remained pretty stable within 2012. The sales could reach a number of about 16,100 units. In spite of the current dominance of military applications, there is a growth in areas such as medical robotics (e.g. robot assisted surgery manipulators), robots for logistics (e.g. automated guided vehicles) and robots for personal and domestic use (e.g. handicap assistance robots, entertainment robots, robots for personal transportation or lawn-mowing robots). About 94,800 new service robots for professional use and approximately 22 million units of service robots for personal use will be installed according to projections for the years 2013 to 2016 [69]. It seems there is a growing market for service robotics in various young fields of applications, and these applications mainly deal with the interaction between man and machine. If there is such an interaction, this always raises the question about safety. The problem is that originally robots were utilized for industrial purposes in an

appropriate environment, and usually there is a strict separation between the robot and the operators.

This separation is not feasible if it comes to robots in human environments. Accordingly, the way robots are to be designed, is completely different from merely industrial robots. In order to be sure that the robot behaves safely, particular attention has to be paid to collision scenarios in case of system failure. Here, the compliant property of the robotic system is a fundamental issue. If the human interacts with automatic machines, such as robots, there is always a risk that in case of unforeseen movements of either man or error-prone machine motion, collisions with conceivably serious hazard might occur. Correspondingly, it is necessary to put emphasis on safety of the system in order to minimize the extent of the aforementioned dangers, or even to remove them completely.

1.1.1 Possible application scenarios

Based on the aforementioned changes, the use of compliant robotic mechanisms ranges from industrial domains and service-oriented fields to housekeeping areas. Within industrial applications for instance, such manipulations can be extended to technical hollows. Also inspection applications in unstructured environments are relevant scenarios for such mechanisms. Compared to rigid robotic systems, flexible manipulators have advantages if winding areas or areas with many obstacles have to be reached. Besides maneuvers in hollows, the focus is on applications that deal with the interaction between the human and said mechanism. One example of such an interaction is the collaboration mode, in which the human and the manipulator fulfill common tasks, e.g. order picking. Within housekeeping applications, service robotics is a core topic, in which safe integration into a human-oriented environment must be guaranteed. More details about possible scenarios are addressed in the separate Chapter 7, which shows the spectrum of the novel robot type that is developed within the framework of this thesis.

1.1.2 Safety issues

Industrial robots are usually installed inside safety fences that guarantee separation of human and machine. This approach is not feasible for humanoid robots aiming towards real interaction [128]. According to present regulations, robotic arms for human-robot interaction mustn't exceed an overall end-effector velocity of 250 mm/s, which limits the working speed rigorously. It seems that there is a need for new standardizations and alternative methods to result in a safe human-robot interaction. Currently various standardization projects in robotics are in progress. Safety regulations for robots dealing with the presence of humans are more and more pushed, since there is a growing market for mobile robots, collaborative robots or service robots in general. Within the norm ISO 10218-2[1] [25] general statements are written down, and the technical specification ISO/TS 15066[2] already reveals details about the collaboration between human and robot. The prEN ISO 13482[3] [26] sets new standards for mobile service robots, motion supporting robots and personal care robots of the non-medical fields. ISO 8373[4] [72] extends

[1] robots and robotic devices – safety requirements for industrial robots – part 2: robot systems and integration
[2] robots and robotic devices – collaborative industrial robots
[3] robots and robotic devices – safety requirements for non-industrial robots – non-medical personal care robot
[4] robots and robotic devices – vocabulary

current robotics vocabulary with terms for service robotics and related fields. According to section 1.1 there is a growing market for service robotics. Safety issues are decisive factors in order to carry on developments in this field. This trend corresponds with broadening of appropriate regulations to define and handle the problems, which service robotics brings in its wake.

1.2 Technical problem and definitions

Considering the aforementioned challenges in robotics of section 1.1 and 1.1.2, the change in robotics, from systems with protective fences to open systems that allow interaction with humans, demands new strategies to overcome the problem of safety. The resulting technical problem is to find robotic solutions that meet the demands of upcoming standards for safe human-robot interaction and collaboration. Currently, there is a trade-off between precision and compliance [156]. Hence, interaction with a human is always related to a reduction of stiffness of the robotic joints or even links, which again usually causes problems related to precision. The idea of compliance in technical sense is two-fold. Passive compliance is correlated to a behavior that is independent of sensory feedback, whereas active compliance explicitly deals with sensory feedback (cf. [72], paragraph 5.3.9). In the two subsections below, the technical background problem of this active and passive compliance is given, which is additionally broadened by a set of definitions of relevant specific terms, mainly being originated in flexible or service robotics and safety domain.

1.2.1 Active and passive compliance

To get a broader knowledge about active and passive compliance, the following subsection gives an overview about the problems related to these topics. Active compliance in the field of robotics deals with force or force-torque sensors that influence the robot's behavior. According to the specific interaction of human and robot, different sensors are necessary. In the simplest case, this force or force-torque sensor is located between the robot's flange and its end-effector. Once the end-effector hits a human, the sensor data are analyzed and adequate control commands are sent to the robot controller in order to limit the current for its drives, and simultaneously restrict the forces and torques that can be applied. As a slight variation of this method the end-effector might be equipped with such a sensor. For instance, the fingers of a gripper have additional sensors to measure the gripping forces. In case that the forces exceed a set threshold, e.g. if a human puts his fingers in between the jaws and the gripper starts closing, the robot control diminishes the power for the end-effector.

Despite its effectiveness, the strategy of active compliance implicates several problems in terms of costs and efforts for integration. The costs for force, torque or even combined force-torque sensors depend on the specific boundary conditions, such as dimensions and amount of force or torque that should be measured. The average costs for one sensor range from a few hundred Euros up to a few thousand Euros. Additionally to the direct costs for the sensors, expenses for mechanical integration have to be considered, such as for manufacturing of adapter plates etc. If such sensors are only attached to the robot's flange, this adaption is quite simple, whereas the integration within existing robotic joints is extremely complex. To change the setup of every joint of the robot, each shaft has to be adapted and most probably the housing must be modified

– all under consideration of already installed components, e.g. encoders, bearings or brake units.

In contrast to the previously described scenario, passive compliance of robots goes without an additional integration of sensors. The concept of passive compliance is based on a flexible structure of the robot [57]. Structure in this context can either mean the driving elements or the supporting structure. Pneumatic actuators are promising means for use as inherently compliant driving elements. If costs and energy effectiveness are decisive prerequisites, pneumatic artificial muscles are a reasonable solution that have several advantages compared to standard pneumatic cylinders. In subsection 2.1.3, more detailed explanations are given to prove the aforementioned hypothesis.

1.2.2 Definition of robot-specific terms

As mentioned in subsection 1.1.2, the terminology of the following thesis accords with the declarations of ISO 8373 in order to guarantee a transparent and common understanding. The most important standard terms are defined in the upper part of Table 1.1. As far as special technical terms with a certain meaning used in this thesis are concerned, further specific declarations are given in the lower section of Table 1.1.

By means of the aforementioned set of vocabulary, together with what can be found in ISO 8373, specific crucial technical terms are completely defined. Other terms with only local scope are declared in the corresponding paragraphs where they are used.

1.3 Outline of the thesis

This thesis develops and investigates two prototypes of worm-like robotic mechanisms that are inherently compliant and use pneumatic artificial muscles (PAMs) as driving elements. The focal point of this work is to implement and evaluate the control of the novel mechanisms. Within the control system, the main challenge is to design both adequate pressure and position control loops. Chapter 1 gives a short introduction, including current changes and challenges in robotics, as well as a definition of the research problem together with relevant terms and definitions, and ends with an outline of the thesis. In Chapter 2 the state of the art and state of research are discussed, highlighting both compliant actuator and mechanism concepts, limitations and thus reasons and requirements for the development of new mechanisms. The prototypical implementation approach is discussed in Chapter 3, where an initial worm-like robotic mechanism is presented that constitutes the basic idea, structure and starting point. Also within this chapter all the details of the mechanical construction and hardware layout of two final prototypes of such robots are shown with integrated actuators and sensors. Aspects of kinematics and dynamics comprising motion analysis of both prototypes are covered and investigated in Chapter 4, and Chapter 5 presents the control of the mechanisms. The latter chapter concerns control strategy, calibration of the driving elements, control of pressure, angle and forces, as well as issues about the concrete implementation of the control hardware architecture. Due to embedded hardware limitations, the computational effort is a crucial factor for the choice of an adequate control design. Within Chapter 6 experimental verification results are exposed.

Table 1.1: Robot-specific terms

Standard terms	*Description*
Manipulator	Mechanism comprising several segments moving relative to one another, being utilized for moving or gripping objects ([72], paragraph 2.1)
Robot	Mechanism with actuators, moveable in more than one degree of freedom (DOF), being controlled autonomously without man's help ([72], paragraph 2.6)
Industrial robot	Robot with at least three axes ([72], paragraph 2.9)
Collaboration	Task fulfilled by both human and robot ([72], paragraph 2.21)
Compliance	Soft behavior of a robot if exterior forces are applied ([72], paragraph 5.3.9)
Specific Terms	*Description*
Worm-like mechanism	Mechanism that has a shape similar to a worm and can bend in multiple directions (about certain axes of rotation). Like invertebrate animals it is meant to be a tubular structure that has actuators in longitudinal direction. In contrast to real worms, the term in the context used in this thesis shouldn't change its overall diameter or fulfill a peristaltic motion. Instead, there is only an expansion and contraction of flexible actuators that cause overall bending motions in several directions. It is similar to the idea of having several segments serially arranged, actuated by fluid chambers.
Worm-like robotic mechanism	Extension of worm-like mechanism that can be controlled autonomously without man's help. It uses various sensors to gain system states in order to control actuators properly.
Discrete worm-like robotic mechanism	Prototype of a worm-like robotic mechanism that is based on a rigid frame backbone and stiff joints that connect all of the robots' segments, such that an overall discrete curvature of the entire system results (with two degrees of freedom (DOF) per segment).
Continuum worm-like robotic mechanism	Further prototype of a worm-like robotic mechanism which is characterized by bending segments that do not require any rigid support structure between supporting discs, such that the robot results in an arched structure that can bend, expand and shorten.
Cardan joint	Coupling between two rigid rods that allows to rotate in two degrees of freedom (DOF). Also known as a universal joint.
Compliant actuator	Actuator that is characterized by soft behavior according to the term "compliance" as explained above. Usually its stiffness can be adjusted.
PAM/PAMs	Pneumatic artificial muscle is a pneumatic actuator that shortens when filled with air (plural: pneumatic artificial muscles).

Test scenarios and their evaluations are considered in addition to the experimental setup. Further, a comparison of decentral vs. central feed arrangement of the setup finishes this chapter. In a subsequent Chapter 7 application scenarios are revealed to give an estimation about the impact of the novel robotic mechanisms, as introduced before. The last Chapter 8 closes the thesis and reveals conclusions and future work. Figure 1.1 summarizes the synoptic view of the thesis.

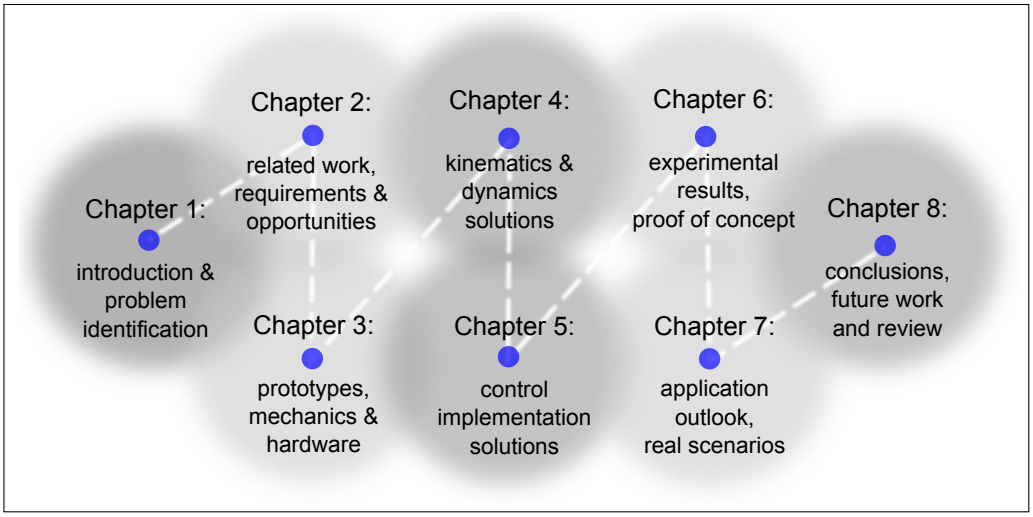

Figure 1.1: Synoptic view

Chapter 2

Related work

There are a number of robotic systems offering compliant behavior, using either adequate control strategies [10, 82, 88] to make the system soft or utilizing compliant components for the structure and actuators [57, 58, 114, 131]. Provided that low costs, low energy consumption and low weight as well as intrinsic softness of the actuators are prerequisites, PAM actuators are appropriate means for driving such inherently compliant mechanisms. Compared to commercially available electric drives, PAMs are preferable on all of the above measures.

First, compliant actuators as the most important sub-components of a flexible robotic mechanism are considered. In a second step, some relevant state-of-the-art mechanisms – complete setups – are highlighted. In further steps, features and disadvantages of the state of the art as well as the state of research are presented. Finally, requirements for the development of a new mechanism and opportunities for such a pneumatically controlled robot are discussed.

2.1 Compliant actuators

Besides the supporting structure of a system, the actuators play the most decisive role to guarantee mechanically soft behavior. In particular it is interesting to adjust the stiffness of the actuators according to the needs of specific applications, such as within a safe human-robot interaction. Different kinds of compliant actuators can be distinguished, which shall be covered shortly in the next paragraphs. One principal distinctive feature is active and passive compliance, which means that either a mechanically stiff actuator is controlled such that it is flexible, or the actuator itself already contains elastic components to be compliant. Van Ham et al. differentiate between equilibrium-controlled, antagonistic-controlled, structure-controlled and mechanically controlled stiffness, corresponding examples are given in [57].

2.1.1 Classical electric actuators

Electric actuators for use in mechatronic servo systems, such as robots, are widely spread, and consequently electric drives are subject to a long history of research, developments and improvements. In particular, servo system control aspects are very well investigated and there is a huge variety of methods (e.g. see [111]). However, if it comes to compliant behavior,

more sophisticated implementations become relevant. To make conventional electric actuators flexible, two ways are possible. A first option is that active compliance strategies have to be implemented in the control of the actuators. The motor itself is stiff, i.e. the controller imitates soft behavior of a spring [1]. Another option is adding a flexible element to the actuator, e.g. fixing a spring in series with an electric motor, which results in a system comprising a predefined compliance. Figure 2.1 shows such a motor and spring system, in which the changing length of the spring is used to measure the force F. An enhanced version of this setup is called equilibrium-controlled stiffness, where the equilibrium position of the spring is varied by control law, thus adjusting the compliance concurrently [57].

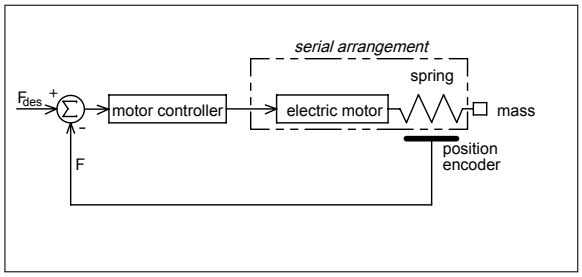

Figure 2.1: Motor and spring system

Regarding the variety and availability of electric motors that can be used for robots, there is an extremely broad range. There is virtually no maximum size limit, for instance if AC motors with three-phase connection are considered. However, the problem is to find small and lightweight motors with high torque or output force. Also there is always the question about efficiency and costs. Table 2.1 presents an overview about which electric motors are utilized for robots according to the current state of research.

Table 2.1: Electric drives used for robots

AC servo drives
DC servo drives
Torque drives
Stepper motors
Piezoelectric drives
Voice coil motors
Synchronous linear motors

Most of the research and industrial robots, e.g. articulated arms, are equipped with rotary AC servo drives, normally permanently energized synchronous motors. For identification of some robotic drive data, current servo motor product portfolios of Yaskawa, Mitsubishi Electric, Fanuc, and Siemens are investigated. To define a maximum limit, Kuka's KR 1000 1300 Titan PA and Fanuc's M-2000iA/1200, which are known to be the robots with the largest payload available worldwide, are considered. The minimum limit, in terms of industrial robots, is defined by wrist drives of small robots, such as the Mitsubishi RV-2AJ. Besides regular size AC servo drives, there are mini series on the market, such as the Yaskawa Sigma-5 mini series with only 15 mm flange size, 3.3 W and 17 bit absolute encoder.

If it comes to mobile robotic applications, DC servo drives become more interesting. Currently, only a few commercial robots are available that are based on DC technology, such as the Kuka youBot. However, in research very many little robots are equipped with DC drives, as they are less dangerous to integrate. There are also brushless torque DC drives available as very compact and lightweight types, such as the ones developed by Deutsches Zentrum für Luft- und Raumfahrt (DLR), named Robodrive. These drives are highly efficient hollow-shaft DC brushless motors. They can be optionally used as direct drive torque motors without gearboxes. Within robotics, the main application of these motors is the equipment of the Kuka LBR4+ and Kuka iiwa robot arms (cf. section 2.2). When large robots should be equipped with DC drives, normally brushless DC high torque motors are utilized, but these motors already need very high voltage far above 24 V and are comparably heavy. As an example for either part handling or studio automation, a robotic system called MM-800, which is based on a Kuka KR 16-2 KS[1], was modified to DC torque motor technology, such that the entire mobile platform can be run with a DC power supply.

Stepper motors are another means in order to move robotic joints. They are based on synchronous brushless DC drives, and mainly used for small and medium size robots that don't have to handle much payload. Since it is possible to use them for positioning tasks without additional sensors, research setups often integrate these cost-efficient motors.

Occasionally even piezoelectric motors occur in the robotic sector, in cases where high precision is necessary. The main advantages of these drives are compactness and micro- or even nanometer precision, but the main drawback is that standard piezo stacks have very short travel or rotation capability. Applications are basically high precision academic applications, e.g. positioning stages, such as the ones supplied by Physik Instrumente (PI) GmbH & Co. KG[2]. Also there are niche applications, for instance surgical robots, that use piezoelectric stages [112, 113].

Another niche technology is the use of voice coil motors for robots, mainly for applications with linear movements, but they are also available for rotary applications. Similar to piezoelectric motors, these motors are only utilized in few research robots [105].

All of the motors mentioned above are principally available both in rotary and linear motion technology. There are already quite a lot of linear synchronous servo motors on the market that can directly generate linear motions, but in many cases, additional elements, such as spindles, are attached to rotary drives. Most of the motors described need to be coupled with gearboxes in order to reach reasonable force/torque and speed. In the robotic segment, precision gearboxes, e.g. strain wave gearing, cyclo or eccentric drive gears, planetary gears or belts, are the most common gear mechanisms, which are supplied by companies such as Harmonic Drive, Sumitomo, Nabtesco, and Alpha Wittenstein.

Table 2.2 summarizes a comparison of the motors discussed above, giving some estimations about which dimension, force/torque, power and weight ranges are typically used within electric drives for robots.

[1] cf. url: http://www.neobotix-roboter.de/industrieroboter-mm-800.html, last accessed: September 6, 2013

[2] cf. url: http://www.physikinstrumente.de/de/produkte/nanopositionierung/index.php, last accessed: September 6, 2013

Table 2.2: Comparison of typical electric drives for robots

Type	*Cross section/ diameter*	*Rated torque/ force*	*Power*	*Weight*	*Example*
AC servo drives	40x40-90x190 mm	0.159-27 Nm	50-8500 W	0.3-40 kg	Kuka KK67Y-YYYY-050
DC servo drives (brushless)	6-60 mm	0.251 mNm-0.75 Nm	1.2-400 W	2.8 g-2.45 kg	Maxxon EC 310599
Lightweight torque DC drives (brushless)	25-115 mm	0.024-11.2 Nm	60-880 W	0.016-2.17 kg	Robodrive 25 (TQ-Group)
Torque motor	150-565 mm	9-6300 Nm (max. 15-13800 Nm)	1900-6600 W	3.05-320 kg	Bosch Rexroth IndraDyn T MST130A-0200
Stepper	20-86 mm	0.014-9.2 Nm	n/a	0.31-2.85 kg	Orientalmotor PKP213U05A
Piezoelectric motor	17x8.8-60x16 mm	3-5 N	n/a	13-216 g	SmarAct SLC 1720
Voice coil motor	9.5-95.3 mm	0.28-117.7 N	1.8-75 W	6.3 g-4.77 kg	Moticont LVCM-010-013-01
Linear synchronous motor	15x51-61x260 mm	6-21500 N	n/a	0.1-75 kg	Bosch Rexroth MCP015A-L040

2.1.2 Conventional fluid actuators

Standard fluid actuators, such as pneumatic or hydraulic cylinders, offer flexibility, since their fluid is compressible to a certain degree. Especially pneumatic cylinders can be considered as springs, as the air contained in the cylinder is highly compressible. A change in compliance can be realized by changing the pressure within the actuator [157]. Fluid cylinders can be divided into single-acting and double-acting cylinders, which means the controllability for movements in one or two directions. Provided that position encoders are in the control-loop, servo-pneumatic or servo-hydraulic systems result. Figure 2.2 depicts a fluid cylinder control of this kind. There is always some friction between the sealing of the piston and the cylinder wall, that's why such systems usually suffer from stick-slip effect, unless huge effort for elimination has been made. Pneumatic and hydraulic actuators work with different pressures, thus resulting forces vary extremely.

Below, first hydraulic and in a second step pneumatic actuators shall be discussed. Hydraulic actuators usually work in an operating pressure range up to about 420 bar [73]. This allows quite a lot of applications that demand very high forces, such as within construction industry. The va-

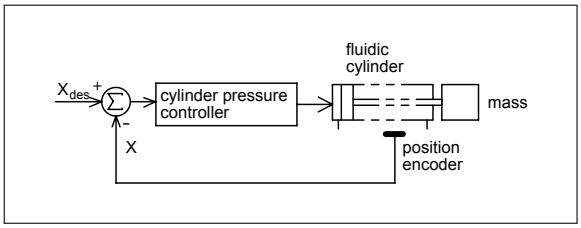

Figure 2.2: Control of fluid cylinders

riety of typically available hydraulic actuators is shown in Table 2.3. In most of the applications, standard single-rod cylinders are installed. Telescopic cylinders with up to 10 stages are interesting, if extreme stroke length is required. Plunger cylinders are actuators that don't include a piston, which is instead substituted by the rod itself. In this manner, it is easy to provide even hollow plunger cylinders. Plunger cylinders are relevant in cases of particular cost-effective applications. Dependent on specific needs within concrete applications, customized solutions of micro- and large cylinders are utilized.

Table 2.3: Types of hydraulic actuators

Single-rod cylinder
Double-rod cylinder
Telescopic cylinder
Plunger cylinder
Micro-cylinder
Large cylinder

The characteristics of the hydraulic cylinders from Table 2.3 are presented in another Table 2.4, which highlights the specification of each of the hydraulic cylinders. This table already indicates that the power or force and the weight of such a cylinder are extremely high.

In contrast to hydraulic actuators, pneumatic actuators have a standard operating pressure that is much lower. This pressure determines the power of the pneumatic system. In principle, the pressure can be chosen arbitrarily, but usually only a pressure up to 10 bar is utilized. More pressure results in more expensive components and more loss of energy. High pressure actuators with a maximum operating pressure of more than 16 bar are available for special applications, but 5-6 bar is the most economic pressure range. Various types of pneumatic actuators can be found in the state of the art, which could be principally installed in robots (cf. Table 2.5).

Within each of these pneumatic actuator types, there is a wide range of features in terms of dimensions, forces, and weights. Table 2.6 provides a summary of different feature ranges of the pneumatic actuator types mentioned in Table 2.5. This overview is based on typical actuator types as they can be found on the market. Without any claim to completeness, the data for this table are based on values from different significant supply companies. It can be easily seen from Table 2.6 that pneumatic artificial muscles (PAMs) are by far the most lightweight and efficient actuators. To estimate the efficiency of these actuators, which are chosen for the robotic prototypes developed within this thesis, Table 2.7 shows a direct comparison to state-

Table 2.4: Comparison of typical hydraulic cylinders

Type	*Diameter piston*	*Force*	*Pressure*	*Travel*	*Weight*	*Example*
Single-rod cylinder	25-320 mm	7.85 (160 bar)-2815 kN (350 bar)	0-350 bar	0-6000 mm	1-7317 kg	Bosch Rexroth CDL2
Double-rod cylinder	25-200 mm	7.85 (160bar)-660 kN (210 bar)	0-210 bar	0-3000 mm	1.0-1226 kg	Bosch Rexroth CDT3
Telescopic cylinder (up to 10 stages)	30-265 mm	7.2-1120 kN (395 bar)	0-395 bar	410-4650 mm	14-314 kg	Agirossi ETZ-K
Plunger cylinder	20-320 mm	5.03-2574 kN	0-320 bar	custom-ized	n/a	PPT Cilindri type P
Micro-cylinder	8-25 mm	1.01 (200 bar)-5.89 kN (200 bar)	0-200 bar	0-500 mm	n/a	Agirossi Mikro Z
Large cylin-der	custom-ized	custom-ized	custom-ized	custom-ized	custom-ized	Bosch Rexroth

of-the-art pneumatic actuators available on the market. In contrast to the comparison before, Table 2.7 is already limited to specific force and dimension values, such that it is possible to adequately study the actuators. The forces and dimensions are chosen to meet the requirements as described later on in 2.4. The Festo DMSP-10-160N-RM-CM artificial muscles, being utilized for the prototypes here, serve as a reference object with their maximum force of 630 N and a maximum stroke of 40 mm. Standard cylinders and compact cylinders need much larger cross sections in order to reach the same force. The air pressure exerts uniformly on all sides of the rubber material of the PAMs, whereas the active part of cylinders is reduced to the piston surface. Particularly interesting are extremely lightweight 3D printed plastic cushions, for example integrated in Festo's robot arm Bionic Handling Assistant BHA, which is introduced later on in section 2.2. More about the muscles used for the robotic prototypes of this thesis can be found in subsection 2.1.3. Table 2.7 already expressed that the force of standard pneumatic actuators is rather limited, or, in other words, the installation space is comparably large. The idea is quite straightforward to use thin cylinders that are applied with higher pressure. The downside of this tactic is that high pressure (pressure $>$10 bar) means components that are used for heavy industry purposes. These components are more expensive, much heavier and larger. The main problems are caused by the valves that can be found on the market. Small and lightweight valves are only available for a pressure $\leq$10 bar. Also there is always the question about adequate compressors, fittings, and hoses for different kinds of pressure ranges. In this sense, the limit for the presented setup is a maximum operating pressure of 10 bar. Table 2.8

Table 2.5: Types of pneumatic actuators [6]

Standard norm cylinders
Compact cylinders
Flat cylinders
Short stroke cylinders
Diaphragm cylinders (thrusters)
Rodless cylinders
High power cylinders
Hydropneumatic cylinders
Bellows cylinders
Pneumatic artificial muscles (PAMs)
3D printed plastic cushions

presents an overview of pneumatics components with respect to availability for different operating pressure ranges. Compared to ”standard” components, ”beyond standard” components are not widely available and more expensive, whereas ”industrial” components are rare and even more costly.

Last but not least, it is reasonable to sum up and evaluate the different actuator types. The main idea here is to have an estimation of how pneumatic actuators, as utilized for the robotic prototypes of this thesis, differentiate in contrast to electric and hydraulic drives. This way, the assumption of choosing pneumatic actuators as reasonable, highly efficient compliant actuators can be confirmed (cf. Table 2.9 and Figure 2.3). It appears that pneumatic actuators have a very good force-to-weight ratio and hydraulic actuators are best in terms of force-to-dimension ratio. However, electric drives are comparable heavy and large in relation to their power.

2.1.3 Pneumatic artificial muscles

Pneumatic artificial muscles (PAMs) are among the most appropriate actuators for use in an antagonistic-controlled compliant setup. The idea of coming up with an artificial muscle, which has quite similar features as the human muscle, was already born in the 1950s, known as the McKibben muscle (formerly patented by Richard H. Gaylord, Clevite Corp., depicted in Figure 2.4 [51]).

The gist of this invention is an elastomer tube surrounded by a braided sheath made of fabrics with high tensile stiffness. All sheath fibers are arranged in an angular or rhombic configuration. Once the elastomer tube is filled with compressed air, the diameter of the tube enlarges, whereas the length of the muscle shortens[3]. The change in length is exploited to generate a tension force.

[3]McKibben muscles with a mesh angle $\alpha < 54°44'$ contract on pressurization, whereas the ones with a mesh angle $\alpha > 54°44'$ extend [151]

Table 2.6: Comparison of typical pneumatic drives

Type	*Diameter piston*	*Force*	*Pressure*	*Travel*	*Weight*	*Example*
Round/norm cylinders	2.5-320 mm	1.9-48 380 N (6 bar)	3.5-7 bar/0-10 bar	1-2000 mm	0.002-53.2 kg	Festo EG-2,5-5-PK-2
Compact cylinders	12-125 mm	51-7363 N (6 bar)	2.5-10 bar	0-500 mm	0.077-8.7 kg	Festo ADN-12-5-A-P-A
Flat cylinders	1.5x6.5 mm (rectangular)-63 mm	3-1870 N (6 bar)	1-10 bar	1-1000 mm	0.004-9.7 kg	Festo EZH-1,5/6,5-10
Short stroke cylinders	4-100 mm	4.9-4712 N (6 bar)	1.5-10 bar	2.5-25 mm	0.004-2.75 kg	Festo ADVC-4-2,5-P
Diaphragm cylinders	52.5-115 mm	1363-6543 N (6.3 bar)	0.03-8 bar	40-95 mm	1.6-5.8 kg	Bosch Rexroth RDC
Rodless cylinders	16-80 mm	127-3146 N (6.3 bar)	2-8 bar	0-9900 mm	0.45-85 kg	Bosch Rexroth RTC
High power cylinders	25-100 mm	542-18 281 N (6 bar)	0.6-10 bar	0-150 mm	n/a	Festo ADHN
Hydro-pneumatic cylinders	40-80 mm	0-3000 N (7 bar)	0-7 bar	0-500 mm	n/a	Specken Drumag HPL80
Bellows	145-640 mm	1.1-197 kN (6 bar)	0-8 bar	34-580 mm	1.1-28.5 kg	Bosch Rexroth BCP
Pneumatic artificial muscles (PAMs)	5-40 mm	0-6000 N (6 bar)	0-8 bar	4-4250 mm	0.01-3.7 kg	Festo DMSP-40-9000-RM-CM

Table 2.7: Comparison of possible pneumatic actuators for worm-like robotic mechanism

	Air muscles	*Cylinders*	*Compact cylinders*	*High force cylinders*	*Hydro-pneumatic cylinders*	*Bellows cylinders*	*3D printed cushions*
Type	Festo DMSP-10-160N-RM-CM	Festo DNSU-32-40-P	SMC CD55B32-40	Festo ADNH-25-40-A-P-A-4N	Specken Drumag HPL-B40	Bosch Rexroth BCP-90	Festo BHA
Diameter (piston)	10 mm	32 mm	32 mm	25 mm	40 mm	90 mm	variable
Overall diameter/edge length	22 mm	42 mm	46 mm	40 mm	70 mm	160 mm	variable
Travel	40 mm	40 mm	40 mm	40 mm	40 mm	50 mm	variable
Weight	72 g	433 g	406 g	n/a	n/a	900 g	variable
Max. pressure	8 bar	10 bar	10 bar	10 bar	10 bar	8 bar	3 bar
Max. force (8 bar)	630 N	643 N	643 N	1381 N	870 N	7333 N	variable
Max. force	630 N (8 bar)	804 N (10 bar)	804 N (10 bar)	1727 N (10 bar)	1110 N (10 bar)	7333 N (8 bar)	n/a
Length	253 mm	192 mm	110 mm	317 mm	386 mm	50 mm	variable
Approx. price	69 Euro	54 Euro	54 Euro	255 Euro	n/a	184 Euro	variable

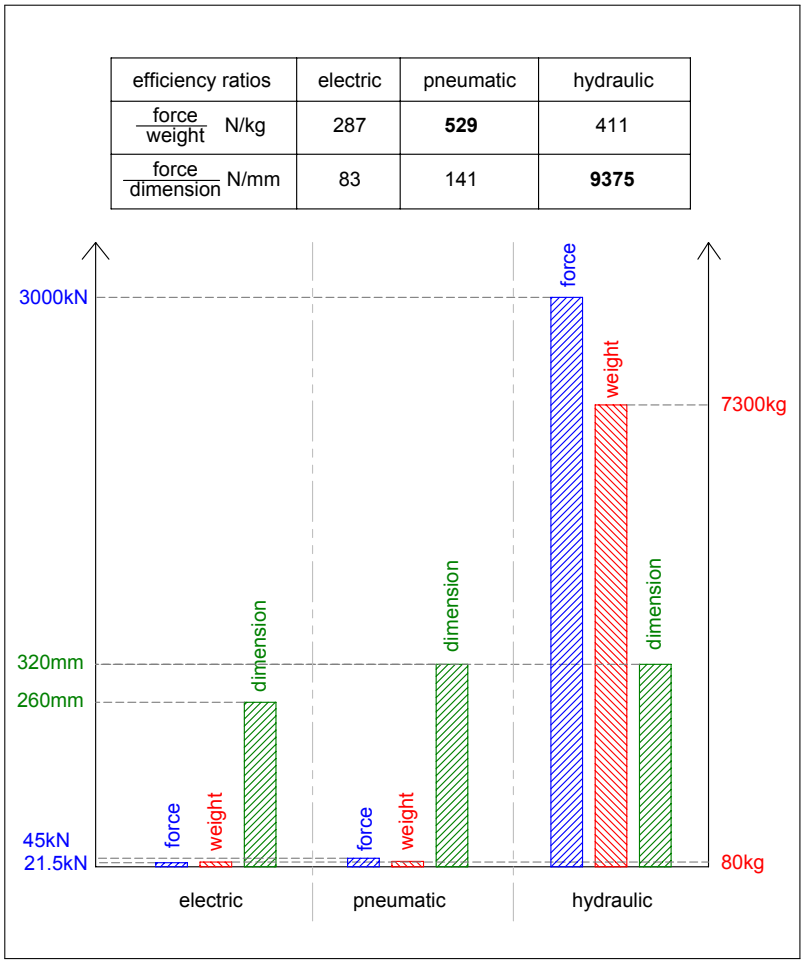

Figure 2.3: Efficiency of different actuators

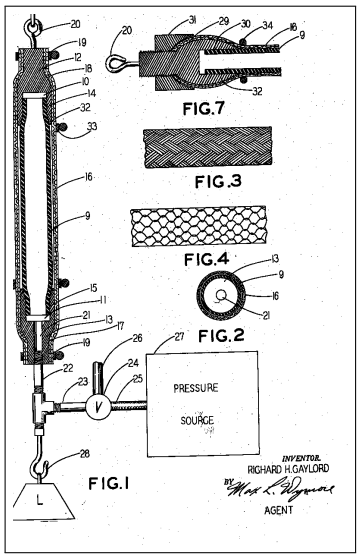

Figure 2.4: Fluid actuated motor system and stroking device, US2844126A [51]

Table 2.8: Available pneumatics components

Pressure	$\leq$ *6bar*	$\leq$ *8bar*	$\leq$ *10bar*	$\leq$ *12bar*	$\leq$ *16bar*	$>$ *16bar*
Compressor	standard	standard	beyond standard	beyond standard	beyond standard	industrial
Valves	standard	standard	standard	industrial	industrial	industrial
Cylinders	standard	standard	standard	beyond standard	beyond standard	industrial
Fittings	standard	standard	standard	beyond standard	beyond standard	industrial
Hoses	standard	standard	standard	standard	beyond standard	industrial
Component size	small	small	small	large	large	large
Component price	economic	economic	economic	high	high	high

Figure 2.5 illustrates the working principle of PAMs. An elastic tube (middle part) is linked to two outer flange mounts, e.g. made of aluminum (initial setting with black dashed lines in Figure 2.5). When pressurized air is filled into the tube, the diameter enlarges. Due to the fibers that are either integrated in the tube or surround the tube as a sheath, an axial contraction results (inflated setting with solid lines in Figure 2.5). This shortening causes pulling forces at each end of the muscle, where the flange mounts are located and power is transmitted. In contrast to conventional pneumatic cylinders, the air pressure not only affects the piston area, but it affects the entire hollow body of the tube including both the tube wall and the circular area at each end of the muscle. Consequently, the overall efficiency of such a PAM is much higher.

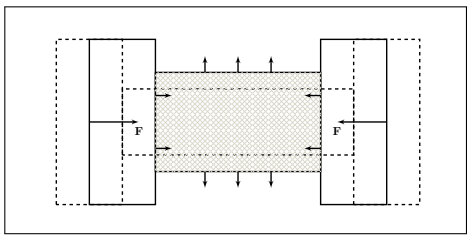

Figure 2.5: Shortening of muscle

The first PAMs were developed some decades ago, and there is a huge variety of different kinds of muscles. In 1999 Daerden categorized various artificial muscles [20]. The following Table 2.10 shows the overview of this plurality, summing up Daerden's results.

Artificial muscles can be distinguished according to their principle of operation – pneumatic or hydraulic. Hydraulic artificial muscles feature much higher rigidity, and PAMs have advantages if scenarios with compliance are regarded. Most of the muscles have a membrane that can expand, but there are also some types that have a folded membrane, which is able to unfold

Table 2.9: Comparison of different types of actuators

Feature	*Electric*	*Pneumatic*	*Hydraulic*
Dimensions (diameter)	6-565 mm	2.5-320 mm [19]	8-320 mm (and more)
Forces/Torques	0.25 mN m-13 800 N m, alternatively 6-21500 N	2-45 000 N (6 bar) [19]	3000 kN (600 bar) [108], even 1000 bar (mining industry [36])
Velocities	diverse	0.1-1.5 m/s (even 10 m/s [56])	0.5 m/s typically
Linear travel	mostly needs additional components	easy realization, high forces	easy realization, high forces
Stiffness	good	problematic (compressible fluid)	good (incompressible fluid)
Accuracy	$\pm$1 µm [108]	$\pm$1 µm [108]	1/10 mm [108]
Power density	less good [36]	good [27, 36]	very good [36]
Advantages	no need of compressor/pump, very high accuracies possible	air is well available, easy storage, clean, cheap components, high velocities	high energy density
Disadvantages	small power-to-weight ratio	compression of air, forces limited, noise, usually only up to 10 bar	leakage, high pressure (danger), dependent on temperature (viscosity)

if it is filled. According to Daerden another very decisive characteristic is the arrangement of the membrane relative to the fibers. Braided sheath muscles are made of an elastic inner tube, surrounded by a woven sleeve that consists of a fiber which is not flexible. For instance, McKibben [51] and Beullens [9] yielded such types. Currently, Shadow Robot Company, England, is among the most important suppliers to put such actuators on the market, named *air muscles* [54]. Netted muscles in contrast have a sheath which has much less density, i.e. fewer fibers, usually combined with an unfolding membrane type. Examples for such a shaping are the Yarlott type or Immega & Kukolj muscle (also called Romac muscle) [71, 159]. Last but not least, there is the embedded muscle version, which is characterized in that the membrane and the fibers are melted within one single layer. Muscles built by Morin [110], Baldwin [5], or highly developed state-of-the-art muscles, such as the Festo ”Fluidic Muscle”, can be given as examples for this group of muscles. For the latter, Festo AG & Co. KG applied for an intellectual property right in 1999, claiming an actuating means that enhances state-of-the-art PAMs, wherein the hose body comprises two strand groups being in a crossover configuration, and an intermediately yielding material is located between the first and the second strand groups, such

Table 2.10: Classification of artificial muscles [20]

Principle of operation	pneumatic	hydraulic	
Membrane type	expanding	unfolding	
Arrangement of membrane/fibers	braided sheath	netted	embedded
notations	McKibben, Beullens	Yarlott, Immega & Kukolj	Morin, Baldwin

that a constant distance is maintained (cf. Figure 2.6). This invention reduces friction between the strand groups and consequently increases the efficiency and durability.

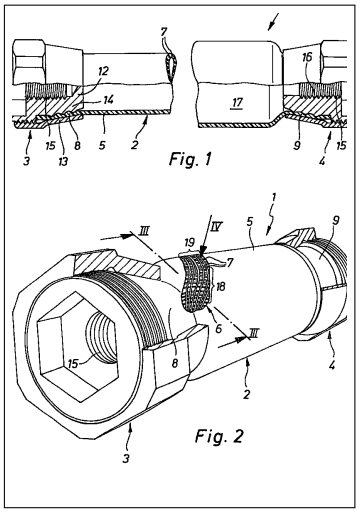

Figure 2.6: Actuating means, US6349746B1 [8]

2.2 Compliant mechanisms

This section gives an overview about relevant compliant mechanisms according to both the state of research and state of the art. Complete setups are described, which are actuated by pneumatic or electric drives, or even combinations of these two types of drives. Various mechanisms with different sizes of discrete and continuum style representations are covered.

At the Artificial Intelligence Laboratory of Stanford University, California, a human-friendly robot was developed, including both PAMs and electric motors to drive the joints [28, 141]. Due to its high control frequency of the electric drives, the performance is very good. The drawback is the integration of additional electric drive units, which increase cost, weight and development effort.

Hildebrandt et al. presented a robot with two degrees of freedom (DOF), driven by four artificial muscles [65]. The robot was developed by the Institute of Automation and Systems Engineering

TU Ilmenau, Germany, in cooperation with Festo AG & Co. KG. It consists of a flat articulated system that can move in a plane. Hence, motion capability is strongly restricted.

Another already commercially available compliant robotic arm based on pneumatic muscles is ROMO by FerRobotics Compliant Robot Technology GmbH, Austria (cf. Figure 2.7). This arm comprises three interlinked actively pivoted levers with three parallel PAMs each [39]. The basic system has five DOF in total, realized by means of two ball-and-socket joints with two DOF each (one DOF is fixed mechanically) and one cylindrical axle with one DOF. All control valves are allocated at the basement of the robot in a common valve cluster.

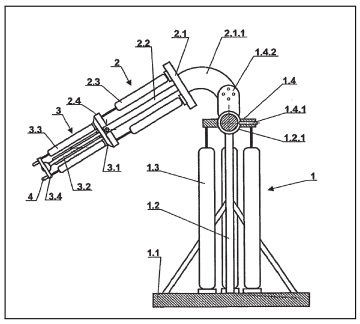

Figure 2.7: ROMA by FerRobotics, US2009/0182436A1 [39]

Besides flexible pneumatic robots, there are also robots mainly built for industry, which are based on electric drives, and integrate a force control mode, such that soft behavior of the mechanism can be ensured. The Deutsches Zentrum für Luft- und Raumfahrt (DLR) developed an articulated robot with seven DOF that is sold as the ”LBR4+” by Kuka Roboter GmbH (cf. Figure 2.8) [2]. Most recently Kuka Roboter GmbH announced the successor, which is an enhanced version of the ”LBR4+”, named ”iiwa” [11, 85], and which is meant to enter new markets that demand sensitiveness and compliance. This robot is based on stiff actuators (servo motors) with additional torque sensors and output side encoders. It can be controlled in a force mode that enables human collaboration with corresponding compliance features. The system is quite high-priced, since components and integration of this sophisticated system deals with vast effort.

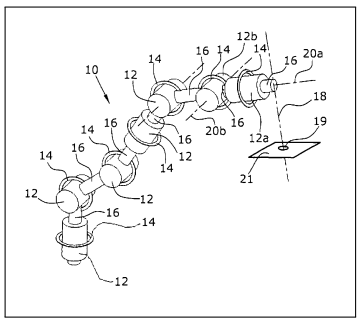

Figure 2.8: Lightweight Robot by DLR, US7,646,161B2 [2]

Both UR5 and UR10 robots by Universal Robots, Odense, Denmark, are lightweight constructions that offer safe and human-friendly solutions, usable for direct human-robot interaction (cf. Figure 2.9) [82]. Velocities and masses of the joints of the robot are comparably low, which ensures save behavior even with inflexible actuators. Universal Robots integrated both an en-

coder at the input side of the motor and an encoder at the output side of each joint, such that it is possible to detect forces or torques by calculating the error between these two encoder values.

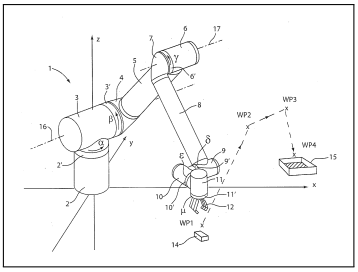

Figure 2.9: UR by Universal Robots, WO2007/099511A2 [82]

Further, Tetra Gesellschaft für Sensorik, Robotik und Automation GmbH, Ilmenau, introduced a flexible robot, named BioRob, suitable for small-scale applications (cf. Figure 2.10) [80, 89]. This articulated arm comprises four elastic joints driven by electric motors. The elasticity comes from bowden cables with integrated spring couplings. In order to get the real position of each joint, there is an absolute encoder mounted at the joint's output side, additionally to a normal encoder on the motor shaft, which is mounted at the input side. Due to the nonlinear force-distance characteristics of the utilized spring couplings, the control of the arm is not trivial. The position accuracy is in the range of 1 mm.

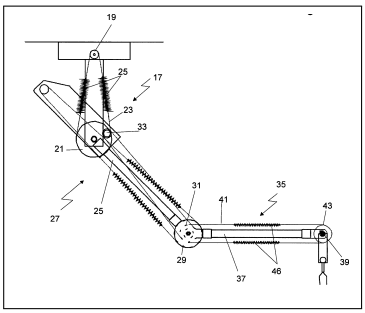

Figure 2.10: BioRob by Tetra GmbH, US2011/0266508A1 [80]

Beyond the already presented mechanisms, it is worth mentioning some more interesting examples of uncommercial compliant mechanisms of the state of research.

The first one is the actuator system with artificial air muscles by Shadow Robot Company Ltd., London, UK (cf. Figure 2.11) [55]. This anthropomorphic actuator research prototype is basically a hand/arm mechanism with highly flexible muscles.

A second setup is an arrangement named Airic's arm by Festo AG & Co. KG, again driven by pneumatic artificial muscles [42]. This arm includes 32 muscles with various sizes, which is interesting in terms of control and dealing with a large number of pneumatic actuators.

ECCEROBOT[4] is a third example, which is driven by conventional DC motors. It is a robot developed within the EU Seventh Framework Programme for Research[5] [74, 75, 124]. This setup

[4] Embodied Cognition in a Compliantly Engineered Robot
[5] ICT-Challenge 2, Cognitive Systems, Interaction, Robotics

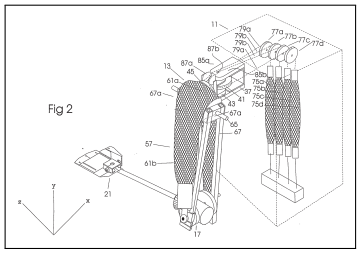

Figure 2.11: Actuator system by Shadow Robot Company Ltd., WO03/74238A1 [55]

is based on a plastic skeleton that is actuated by DC motors with gearboxes. Dyneema lines together with elastic shock cords are coupled to the drives to result in compliant behavior.

All of the aforementioned mechanisms are characterized in that they are based on stiff support structures. The joints are arranged in a serial kinematics with rigid links in between. Consequently, the mechanisms have a defined geometry that can only be influenced by actuated joints, which usually rotate the links attached. Besides robots with rigid supporting structures, there are also continuum style robots that are completely flexible in terms of both actuation and structural design.

A continuum style manipulator geared towards the media was built by Festo AG & Co. KG, named Bionic Handling Assistant BHA, which is based on the topology of an elephant's trunk. It unifies compliance and high maneuverability within a 3D printed plastic structure. All supporting elements of the manipulator are utilized as actuators at the same time. The arrangement is highly flexible due to three bendable parallel strands that are mounted serially to each other (cf. Figure 2.12) [49]. Except for some sensors, all control devices, in particular the valves, are located in a central basis. The valve cluster consists of large proportional directional control valves, type Festo VPWP, each 132 mm $\times$ 60 mm $\times$ 74 mm and 0.8 kg. Compared to its overall weight of 1.8 kg, the payload of 0.5 kg is high. Its positioning accuracy is in the range of 10 mm. The main drawback of this manipulator is its oscillation tendency.

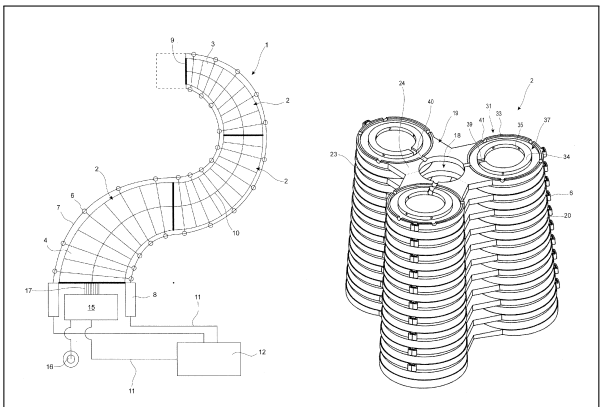

(a) Bionic Handling Assistant, Festo, US2012/0210818A1 [49]

(b) One segment of Bionic Handling Assistant, Festo, US2012/0210818A1 [49]

Figure 2.12: Bionic Handling Assistant by Festo AG & Co. KG

Besides the BHA, Festo AG & Co. KG filed some more utility models and patents in the domain

of manipulators, such as the ones depicted in Figure 2.13. The Bionic Tripod 3.0 [46] is a manipulator that has four bars made of spring steel, which are moved electro-pneumatically. The moving structure is able to bend and lift (cf. Figure 2.13(a)). X and y motions are in the range of $\pm$500 mm, vertical z motions of up to 300 mm are feasible. The overall handling capacity is about 400 g. Furthermore, Festo AG & Co. KG presented a modular drive device (cf. [76]) that is movable in three dimensions, which is based on 3D printed plastic parts (cf. Figure 2.13(b)). The new idea here is that each of the single modules can actively move in two opposite directions, and the modules can be attached to one another in various ways resulting in mechanisms that are able to extend and retract in 3D space. A similar device compared to the aforementioned BHA is the Slim Slime Robot by Aoki et al. [3, 4], which has pneumatic bellows made of metal that are additionally guided by wires (so-called *Bridle Drives*).

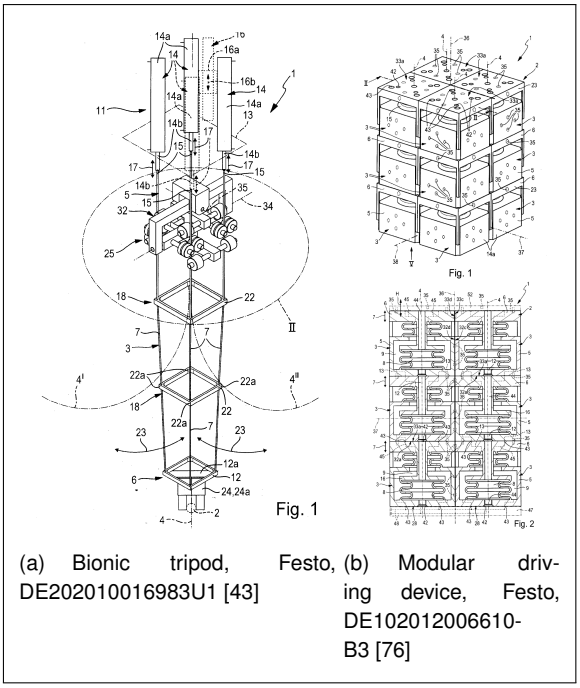

(a) Bionic tripod, Festo, DE202010016983U1 [43]

(b) Modular driving device, Festo, DE102012006610-B3 [76]

Figure 2.13: Manipulators by Festo AG & Co. KG

Supplementary to what was described before, highly innovative robots were developed by Whitesides Research Group of Harvard University, Cambridge. These small soft pneumatic robots, composed of extremely flexible elastomeric polymers, can generate crawling movements and undulation. The overall length of the robot is approximately 160 mm, the velocity can reach up to about 26 mm/s [140]. Operated with a pressure of less than 0.7 bar, it cannot carry any payloads, but move its own weight. Similar to this approach a soft robot based on fluidic elastomer actuators was developed at the Massachusetts Institute of Technology, Cambridge [117]. The special characteristic here is a pneumatic battery for portable pressure generation.

Furthermore, recent robotics research also deals with the imitation of octopus arms. A two-arm underwater octopus robot made of rubber was built by Greek developers [139]. However, this kind of robot uses standard DC drives to actuate the system. In contrast, the robot by the IIT, Italy [104], utilizes shape memory alloy coils to drive the flexible arm, and the octopus by Calisti et al. [12] is moved by steel and Dyneema cables, which are again actuated by means of external DC motors.

Last but not least, McMahan et al. [106] designed a pneumatic contractor-muscle based continuum trunk manipulator, named Octarm (cf. also [7]). The limitation is the central placement of all valves at a common basement, which causes modularity issues in case of higher numbers of segments.

2.3 Evaluation of state of research

Considering the current state of research as already shown in the previous sections 2.1 and 2.2, different kinds of compliant actuators and mechanisms are available. There are several ways to implement compliance, and it seems plausible that the systems have both advantages and disadvantages in diverse fields. One cannot distinguish between the right or the wrong actuators and mechanisms, there are always dependencies, such as the concrete boundary conditions. The following section intends to give an overview to estimate the value of the features as well as limitations or weaknesses of compliant actuators and mechanisms of the state of the art and state of research.

If classical electric actuators are integrated, either elastic elements have to be utilized together with an adequate control or a very complex control imitating compliance has to be implemented, usually combined with additional sensors. The costs for electric motors are not very high due to mass production. Further integration effort and expenses are caused by the use of elastic elements and specialized sensors. In case of an actuator without elastic elements, there is still the problem that compliance cannot be guaranteed if the control fails. Hence, more effort has to be made to result in fault tolerance.

Conventional fluid actuators are a practical way of embedding flexibility, especially if pneumatic systems are considered. Fluid cylinders are robust, mechanically simple and comparably cheap (cf. [64]), only the integration together with valves, pumps etc. might be a cost-driver. Such cylinders normally suffer from stick-slip effect, which influences the performance of the setup. However, the main advantage is that the stiffness of the actuators can be adjusted continuously without the necessity of adding components. As cylinders are made of rigid material, primarily steel, the actuators or their supporting structures do not behave completely flexible. They might still cause severe damage in case of collision with other objects or humans.

The crucial benefits of PAMs are their elastic behavior and their high power-to-weight ratio compared to conventional fluid actuators. Acquisition costs are less than in the previous case of standard fluid drives. The drawback of these drives is that they always have to be arranged in an agonist and antagonist setup, such that movements both back and forth can be realized. Precise control of these PAMs requires a pre-calibration of the muscles, and reaching an accurate position is hard to achieve with conventional control methods.

Regarding the mechanisms of section 2.2, offering soft characteristics, the next paragraph reveals their features as well as their limitations.

Hybrid mechanical systems comprising pneumatic and electric actuators within one setup, such as the one presented by Stanford University, can maneuver quite precisely, but the control and integration effort is enormous, which again affects the costs. The simple experimental mechanism introduced by Hildebrandt and the TU Ilmenau only allows motions in a plane, thus this mechanism can just be regarded as a reference platform for estimating the control quality. In contrast, the Bionic Handling Assistant is a potent mechanism with high power-to-weight ratio.

As mentioned before, the position accuracy is in the range of 10 mm, which can be regarded as the limit of the system. The commercially available system ROMA implicates a PAM driving technology that enables inherent force measurement and compliance. The position accuracy of the system is restricted to around ± 2 mm. Different from these systems, the DLR/Kuka robot LBR4+ is an extremely precise manipulator, driven by electric actuators, making use of compliance control methods. High costs are the main deficiency of this arm. This is due to many customized components of the drive unit plus the integration of a torque sensor on the output side of each motor shaft. Cheaper solutions, based on electric servo drives, are the UR5 and the UR10 robots that offer compliance by measuring input and output motor shaft angles in order to calculate the forces. The control strategies of these more budget-priced robots are less sophisticated than for the LBR4+. Also there are no additional torque sensors in use within the UR5 and the UR10. The principle of combining elastic springs with electric drives to gain flexibility is applied in the BioRob. Similar to the LBR4+, the UR5 and UR10, this setup is available for purchase, but the reachable payload is less. The anthropomorphic pneumatic actuator system published by Shadow Robot Company Ltd. is not available on the market, that's why no statements can be made so far. Airic's arm by Festo AG & Co. KG is another mechanism that is not commercially available. It includes very many actuators, thus the valve cluster at the torso is quite large. Concerning the precision of this setup, there are no data published. With ECCEROBOT, an electrically driven elastic robot is revealed with about 80 DC motors, which is a challenge in terms of adequate control strategies, such that vibration is kept within tolerance limits.

Modularity, i.e. expandability and scalability, is an important feature that is hardly feasible with the mechanisms presented before. So far, robots are closed systems that have a certain number of joints with a certain number of DOF. Expansion and scaling within these robots are normally realized by either adding adequate end-effectors that enlarge the workspace or by exchanging parts of the supporting structure, e.g. the forearm tube. Often robotics manufacturers simply offer different sizes of robots according to the needs of the applications, such as the UR5 and UR10 robot types by Universal Robots.

The enumeration in Table 2.11 highlights core statements that can be derived from the investigation of features and drawbacks as mentioned in the previous paragraphs.

2.4 Resulting requirements

Considering the statements of sections 2.1, 2.2 and 2.3, there are certain limitations of the state of research which shall be addressed in this thesis. Most important is the prerequisite that the actuators should guarantee inherent compliance to make sure that the system can operate in a collaboration mode with a human without safety problems. The mechanisms must be flexible even in the case of control failure. To widen the possible field of applications, the stiffness of the system is preferably controllable. Similar to the state of research constructions, lightweight design is of special significance, which supports the approach of a human-friendly mechanism. Modularity should also be part of the characteristics of the mechanisms that are to be developed. The mechanisms should offer the option to be extended by simply adding modular segments. Consequently, the control hardware and the control architecture have to fulfill these modularity requirements, and both actuators and sensors have to be arranged decentrally. Position accuracy and acceleration dynamics is a challenge for many of the introduced structures. A core

Table 2.11: Assets and drawbacks of state of research

Compliant robots based on electric servo motors with impedance control are quite elaborate and expensive
Compliant robots based on electric servo motors with simple speed or force limitation are constricted to applications where safety issues don't have priority
Due to the issues with pneumatic control accuracy, the use of pneumatic compliant mechanisms is a challenge within positioning tasks
Precision of electric motors combined with elastic transmission members results in expensive setups with huge control effort
So far there are only quite specific mechanisms available that completely fulfill compliance requirements for very particular tasks
Most of the robotic mechanisms are not modular or designed for expandability and scalability

feature of new compliant mechanisms should be precision and sufficient dynamics capabilities. Force controllability plays a fundamental role within human-robot interaction. The implementation of relevant force control strategies should be possible in a simple way. Besides technical aspects, economic issues, i.e. cost-efficiency, have to be taken into consideration. Expensive components, both actuators and sensors, in particular force or torque sensors that demand more complex control, shall be avoided, as well as elements that are not vital to the function (cf. [92]). The requirements as mentioned above can be concluded in Table 2.12.

Table 2.12: Summary of requirements

Inherently compliant mechanisms
Controllable stiffness of the system
Lightweight design
Modular mechanisms
Modular control
Decentral actuator and sensor arrangement
Positioning performance
Option to integrate force control
Cost-effective actuator technology

2.5 Opportunities for novel robot design

As a transition to the next chapter, the general concept behind the design of novel robotic mechanisms is shortly introduced, and benefits are complemented. This way, the target analysis

is addressed and the problem is already structured in an early phase of development (cf. [93]). Details about the design are revealed in Chapter 3.

To meet the demands as described in section 2.4, the design of the robots described in this thesis is structured as modular worm-like robotic mechanisms, which are composed of several segments that can be arbitrarily extended or reduced. Two different subtypes of this kind are presented to prove the concept within different constructive frameworks.

A first subtype is characterized in that each of the robot's segments can move in two DOF utilizing cardan joints that connect rigid supporting structures. In this manner, a mechanism with discrete kinematics is generated that already provides inherently compliant behavior due to the flexible PAM actuators. As a second subtype, a robot without rigid backbone is developed, based on continuum style kinematics, which allows enhanced maneuverability with three DOF per segment.

For cost-efficiency and energy-density reasons, compact demonstrators are developed, using stick-slip free PAMs powered by miniature valves. The control of the valves and indirectly the control of the actuators are realized with decentrally arranged subordinated pressure controllers plus a superordinate controller, which are all located inside each segment. This decentral arrangement allows to use extremely short air feed pipes between the valves and the pneumatic actuators, which again results in high acceleration dynamics. The dead volume of compressible air is reduced and the problems with related nonlinearities can be limited. For position control feedback, angular sensors attached to the cardan joint axes are used in case of the discrete kinematics robot. For the continuum style kinematics robot, stretch sensors are attached to each PAM. Both prototypes have integrated pressure sensors, which are fixed to all muscles to gain feedback about their actual condition. Force control is optionally feasible by utilizing the feedback of these aforementioned sensors and evaluating muscle calibration characteristics, i.e. no additional force sensors are integrated.

Table 2.13 illustrates the main advantages of the mechanisms that shall be aimed at within this thesis.

Table 2.13: Crucial benefits of the novel mechanism

Inherent compliance of the system
Cost-effective PAM actuators
Lightweight actuators
No stick-slip effect of actuators
Energy-efficiency
Active safety in terms of soft dead stop
Robustness in case of external shocks since the actuators are flexible
Force-based control easily performable without additional force sensors
Soft position changes
Modularity and extensibility

Chapter 3

Prototypes

The development of robotic prototypes deals with many individual steps that affect one another. Different mechatronic disciplines have to be considered for the process to result in functional prototypes.

In this chapter, the methodology of the novel approach and relevant development stages are identified and described in chronological order. First, the principle structure of the mechanics and electronics and an initial prototype, both of which serve as a starting point for the development of enhanced prototypes, are examined. This simple initial prototype is based on previous work and was already built for a diploma thesis in 2007 [31]. In this dissertation, final enhanced prototypes are developed that take into account knowledge that was gained with the first rudimentary setup.

Several sections introduce the novel prototypes, which are divided in two different kinematic cases – a discrete case and a continuum case. First, an overview of the entire setup is given, followed by a section dealing with the mechanical construction, in particular the frame structure, the linking cardan joint in the case of the discrete kinematics subtype, and the linking spring elements in the case of the continuum style kinematics subtype. Relevant hardware connectors that have to fix hardware components according to a concept that integrates each of the hardware modules on board within the single segments are also mentioned. The hardware layout is described in the next section, in which adoption of both the main controller boards and the pressure controller boards is presented. The integration of the actuators and sensors is discussed in another section, assessing valves and PAMs, pressure sensors, angle sensors, and stretch-strain sensors. Costs and comparison with some relevant state-of-the-art mechanisms are given in the last section.

3.1 Design and initial prototype

The fundamental design of a first prototype relates to a pneumatic mechanism that is flexible. Its shaping is serpentine or worm-like. For a first implementation, three modular mechanism units are combined to an apparatus that looks similar to a human arm. To meet the requirements of Table 2.12 from section 2.4, a mechanism construction is chosen that is based on lightweight and cost-effective PAM actuators, which allow adjustment of stiffness. PAMs are soft actuators,

inherently compliant and optionally force control is feasible with little effort. The core of the development is to improve the control quality of multi-segment mechanisms. To reach this improvement, the supply of media to each module shall be centralized, whereas the control of the actuators is decentrally arranged, such that very short and powerful control loops can be guaranteed.

3.1.1 Initial structure

A supporting structure made of aluminum is the backbone of each modular unit of the initial worm-like mechanism. The actuation means are arranged between two supporting discs, being spaced from one another. This space is optionally defined by a central rod, which is connected to a bottom disc and a joint that is fixed to the end of this central rod. A top disc is attached to a second central rod, and one end is fastened to the second side of the joint, the other end can be coupled with a following segment. The joint provides two orthogonal axes and is implemented as a cardan joint. For the actuation means PAMs, as described in subsection 2.1.3, are utilized. They are located around the central rod, organized in two antagonistic pairs. These driving elements can be controlled separately and are supplied by a central feed line. Several segments can be attached together. For each segment, stub lines supply locally arranged valve clusters to control the pneumatic actuators. Figure 3.1 depicts the general concept of the structure as described before.

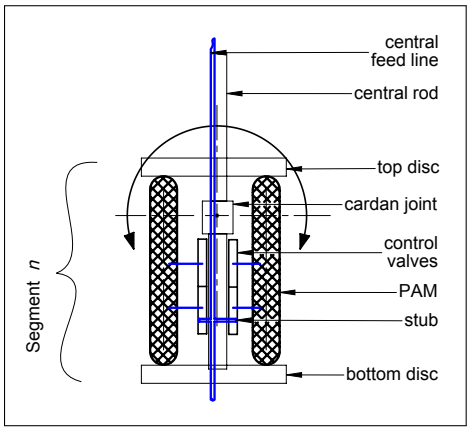

Figure 3.1: Basic structure

Three of these segments are attached serially, which creates a mechanism having movement abilities similar to a human arm. Figure 3.2 shows the combination of three segments to a worm-like mechanism as a discrete type embodiment.

3.1.2 Initial situation for final prototypes

As a starting point for further development of robotic worm-like mechanisms, a setup is utilized according to Figure 3.3 [31]. This first prototype comprises the elements as given in Table 3.1

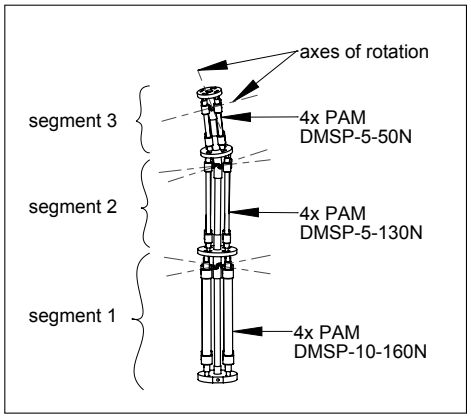

Figure 3.2: Three segments of worm-like robotic mechanism [32]

Table 3.1: Elements of initial setup

Aluminum supporting structure
Cardan joint with two DOF per segment
PAM type Festo DMSP with rope mounting and offset between axles and PAM points of attachment
2/2-way miniature solenoid valves type FAS Chipsol
Crosswise valve cluster
Simple potentiometer sensors used for position tracking
Customized valve driver boards

Figure 3.3(a) shows the initial simple assembly that is only controllable by hand, which means that neither a position nor a pressure controller is implemented. The amplifier hardware units used for switching the valves are customized hardware solutions based on transistor stages (cf. Figure 3.3(b) and 3.3(c)). For gaining position feedback, simple potentiometer sensors (cf. Figure 3.3(d)) are attached to the axles of the cardan joints that allow a quantitative display of rotational changes. Due to issues with precision, temperature drift and mechanical mounting, these potentiometers don't provide reliable information about the moving state of the system, so later on a different angle feedback system has to be implemented. The control in this first mechanical prototype is based on inflate- or exhaust-commands that are given by hand in order to open or close corresponding valves. This very first pre-configuration comprises 2/2-way miniature solenoid valves that are able to either completely open or close their orifice. In further stages of development for continuum muscle control, a PWM mode has to be realized. The valves, type FAS Chipsol with an outer diameter of 8 mm, have a quite small orifice (cf. Figure 3.3(e)), and the system dynamics is very limited as the air flux is severely restricted. Due to their overall size it is possible to integrate them in a pretty small crosswise valve cluster (cf. Figure 3.3(f)). The first prototype doesn't include pressure sensors so far and accordingly, the aforementioned manual control is open-loop. Pressure data are necessary to properly control PAM actuators.

In conclusion, the initial prototype is used as a start platform for further work within this thesis

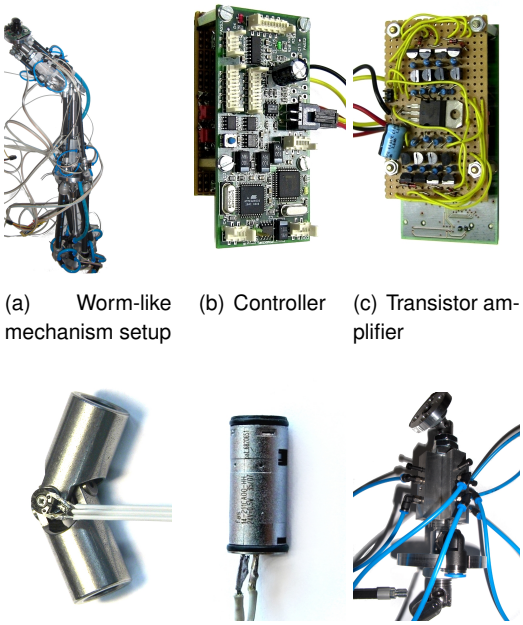

(a) Worm-like mechanism setup (b) Controller (c) Transistor amplifier

(d) Cardan joint potentiometer (e) Mini valve FAS Chipsol (f) One segment with valve cluster

Figure 3.3: Initial setup [31]

and only fulfills proof of concept in a mechanical sense. This platform is utilized to gain results for developing improved specific designs of the mechanism, in terms of mechanics, electronic hardware and control software. The first setup already shows a number of drawbacks or development needs. In Table 3.2 these disadvantages are listed, which have to be eliminated within the final prototypes. As there is no automated control implemented in this first stage of prototype, the controller design is a central issue for the development of the final prototypes. Both the construction and experimental results of these prototypes are covered in the following chapters.

3.2 Overview of final prototypes

Due to their compliant actuators, the entire mechanisms react flexibly. Different pressure can be applied to the PAM actuators, i.e. the stiffness is adjustable. The mechanisms are able to meet safety requirements that are relevant within human-robot interaction scenarios (see subsection 1.1.2). Another main goal is to create systems that are easily extendable. All subsystems are based on completely modular design, which means that the system might be either enlarged or reduced. This modularity concerns mechanical and electrical linkage, as well as control-specific issues, i.e. software (cf. Figure 3.4). Each segment has to provide the same mechanical connection. Regarding the electronics, a decentral design approach is needed, such that arbitrary numbers of subsystems can be attached to a common interconnection system. To gain software modularity, a bus network shall be used.

As mentioned before, two different prototypes with intrinsic mechanical actuation are considered

Table 3.2: Drawbacks of initial setup

Offset between axles and PAM points of attachment causes kinematic dependencies of two perpendicular cardan joint axes
Rope mounting of the PAMs often breaks or knots are loosening
Air flow through miniature valves is too small resulting in large actuation times
Very poor fine adjustment of 2/2-way valves
Simple potentiometer sensors don't guarantee precise and reliable angle data
Bulky customized valve driver boards with EMC problems
Driver boards are not mounted within the segments
Precise PAM control is not feasible without pressure sensors

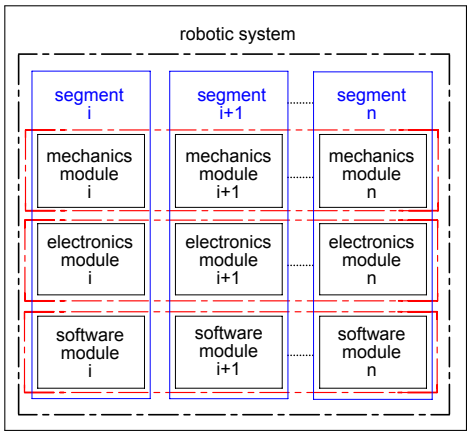

Figure 3.4: Modular setup

in this thesis. The first subtype has a modular and rigid backbone structure, which is rotatable about cardan joints, thus each segment has two DOF and is linked as a discrete mechanical structure. Position monitoring is handled by rotary encoders that are attached to the joints of the cardan axes. Depending on how many modules are included, this discrete redundant robot can be extended to a discrete hyperredundant robot with many units. The second subtype is based on a flexible backbone structure, such that a continuum style soft robotic mechanism results [152]. In this case a position control utilizes stretch sensors that detect the length of the arc elements of each segment. Two rotational DOF are feasible plus a third translational DOF for extension/contraction. Figure 3.5 shows the general outer shape of both discrete and continuum prototypes. For a better comparison both types are presented comprising three segments.

In the subsequent sections, the discrete and the continuum style prototypical constructions of these worm-like robotic mechanisms are discussed successively. Details about the mechanics of the developed mechanisms are revealed. In particular, the design of the modular robotic frame structures, their interlinking elements, and customized hardware connectors, used for

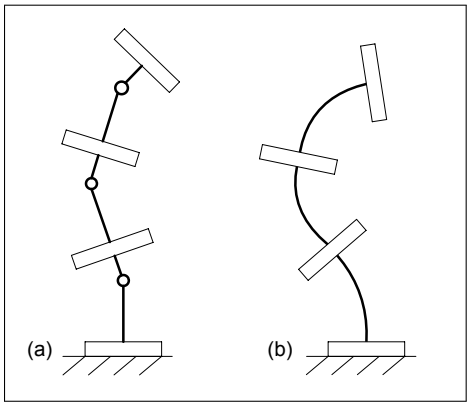

Figure 3.5: Prototypes: a) discrete b) continuum style

mounting all on-board hardware components directly at each segment, are highlighted. Both of the two kinematically different subsystems are structured, such that an arrangement of independently controllable segments results, all with locally fixed actuators and actuator control units.

3.3 Discrete mechanical design

The discrete kinematics prototype in this section is a serial arrangement of rigid framework units, driven by four compliant PAMs per segment. Discrete in this context means that all DOF of the robot are rotations about fixed positions, which are defined by the cardan joint axes that connect the movable parts of each segment. The reason for implementing such a serial kinematics with a rigid backbone is the simplicity of the construction, while having good movement options and controllability. As the PAM actuators behave flexibly, the entire mechanism becomes compliant. The frame structure, the cardan joint as well as the hardware connectors of the discrete style robot are presented in the next three subsections 3.3.1 - 3.3.3.

3.3.1 Discrete frame structure

All single segments of the discrete mechanism frame structure are based on the same design, comprising the following elements, shown in Figure 3.6.

Core supporting component of the mechanism is an aluminum bottom disc, which carries a first aluminum rod. The aluminum disc has a central threaded bore. This bore is used to screw in the rod, which is threaded at its ends as well. A lock nut and a serrated lock washer serve as a twist lock. The mechanism does not include any torsion joints, but only tilt links. Torsional moment only occurs either during accelerations or due to loads and gravitational influence. Accordingly, the aforementioned anti-rotation protection is sufficient. At the second end of the rod there is another thread, which is the interface to a cardan joint offering two rotational DOF. On the other side of the cardan joint a moving disc is attached. Again, this disc has a central threaded bore, which is fixed with a second rod similar to the first one. The second rod is located between the cardan joint and the disc, and the end of this rod is not in alignment with the moving disc, but longer. The second end of the rod can be used as a first rod for the following segment.

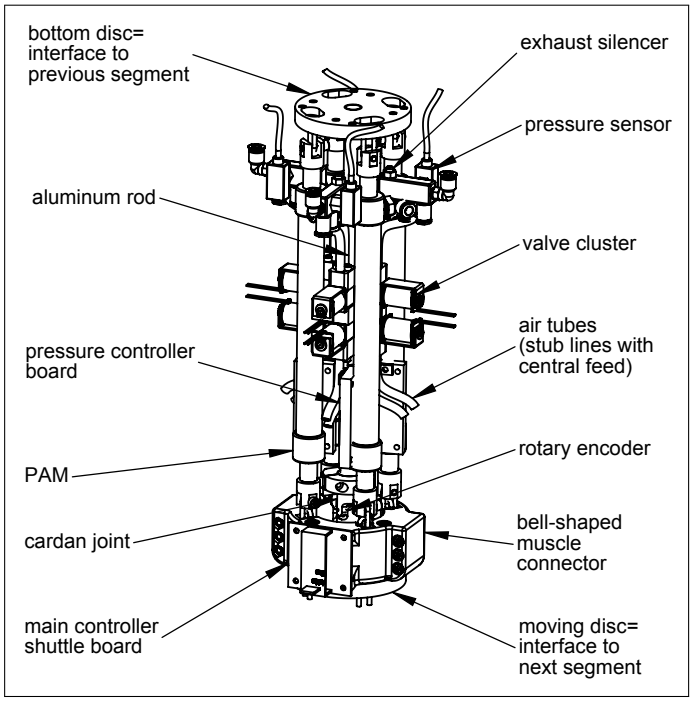

Figure 3.6: One segment of discrete worm-like robotic mechanism

Between each pair of discs two antagonistic pairs of PAMs are symmetrically distributed around the central rod. Motions in two DOF, in both directions of each cardan joint axis (back and forth move), are feasible, which are detailed in subsection 3.6.2.

The key specification of the entire system, comprising three segments for the current discrete prototype, is shown in Table 3.3. It gives information about geometric dimensions, types of components, joint angles, material and suppliers.

3.3.2 Cardan joint

According to subsection 3.3.1, a cardan joint is used between each of the mechanism's segments to allow movements in two DOF (cf. Figure 3.7). Both axes of the cardan joint are orthogonally aligned to each other and orthogonal to the longitudinal axis of the rod. Consequently, the mechanism can be tilted in two directions about these cardan joint axes. The reason for using a universal joint instead of a ball joint is that torsional movement should be restricted and it should be possible to record joint angles easily. Spherical joints usually feature three DOF, but state-of-the-art setups show that there are ways to limit this number, i.e. such a joint can be manufactured with a ring groove in order to prevent torsional movements. However, the problem of direct and simple angle measurement would not be solved. In contrast, cardan joints can be equipped with simple rotary encoders to measure their angular positions (cf. subsection 3.6.4). The assembly of a mechanism including universal joints is possible without large expenditure.

Table 3.3: Key specification of the discrete worm-like robotic mechanism

Overall length L	1050 mm
Max. diameter D	140 mm
Number of segments	3
Length of segment 1 L_1	280 mm
Length of segment 2 L_2	350 mm
Length of segment 3 L_3	350 mm
Length of flange L_4	70 mm
Overall weight m	about 4800 g
Payload	about 1200 g
Number of PAMs	12
PAM type	Festo DMSP-10-160-RM-CM
Number of valves	24
Valve type	proportional valve, Parker MD-PRO
Number of pressure sensors	12
Pressure sensor type	analog, SMC PSE-510-M5-Q
Number of angular sensors	6
Angular sensor type	magnetic, absolute, ams AS5145H-HSST SSOP16 LF
Angular sensor resolution	12 bit
Max. joint angles (segment)	about $\pm 16^\circ$
Max. global deflection of arm	about $\pm 27^\circ$
Max. lifting of entire arm	about 75 mm
Max. joint velocity ω_{max}	16 °/s
Max. joint torque	6.3 N m
Frame material	Aluminum
Hardware connector material	ABS
Voltage supply	5/9/12V
Air supply	6.9 bar

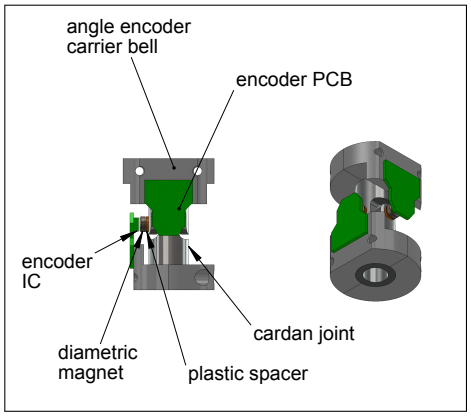

Figure 3.7: Cardan joint

3.3.3 Discrete hardware connectors

Frame and cardan joint supporting structures as introduced in subsections 3.3.1 and 3.3.2 carry several connectors to mount hardware. To realize a lightweight construction, mainly rapid prototyping plastic parts[1] are utilized. These generatively manufactured elements have the advantage that nearly all conceivable shapes and hollow honeycomb structures can be built. The parts are extremely lightweight with relatively high stiffness. Only a few connectors are fabricated with conventional turning and milling technology – if either smallest shape and position tolerances or impermeability to air are significant. These parts are made of plastics (PVC) and aluminum. The latter is used for parts with threaded bores and the ones that need higher load-bearing capacity.

Among the most challenging tasks of mechanical integration is the design of a valve cluster for each segment, which is as compact as possible. Also the weight and the inertia of such a cluster must be kept low. Else the payload of each segment would decrease and the dimensions of the entire setup would increase, in particular the mechanism's diameter. One robot segment utilizes four PAMs, which means that eight valves (four inlet valves, four outlet valves) are to be mounted in the cluster (cf. Figure 3.8(a)). Specifics about the integration of this cluster are detailed later on in subsection 3.6.1.

Further attention has to be given to the mounting of the rotary encoders to realize reliable position feedback from the rotation of all joint axes. For this purpose, divisible plastic rings are designed as turning and milling parts. Figure 3.8(b) illustrates the rotary encoder connector. Detailed information about the mechanical integration within the entire mechanism is provided in subsection 3.6.4.

Another quite important plastic connector made by rapid prototyping machinery is a bell-shaped muscle connector. This connector is necessary because of the kinematic coupling between the PAM pairs, which occurs during the rotation of two neighboring muscle pairs. Once an antagonistic pair of PAMs rotates one axis of a cardan joint, the second pair of muscles automatically changes its length if the muscles are directly connected to the top plate of each segment. The mutual influence would make a position control more difficult. In order to avoid this dependency and to nearly eliminate transmission of vibrations, this decoupling element is introduced. For

[1] FDM printing technology, ABS material

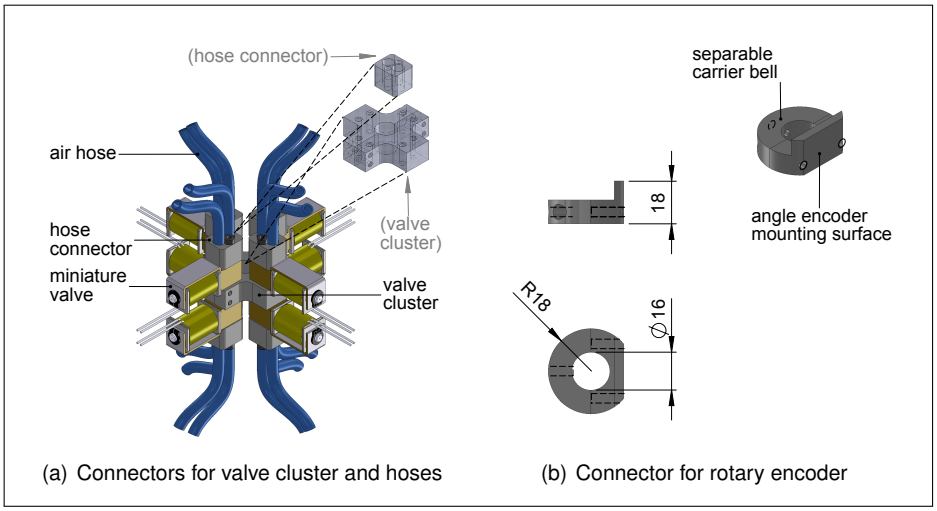

(a) Connectors for valve cluster and hoses (b) Connector for rotary encoder

Figure 3.8: Connectors for valves and encoders

ease of mounting, the bell-shaped connector is divisible into two half-rings. These rings guarantee that all of the upper PAM suspension points are in a line that intersects with the joint axis, which is shown in Figure 3.9(a). The model of the bell-shaped muscle connector is depicted in Figure 3.9(b).

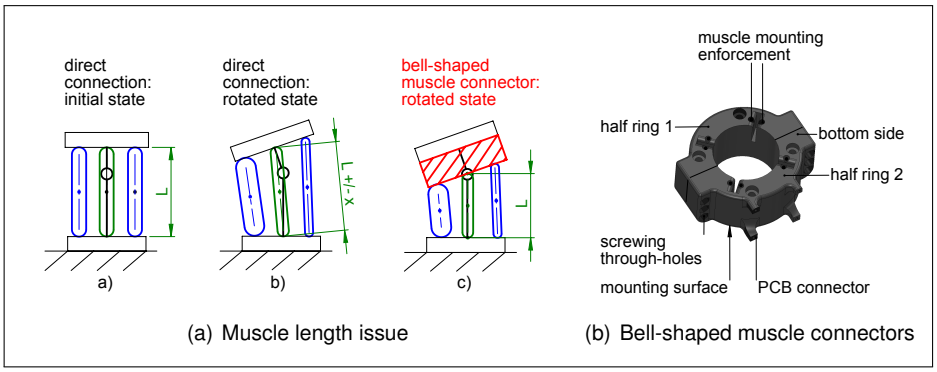

(a) Muscle length issue (b) Bell-shaped muscle connectors

Figure 3.9: Fixation of muscles

Two more connector elements are presented in Figure 3.10. The pressure controller connector is designed as a simple plastic assembly that comprises four single connector pieces with an angular shape and a rounding at each edge. Accordingly, four of these connectors cluster around the central rod for fixation. The pressure sensor connector is a milled block with a number of threaded bores to screw fittings as well as the pressure sensor with its M5 threaded plug. This block also includes a silencer for the attached exhaust valve.

3.4 Continuum mechanical design

After the introduction of a discrete prototype in the previous section 3.3, another enhanced prototype shall be presented in the upcoming section. The enhanced prototype is characterized

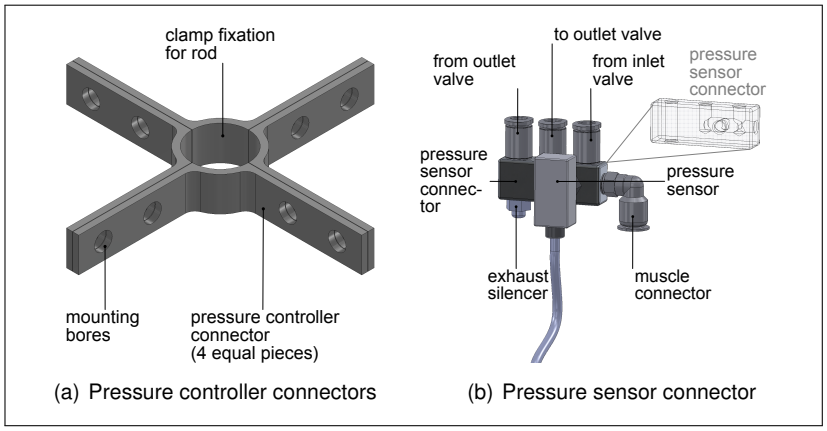

(a) Pressure controller connectors (b) Pressure sensor connector

Figure 3.10: Connectors for pressure devices

by a robotic arm with continuum style kinematics. This continuum style kinematics replaces a kinematics that utilized a rigid frame structure with stiff aluminum components. Instead, the entire system is bendable and most of the mechanical components are flexible. The overall system merges mechanical links and actuators in a soft structure.

3.4.1 Continuum frame structure

The continuum style kinematics can be seen as an enhanced development of the discrete worm-like mechanism, as presented in the previous section 3.3. There are several crucial differences. The main difference is that each of the modular segments has three DOF. More precisely, theoretically each segment is a mechanism with infinite DOF due to the flexible structure, but the actuator control allows to influence only three DOF independently. Consequently, the system is underactuated [86, 116, 148]. The additional translational DOF makes extension/contraction movements possible. Due to this additional DOF it is no longer feasible to integrate a rigid backbone as it is done in the previous discrete subtype. The PAMs are directly connected to their bottom and top suspension plates made of aluminum, supported by additional compression springs, which are used to brace the segments. In this way, the loads aren't carried by a rigid frame structure, but by the muscles and the springs. In particular, compressive forces are absorbed by the spring elements, since the PAM actuators can only withstand tensile forces. For this reason, pressure springs are used to cope with compressive forces. Also the springs support transverse loads to a certain extent, which means that the PAMs are relieved from loads that reduce their lifetime. The setup does not integrate any mechanical joints as in the discrete robot case, instead the continuum robot mechanism bends around its PAMs. The muscles curve if the three PAMs of one segment are set under different pressures.

The discrete prototype integrated four symmetrically arranged PAMs, i.e. two antagonistic pairs. Here the setup comprises three PAMs that are parallel to each other and form a triangle. In this manner, the number of PAMs is decreased. Within the continuum prototypical subtype, the PAM membrane curves during bending of a segment, which means that muscle force or bending energy is necessary to deform the PAMs. Accordingly, the fewer muscles there are, the less deforming energy is necessary, which would diminish the positioning force. Similar to the discrete setup's frame design (cf. subsection 3.3.1), each segment has two aluminum plates

with central bores. One bottom plate serves as the base of the segment, one top plate serves as the local ending of the segment. Both plates have connection means, such that a previous/ subsequent segment can be attached easily. In contrast to the discs used for the discrete setup, the plates here offer direct installation options for mounting hardware, such as the main controller shuttle board, pressure controller boards, stretch sensor and the gyroscope/acceleration sensor. Each segment is equipped with three PAMs and three pressure controller boards with one superordinate main controller board. These four controller devices can be distributed at the sides of the quadrangular bottom plate of each segment. In the centre of each top plate the gyroscope/acceleration sensor is fixed. In order to guarantee easy assembly and disassembly of several segments to a continuum style worm-like mechanism, each top plate is connected to the bottom plate of the next segment using three knurled screws, which can be fixed by hand. Figure 3.11 depicts the general structure of one continuum segment.

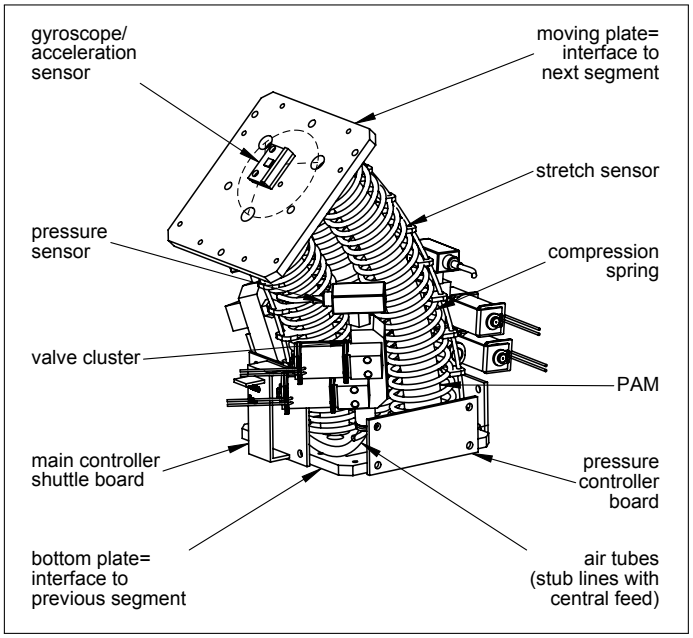

Figure 3.11: Continuum style segment

Analogous to the discrete case, the key specification for the continuum setup can be summarized in Table 3.4, including all relevant data. This table presents a continuum prototype comprising four segments in total, as it is developed exemplarily within this thesis.

3.4.2 Continuum hardware connectors

The continuum worm-like robotic mechanism is highly flexible, and all hardware units have to be attached to the segments such that this flexibility is minimally affected. Hardware components have to be positioned carefully and for some components the arrangement should be even bendable. Basically three different types of hardware need to be fixed to each of the modular segments – (1) control hardware, such as main controller shuttle board and pressure controller boards, (2) sensors, i.e. pressure sensors, stretch sensors and gyroscope/acceleration sensor, (3) valves, which means the inlet and outlet valves connected within a cluster. For reasons of

Table 3.4: Key specification of the continuum worm-like robotic mechanism

Overall length L	1008 mm
Max. diameter D	125 mm
Number of segments	4
Length of segment 1 L_1	252 mm
Length of segment 2 L_2	252 mm
Length of segment 3 L_3	252 mm
Length of segment 4 L_4	252 mm
Overall weight m	about 4000 g
Payload	about 1200 g
Number of PAMs	12
PAM type	Festo DMSP-10-160-RM-CM
Number of compression springs	12
Compression spring type	30 mm $\times$ 2.7 mm, 10 mm pitch, 21 coils, steel
Number of valves	24
Valve type	proportional valve, Parker MD-PRO
Number of pressure sensors	12
Pressure sensor type	analog, SMC PSE-510-M5-Q
Number of stretch sensors	12
Stretch sensor type	polymer resistor, Images Scientific Instruments Inc.
Repeatability stretch sensor	2 %
Max. segment angles	about $\pm 30^\circ$
Max. lifting of arm	about 120 mm
Max. linear velocity v_{max}	85 mm/s
Max. rotary velocity ω_{max}	20 °/s
Frame material	Aluminum
Hardware connector material	ABS
Voltage supply	3/5/9/12 V
Air supply	6.9 bar

weight, most of these connectors are made of ABS material, manufactured in rapid prototyping technique.

Both the main controller shuttle board with its Teensy 3.1 microcontroller on it and the three customized pressure controller boards are simply attached to one segment bottom plate utilizing mounting brackets, electrically isolated by means of rubber buffers. It is beneficial to fix the pressure controller boards horizontally in order to reduce installation height.[2]

It is a very important factor to mount the valves (cf. subsection 3.6.1) and the pressure sensors (cf. subsection 3.6.3) as close as possible to each PAM. This saves installation space and ensures movement abilities. A curvature of the segment must be guaranteed, which requires a flexible fixture solution. There is not enough space between the PAMs and spring elements, such that the valves could be mounted in a similar way as previously described for the discrete case in subsection 3.3.3. All PAMs are spaced only 44 mm from each other and the gap between two springs is 14 mm. It is reasonable to put the valves outside the area of the PAMs and their springs. Furthermore, it is favorable to keep the distance between the valve, the PAM and the pressure sensor as short as possible. That's why an integrated valve cluster with pressure sensor mounting is designed. Both the inlet and outlet valves for one muscle are slightly displaced in relation to each other, which allows to use a common air channel for PAM feeding and exhausting. The inlet channel of the inlet valve is connected to an air supply connector, and the exhaust channel of the outlet valve is combined with an exhaust silencer. In this manner, the valve cluster including the pressure sensor and hose connections are paired together on smallest space, located beside the PAMs and springs. Figure 3.12 shows the facts described before. One segment is equipped with three of these clusters, decentrally supporting each of the three PAMs. These three clusters are connected with a central air feed line, using adequate stub line hoses.

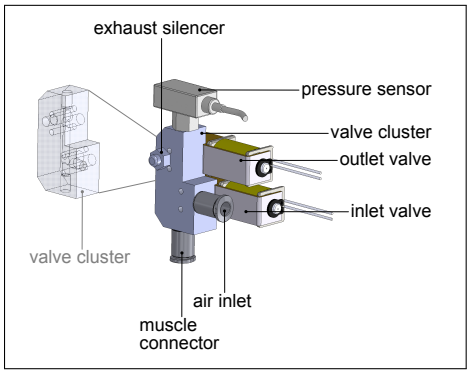

Figure 3.12: Valve cluster with pressure sensor

After arranging the valves and the pressure sensors it is not less crucial to attach the position sensors in a best possible way. The idea of position sensing is based on detecting the length of each PAM, which degenerates into an arc length once a PAM bends. Hence, the position sensors have to be both bendable and extendible, also the sensors should be tightly placed along the lateral surface of the PAMs. In the continuum robot case the PAMs are surrounded by compression springs (cf. subsection 3.6.2 or Figure 3.13). The spring coils were chosen to support these sensors. Stretch sensors, which will be described later on in subsection 3.6.5, are

[2] the external dimension of one pressure controller board is 65 mm $\times$ 28 mm

practical means for flexible curvature and arc length measurement. These sensors are polymer cords that have to be used with a guiding system to keep them at the PAM lateral surface as tight as possible. For this reason, two-piece stretch sensor connectors are designed made of non-conductive ABS. The connector comprises a C-shaped guide that has a twist drilling such that it can be slipped over the spring coils. To guide the cord, a locking piece is connected to the C-shaped guide and between both parts the sensor can be attached, being able to slide along the lateral surface. As the springs could rotate about their axes and thus influence the position sensing, spring connector elements are integrated as anti-rotation devices. For a better understanding of the position sensor mounting, Figure 3.13 depicts the information given above. To simplify the presentation, only one stretch sensor with one spring is shown without a PAM.

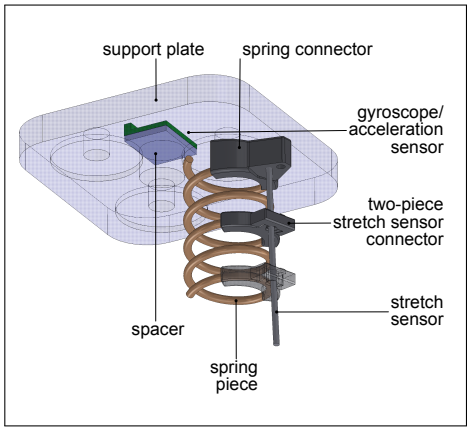

Figure 3.13: Connector for stretch sensor

In addition to the pressure and position sensors, there is a combined gyroscope and acceleration sensor that has to be mounted on each moving plate of one segment. Details about this sensor are presented in subsection 3.6.6. Fixing this kind of sensor is straightforward as it comes in a breakout board version that can be easily screwed on the plate. To simplify the evaluation process of the acceleration and rotational speed data, the sensor is located on top of the moving plate, in the line of the longitudinal axis of the segment. The connector of this sensor consists of a non-conductive spacer device with two bores, which allow a screw connection to the aluminum plates (cf. Figure 3.13).

3.5 Hardware layout

The allocation of the control electronics for the worm-like robotic mechanisms follows the principle of decentralization. Control units are distributed over the entire system to build independent and modular subsystems. Details about all different electronic boards are shown in the next subsections.

3.5.1 Main controller boards

Each of the mechanism's segments is equipped with a main controller board. Since the computation requirements for the discrete and continuum style robot prototypes are pretty different, also different kinds of main controller boards are realized. To meet modularity demands, these controller boards are mounted on adapter boards, each with the same dimension.

The discrete robot setup does not require computationally intensive tasks on segment level. One main controller only has to care about simple sensor data processing and switching the valves. For reasons of costs and installation space, an Arduino Nano 3.0 board is chosen with an ATmega 328 microcontroller with 8 bit CPU on board running at 16 MHz, having 32 kB flash memory (cf. Figure 3.14(a)). This board has quite small external dimensions of 18.5 mm $\times$ 43.2 mm and comes with a Mini-USB connection, which serves as the programming interface for a standard PC. The board is docked on an adapter board that features bus connectors, power connector and angle sensor input connectors. Correspondingly, these main controller boards are integrated in a bus system, more precisely an i^2C bus.

For the continuum robot setup, the situation is different regarding sensor data processing. Instead of rotary encoders with convenient digital SSI data feedback, stretch sensors (cf. subsection 3.6.5) and in a stage of expansion in the future also gyroscopes and acceleration sensors (cf. subsection 3.6.6) are in the loop. Gyroscope and acceleration data together with the stretch sensor information are much more computationally intensive. The problem with the stretch sensor feedback is that their analog resistance value output has a very large hysteresis and must be post-processed. This post-processing is expensive. Also the data synchronization and data fusion of gyroscope/acceleration sensor and stretch sensor is complex, which shall be implemented within a future expansion stage. For this reason, Teensy 3.1 boards based on an Arm Cortex-M4 32 bit chip are used, which provide 72 MHz clock speed, 256 kB flash memory, and i^2C modulator (cf. Figure 3.14(b)). These boards are efficient, reasonably priced and pretty small, having external dimensions of 17.8 mm $\times$ 30.5 mm. Similar to the previous description of the discrete prototype, the continuum style main controller board is shuttled by means of an adapter board, which offers connectors to the gyroscope/acceleration sensor, to the subordinate pressure controller boards, and to the i^2C network. The i^2C bus allows communication with all the pressure controller units of one segment. Again several segments' main boards are connected via i^2C bus, giving superordinate commands to subordinated pressure units, which are described in the following subsection (cf. subsection 3.5.2). More on the communication and hardware architecture including i^2C bus can be read in section 5.6.

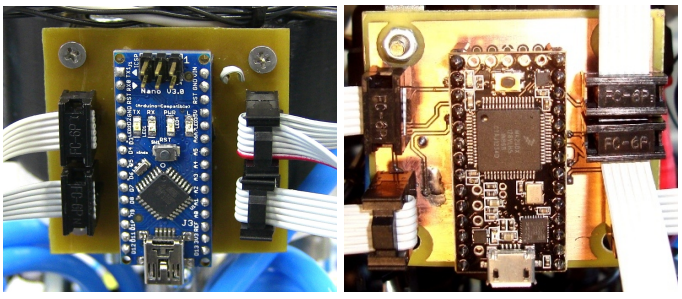

(a) Arduino Nano board (b) Teensy board

Figure 3.14: Main controller adapter boards

3.5.2 Pressure controller boards

The idea of having individual pressure controller boards for each actuator is driven by a consistent decentralization concept. All the actuators have an associated pressure controller board, which deals with the low-level control of the drives. The advantage of this spatial distribution is that all units are equally spaced, such that they can be allocated very close to their drives without standing out from the mechanism's contours. Due to the decentralized approach, the main controller boards, as described in subsection 3.5.1, can be designed as very compact and inexpensive units. In this respect, the decentral arrangement is accompanied by a distribution of processing power and cost savings for hardware.

All pressure controller boards basically comprise a small Atmel ATTiny24 microcontroller with integrated ADC (analog-to-digital converter) and two current controller stages for the inlet and outlet valves. A picture of the pressure controller board is presented in Figure 3.15, the circuit diagram for one of the current controller stages is shown in Figure 3.16.

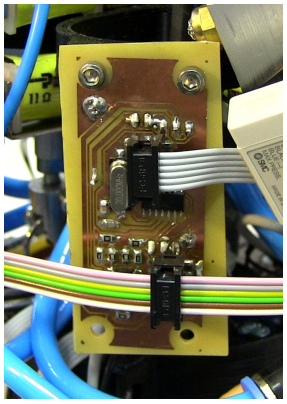

Figure 3.15: Pressure controller board

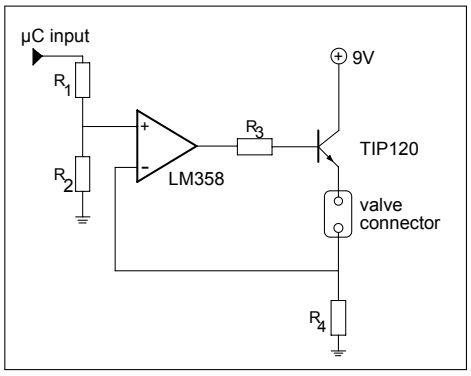

Figure 3.16: Current controller (cf. [118])

The 8 bit ATTiny24 RISC chip comes with a frequency of 20 MHz, 12 programmable I/O lines, a flash program memory size of 2 kB and a 10 bit ADC, which is utilized for the integration of the pressure data. In the continuum case, also stretch sensor data are fed to the pressure controller board. Hence, each board has connectors for two valves, one pressure sensor, one stretch sensor and i^2C bus. Both current controller stages comprise an operational amplifier together

with a transistor and a shunt resistor. The 1 Ω shunt resistor is used such that the operational amplifier can control the valve current considering the voltage drop at the shunt resistor R_3. For the Parker MDPRO valves, which are utilized, a maximum input current for full flow is specified at 304 mA. A voltage divider stage has a resistor R_1 with 5100 Ω and a resistor R_2 with 330 Ω and is connected to the operational amplifier to adequately balance microcontroller voltage and maximum valve current. The transistor TIP120 bridges the +9 V voltage supply that runs the valve, which can be linked to the valve connector on board of the current controller. In this way, the current of the valve is controlled relatively to the input voltage at the operational amplifier, which is influenced by the input received from the ATTiny microcontroller. Details about the overall pressure control loop, performed with the previously described pressure controller board, are given in section 5.3.

3.6 Actuator and sensor integration

To ensure compact package, it is crucial that both actuators and sensors are strategically located. Slimline design is necessary to enable motions even within cramped conditions and to save energy. Compact mechanisms with reduced mass and mass moment of inertia consume less power. The next subsections explore the theme of such an integration of various components.

3.6.1 Miniature valves

The technical integration of all valves for switching the pneumatic actuators is one of the most important steps towards compact configuration. In this manner, the choice of adequate small valves has certain consequences. As mentioned in subsection 3.1.2 or Table 3.2, extremely compact and simple binary on-off miniature valves[3] as used in the initial prototype turned out to be too slow. New proportional valves with larger size that behave faster and more precisely are chosen instead. They need acceptable installation space in relation to their performance (cf. Figure 3.17, [32]). By means of these new proportional valves much better overall control precision can be reached. The main problem to find compact valves is that most of the miniature valves are not available as proportional valves, and also that proportional valves usually have large sizes with high weight. Only a very limited number of miniature valves can be purchased, that are both economic and meet the demands of size and weight (cf. Table 3.5). It turned out that MDPRO and VSO valves from Parker Hannifin Corporation, Cleveland, USA, are reasonable proportional pressure control devices. The limit of the MDPRO types is that the maximum pressure is 6.9 bar, and the VSO valves can bear up to 10 bar. However, the VSO valves have disadvantages regarding flow rate. Balancing the pros and cons, MDPRO types were chosen to allow fast control. Compared to large-sized valves, the miniature valves offer less flow rates, which are a matter of size. The inner volume of the PAM actuators is only 12.6 cm^3, so it takes less than 0.04 s to fill it with the MDPRO valves, and less than 0.1 s to completely fill it with VSO valves. Both times for filling are acceptable, that's why the limited flow is not an issue within the applications presented here.

[3] by FAS, type Chipsol, with a diameter of 8.4 mm and an overall length of 24 mm

Table 3.5: Comparison of proportional valves

Manufacturer	Festo	Norgren	Parker	Parker	Hoerbiger	Landefeld
Type	VPWP	VP12	VSONC-3S11VAF8	MDPRO-4VAF8S	tecno-easy PRE-U3	DRPD
Design	5/3-way sleeve valve	n/a	2-way normally closed	2-way normally closed	3-way piezoelectric pilot valve	3/2-way seated valve
Flow	350 L/min	220 L/min	7 L/min	18 L/min	220 L/min	300 L/min
Pressure	10 bar	8 bar	10 bar	6.9 bar	8 bar	10 bar
Length	80 mm	36 mm	45 mm	45 mm	37 mm	63 mm
Width	60 mm	34 mm	16 mm	16 mm	36 mm	35 mm
Height	105 mm	64 mm	17.3 mm	17.3 mm	68.5 mm	80 mm
Weight	776 g	200 g	63 g	63 g	100 g	700 g
Costs	500 Euro	514 Euro	93 Euro	60 Euro	450 Euro	725 Euro

Analogous to what was shown in the subsections 3.3.3 and 3.4.2 or Figures 3.8 and 3.12, it has to be mentioned, that different valve cluster approaches are necessary for the discrete and the continuum robot prototypes.

For the discrete robot, one segment includes four PAMs that have to be controlled by eight valves. One muscle needs to be equipped with two valves, one for inflation and another one for deflation. The valves have to be arranged such that a minimum of space is required and that the motions of the segment with its muscles are not restricted. To meet these demands, a valve cluster connector is developed that allows the integration of eight valves. The shape of this connector is basically crosswise and has mounting holes for screwing valves opposite to one another on the top and bottom side. To simplify the installation, the connector is split in two, such that it can be attached to the aluminum rod of the supporting structure with a clamp connection. Figure 3.17 depicts the miniature valve used with its dimensions, and Figure 3.18(a) shows a real picture of the discrete valve arrangement.

Conversely, the continuum style robot demands a more flexible valve integration. As explained in subsection 3.4.2, each segment has to be equipped with three valve clusters to supply three PAMs, carrying two valves each, again one for inlet and one for outlet. Due to installation space limitations, the clusters cannot be reasonably fixed between the PAM actuators. Instead, they are attached beside the actuators. The valve clusters are connected to the PAMs using flexible polyurethane hoses, and they can also curve with the bending segment. For compactness reasons, the pressure sensors are already integrated in the cluster, which means that the pressure can be measured very directly without long hose distances between the sensor and the PAM actuator. Figure 3.18(b) presents a picture of the real integration of the continuum cluster.

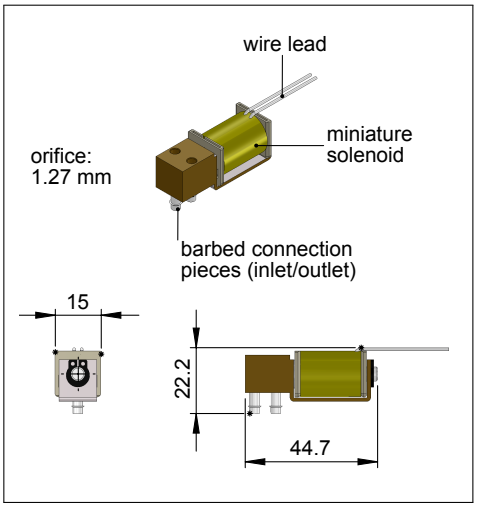

Figure 3.17: Miniature valve Parker MDPRO

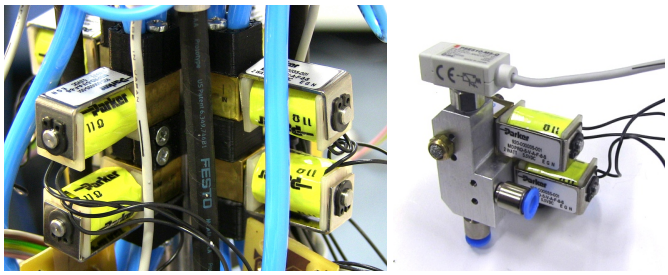

(a) Discrete case (b) Continuum case

Figure 3.18: Valve clusters

3.6.2 Pneumatic artificial muscles

The PAMs utilized for the robotic prototypes are specified as follows. Festo AG & Co. KG is the only supplier of PAMs with industrial quality, that's why PAMs of this supplier are installed. There are different PAM types available, but the DMSP types are currently the ones with lowest weight and greatest compactness (30 % less weight than MAS types and about 25 % more compact cross section). Additionally, the DMSP version is more durable than the MAS alternative (PAMs installed in 2007 are still in use). This is mainly due to their specialized arrangement of strand groups in a crossover configuration, based on aramid that is embedded in a chloroprene sleeve. This arrangement of strand groups causes much less wearing than within conventional PAMs, in which the fibers rub against one another. Table 3.6 shows the technical specification of the PAMs utilized, Figure 3.19 depicts the PAM structure. The weight of the muscles used is 74 g for a DMSP-10-160N-RM-CM PAM-type, having a maximum drag force of 630 N at 8 bar [40, 41, 62]. These values are valid for a PAM with a diameter of 10 mm, but other PAM sizes would be available, resulting in different force-contraction values. For more on this, see Figure 4.13 of section 4.5 within Chapter 4.

The efficiency of PAM actuators compared to other state-of-the-art pneumatic actuators was already discussed in Chapter 2, in particular explained within Table 2.7. Additionally, Table 2.8

Table 3.6: Specification of PAM actuator

Type	Festo DMSP-160N-RM-CM
Max. force	630 N
Max. pressure	8 bar
Max. operating frequency	3-150 Hz
Max. velocity	1.5 m/s
Normal leakage	1 l/h
Repeat accuracy	3 %
Theoretic air consumption (1 Hz, 6 bar)	10 l/min
Weight	74 g
Max. payload	30 kg
Nominal length	160 mm
Inner diameter	10 mm
Max. outer diameter	18 mm
Overall length	242 mm
Max. contraction	25 % (40 mm)
Max. elongation	3 % (4.8 mm)
Sleeve material	chloroprene
Fiber material	aramid

gave an overview about how current state-of-the-art pneumatics components can be differentiated with respect to operating pressure.

The mechanical arrangement of the actuators implies four PAMs per segment in the discrete case, and three PAMs within the continuum prototype. Each muscle is connected to two proportional valves (cf. subsection 3.6.1). Both design variants, discrete and continuum prototype, are explained below.

The discrete setup comprises four PAMs, which operate opposite to one another to have perpendicular impact. PAMs are actuators that only generate traction forces, and pairwise arrangement is necessary to create back and forth movements. Alternatively, springs could be used to ensure backward movement, but in this case the PAMs have to work against the spring force, which means that some energy is lost. Due to this reason, more than two PAMs are integrated within one segment. For the control of both DOF of the cardan joint, at least three PAMs are necessary if springs are not utilized. To have a more symmetric force distribution and higher output forces, four PAMs are installed in the discrete setup. Even more PAMs would result in better symmetry, but the arrangement of four PAMs is a good compromise in terms of construction volume, force and symmetry.

As the shortening abilities of the PAMs used here are much higher than the elongation options,

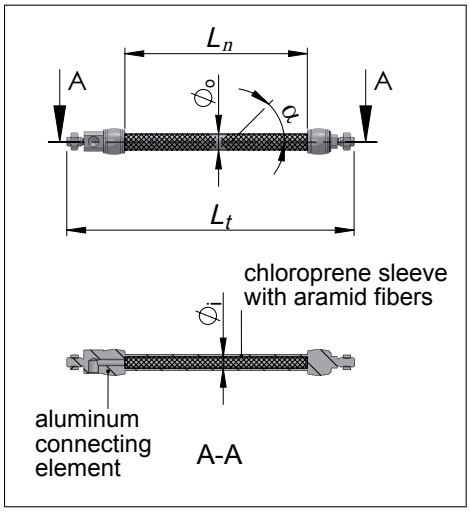

Figure 3.19: PAM structure

there is an asymmetric behavior that has to be considered when mounting the muscles to the segment. Maximum shortening is feasible up to 25 %, but expanding is limited to about 3 %. One antagonistic pair of muscles is responsible for a rotation about the cardan joint axis in both directions, i.e. while one PAM contracts, the other one has to expand. The PAMs mustn't be fixed tightly to the segment structure, but have to be loosely inserted between the two supporting discs. Before one segment starts to move, first both antagonistic muscles have to be tensed to get contact to the supporting elements. This pre-stressing is coupled with a muscle mounting that allows freedom of movement if the PAMs are relaxed and rigid contact while inflated. The initial prototype setup from section 3.1 used Dyneema cords to connect the PAMs to the supporting discs, but loosening of the knots is an issue. For this reason, the current system uses steel chain elements to connect the ends of each PAM to U-like mounting brackets that are fixed to the supporting discs. The backlash, i.e. the way of travel until a PAM is rigidly connected to these supporting brackets, can be adjusted, as the mounting brackets have threaded ends that can be fastened with nuts. Figure 3.20 shows the connecting elements of the PAM as described above. The aforementioned backlash is adjusted until the pre-stressing corresponds to half of the maximum contraction of the PAM, i.e. 12.5 %. Both antagonistic muscles can expand and shorten equally starting from the reference position with 12.5 % contraction. 3 % expansion capability is reserved for safety reasons.

In contrast to the discrete setup, the pneumatic muscle arrangement in the continuum robot prototype uses three PAMs per segment (cf. subsection 3.4.1). The muscles are rigidly mounted on the supporting plates, thus transmitting bending and torsion moments. In order to support the muscles, additional springs are integrated. The setup of three parallel PAMs including their springs and the formation in a triangular pattern help to cope with the loads and to convert the torques into forces that can be handled. Due to their flexible chloroprene sleeve, the muscles can curve up to a maximum value, after which buckling occurs, which has to be prevented. The direct rigid mounting doesn't need any interfacing means between the PAMs and the support plates, hence the assembly is very easy. In a reference position, i.e. if all PAMs of one segment are vented, the overall length of the segment reaches its maximum, and in any kind of inflated state the unit shortens and/or bends (cf. Figure 3.11 or 3.32).

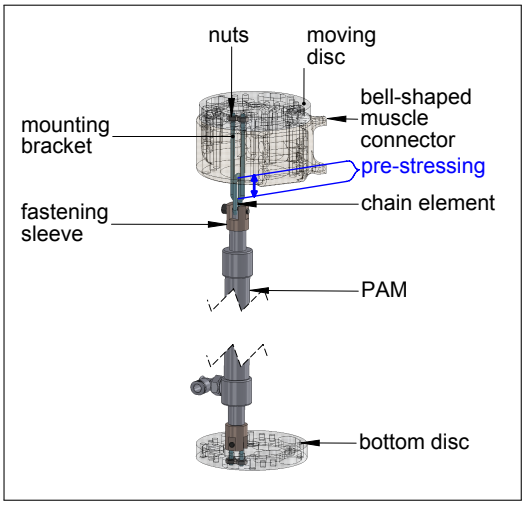

Figure 3.20: Fastening of PAMs

3.6.3 Pressure sensors

Pressure control is the key for any accurate control of pneumatic actuators. The PAMs in the setup described here are equipped with a gauge each. Pursuing the approach of decentralized actuator and sensor components, the pressure sensors are integrated locally within the segments, mounted very close to the PAMs. In this way, the dead volume between the actuators and the sensors is minimal, so the gauge can detect the internal pressure of the PAM instantaneously. Specific influence of airflow within tubes or fittings doesn't play an important role then. The selected pressure sensors are embedded in a plastic housing and are among the smallest devices obtainable on the industrial market. In Figure 3.21 the dimensions of this gauge are shown, the real device is depicted in Figure 3.22. Relevant specification data of the sensor are highlighted in Table 3.7. Regarding mechanical integration of the gauge, corresponding images can be seen in subsection 3.3.3, Figure 3.10 and in subsection 3.4.2 with Figure 3.12. The actual implementation of the pressure control, based on the sensors introduced here, is referred to in Chapter 5, section 5.3.

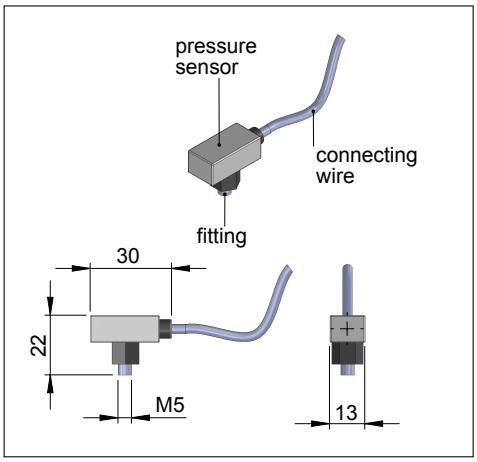

Figure 3.21: Dimensions of pressure sensor SMC PSE-510

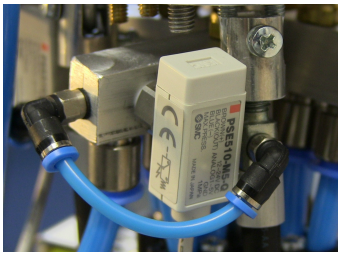

Figure 3.22: Pressure sensor SMC PSE-510

Table 3.7: Specification of pressure sensor

Measurement type	analog, silicon (1-5V)
Ordering designation	PSE510-M5 by SMC
Measuring range	0-10bar
Voltage supply	12-24V
Repeatability	0.3 % F.S. or less
Dimension	30 mm $\times$ 22 mm $\times$ 13 mm
Weight	10 g
Housing material	PBT

3.6.4 Angle sensors – discrete case

Monitoring the kinematic configuration of the discrete worm-like robotic mechanism is implemented by angle sensors, which are attached to the axes of the cardan joints. The cardan joints feature rotatably fixed axes, which are mounted in a centerpiece. Two connecting pieces move against each other and against the axes of this centerpiece. Accordingly, the angle of each axis can be detected using a measuring device fixed to each connecting piece. For this purpose, the axes have to be equipped with a trackable means, such that the measuring device can detect their rotating angle. There are different options, which specific angle sensors could be used. First, it is important that the sensors have to be as small as possible. Second, the sensors should be reliable, available at an affordable price and preferably absolute, i.e. usable without the need of referencing. Rotary encoders according to Table 3.8 were chosen to fulfill the aforementioned requirements. These encoders have to be equipped with diametral magnets that must be fixed to the axes of the cardan joints (cf. Figure 3.23). The distance between the magnet and the encoder IC should be in the range of 0.5 mm up to 1.5 mm, and the center axis of the magnet has to be aligned within a displacement radius of 0.25 mm with respect to the center of the encoder IC. The real encoder with its mounting on an adequate adapter board and the integration within the worm-like setup are depicted in Figure 3.24. In section 5.4 of Chapter 5, the angle control implementation is concerned in detail.

Table 3.8: Specification of rotary encoder

Type	magnetic, absolute, by ams
Ordering designation	AS5145H-HSST SSOP16 LF
Measurement type	contactless
Measuring range	360°
Resolution	12 bit
Voltage supply	3.3/5 V
Integral nonlinearity (optimum)	±0.5°
Integral nonlinearity	±1.4°
Read-out frequency (serial data)	1 MHz
Serial interface	SSI
Magnet	diametral, 6 mm in diameter
Magnet material	NdFeB

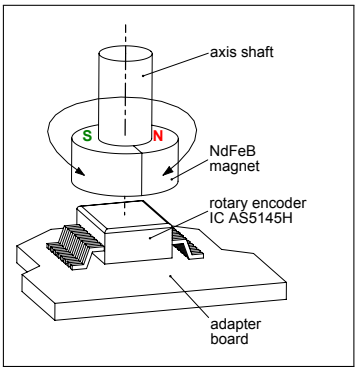

Figure 3.23: Rotary encoder with diametral magnet

(a) Rotary encoder (b) Integration of rotary encoders

Figure 3.24: Angle sensor

3.6.5 Stretch sensors – continuum case

The identification of pose parameters such as curvature and elongation is crucial to calculate the kinematics of the continuum style mechanism. The use of rotary encoders like for the discrete style setup is no longer possible. Instead, a sensor solution has to be considered that is capable of detecting curvature and elongation simultaneously. In this manner, the sensor itself has to be both bendable and ductile. Stretching or contraction of the PAMs are in the range of up to 25 %, which means that sensors such as strain gauges cannot be utilized. An integration of cable sensors or stretch sensors is a reasonable choice, which meet the demands as mentioned before. In this work, stretch sensors are chosen for cost reasons and in order to save installation space. Cable sensors in contrast have to be coupled to multi-turn potentiometers with spring return, which are far larger in scale than the stretch sensors. Such a stretch sensor is based on an extendible polymer string that changes its resistance during extension. However, this kind of sensor has some specificities that require data processing effort. The sensor shows a pronounced hysteresis, i.e. sensor values are dependent on the ”history of motion” and correspond to the relaxation of the sensor material. Once the sensor is elongated, its electric resistance increases. The sensor utilized here (Stretch Sensor by Images Scientific Instruments Inc., USA) doubles its resistance if stretched by 50 %. The relaxation behavior of this resistor is illustrated in Figure 3.25. Figure 3.26 shows the cord sensors attached along the muscle support springs. Concrete hysteresis compensation methods and implementation of this position sensor are covered by section 5.5 of Chapter 5.

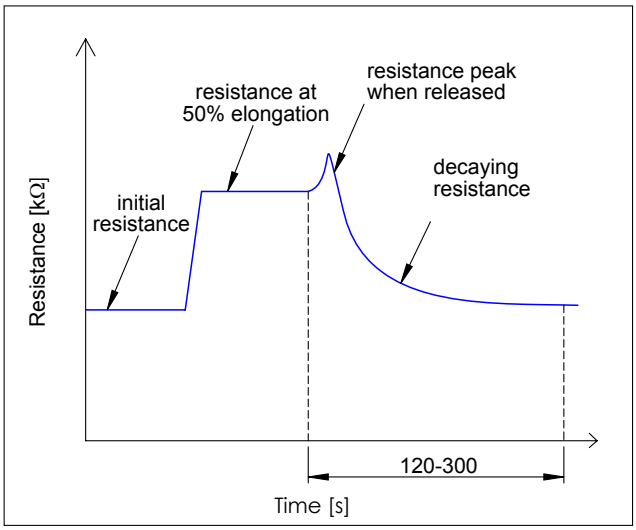

Figure 3.25: Relaxation behavior of stretch sensor (cf. [33])

3.6.6 Gyroscope and acceleration sensor – continuum case

The stretch sensors (cf. subsection 3.6.5) have some limitations in terms of precision and noise. For further enhancing the position, velocity and acceleration sensing, a three DOF gyroscope with a three DOF acceleration sensor is added to the continuum robot segment. The sensor is already integrated in the current setup and used for movement tracking, but an implementation or rather fusion with the corresponding stretch sensor data is part of a later configuration stage.

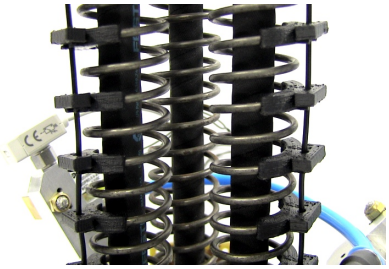

Figure 3.26: Stretch sensors

It is placed on top of the moving plate of each segment. The sensor of choice has a three-axis MEMS gyroscope and a three-axis MEMS accelerometer within one breakout board, both with 16 bit ADCs, signal conditioning and i^2C interface. It is available for a very reasonable price, which is particularly important if a larger number of segments should be equipped. Although in general the three stretch sensors would be enough to measure the position and orientation of the moving plate of a segment, the integration of the gyroscope and acceleration sensor can guarantee a better accuracy for the future. In Table 3.9 all important technical specification data can be seen. An image of the combined sensor mounted on a breakout board is illustrated in Figure 3.27.

Table 3.9: Specification of gyroscope/acceleration sensor

Type	MEMS, 3-axis gyroscope (coriolis effect), 3-axis acceleration
Ordering designation	MPU 6050
Output data arrangement	i^2C, 6-axis motion fusion data
Input voltage	2.3-3.4V
Rate sensor range	$\pm$250 °/s (max. $\pm$2000 °/s)
Accelerometer sensor range	$\pm$2 g (max. $\pm$16 g)
Breakout board dimensions	20 mm $\times$ 16 mm $\times$ 1.6 mm
ADC resolution	16 bit
Max. output data rate gyroscope	8 kHz
Max. output data rate acceleration sensor	1 kHz

3.6.7 Assembly of the segments

Following the previous introduction of all crucial individual components for the robotic prototypes, the next two paragraphs demonstrate how these parts are arranged in units. Two cases must be differentiated again – discrete and continuum case.

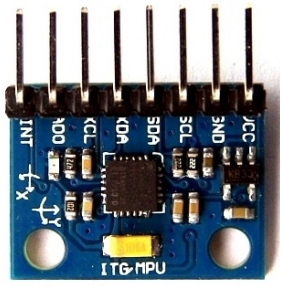

Figure 3.27: Gyroscope/acceleration sensor

Integration – discrete case

The assembly of the aforementioned components for the discrete robot subtype with three segments in a serial arrangement, mounted hanging from a ceiling plate, can be seen in Figure 3.28. A compact setup requires a high integration. It is beneficial to place the valves and the pressure controller boards lengthwise between the PAMs (cf. Figure 3.6 in subsection 3.3.1). The superordinate Arduino segment main controller is put on the bell-shaped plastic support component. At this position is can be connected easily to other segments' Arduino main controller boards to set up a communication network via i^2C.

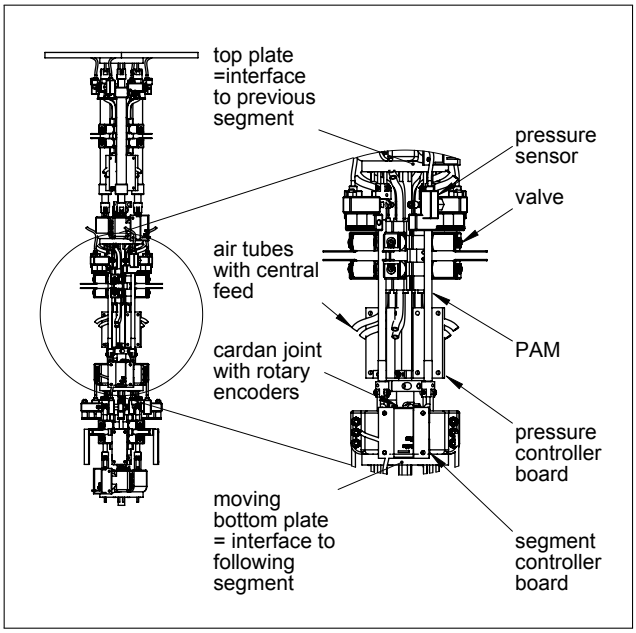

Figure 3.28: Assembly of the segments [34]

A real setup of a first, second and third segment of the discrete worm-like robotic mechanism is depicted in Figure 3.29. These modules can be dimensioned either completely identically in terms of components, length and diameter or they can have different sizes. The difference in size mainly results from integration of various PAM types. For instance, an early prototype utilizes PAM type Festo DMSP-10-160N-RM-CM for the first segment, a second one is equipped with DMSP-5-130N-RM-CM, and a third segment has DMSP-5-50N-RM-CM, which have a nom-

inal length of 160 mm, 130 mm and 50 mm. The idea of using different segments is that they can be dimensioned based on force/torque requirements for a specific position of the segment within the serial kinematic chain. However, the advantage of completely identical segments is that the mechanism becomes 100 % modular, e.g. if only DMSP-10-160N-RM-CM type PAMs are used (cf. Figure 3.29).

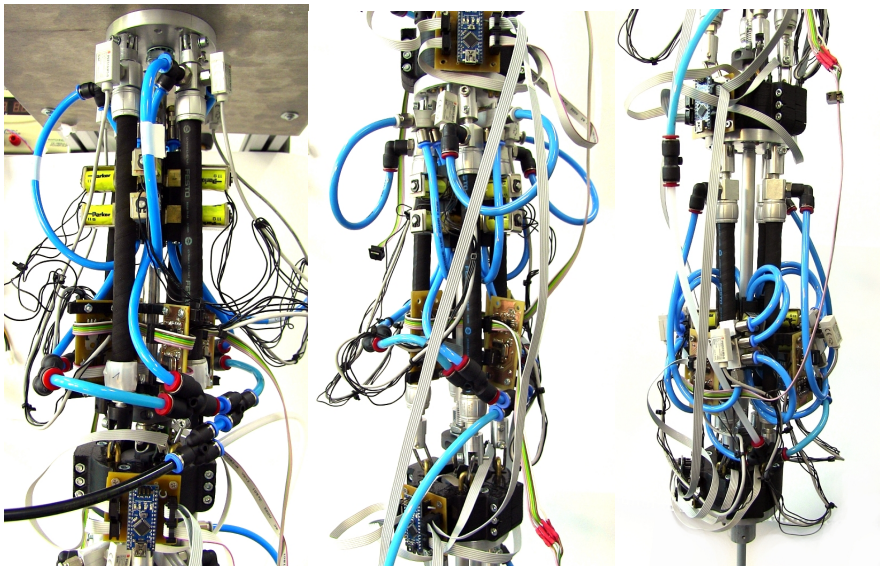

(a) Segment 1 (b) Segment 2 (c) Segment 3

Figure 3.29: Discrete robotic segments with equally equipped PAMs

An arrangement of several segments results in a serial kinematics with four parallel actuators per segment. The setup described is shown in Figure 3.30(a), comprising three equal segments in total. To get a feeling of the movement abilities, Figure 3.30(b) illustrates a movement state that is completely deflected.

A technical specification of the entire assembly of the worm-like robotic mechanism according to Figure 3.30 was already highlighted in Table 3.3, and the masses of all relevant components are given in the appendix (Table A.2).

Integration – continuum case

In contrast to the assembly of the discrete robot, the continuum worm-like robotic mechanism prototype doesn't offer a rigid backbone structure, where any controller boards, valves or other devices can be attached. Thus the integration is even more challenging, since curvature of the entire mechanism affects the fixture of components, in particular influences the ones that are not flexible themselves. In this regard, the placement of controller boards, valves and pressure sensors is crucial. As already introduced in subsection 3.4.2, all of the three pressure controller boards plus the main controller board are fixed horizontally at the bottom of the non-moving plate of each segment. Valves and pressure sensors are placed beside these boards and the PAMs (cf. Figure 3.11). Most of the components of the worm-like robot can be used either for the discrete or for the continuum setup. The continuum mechanism comprises four segments

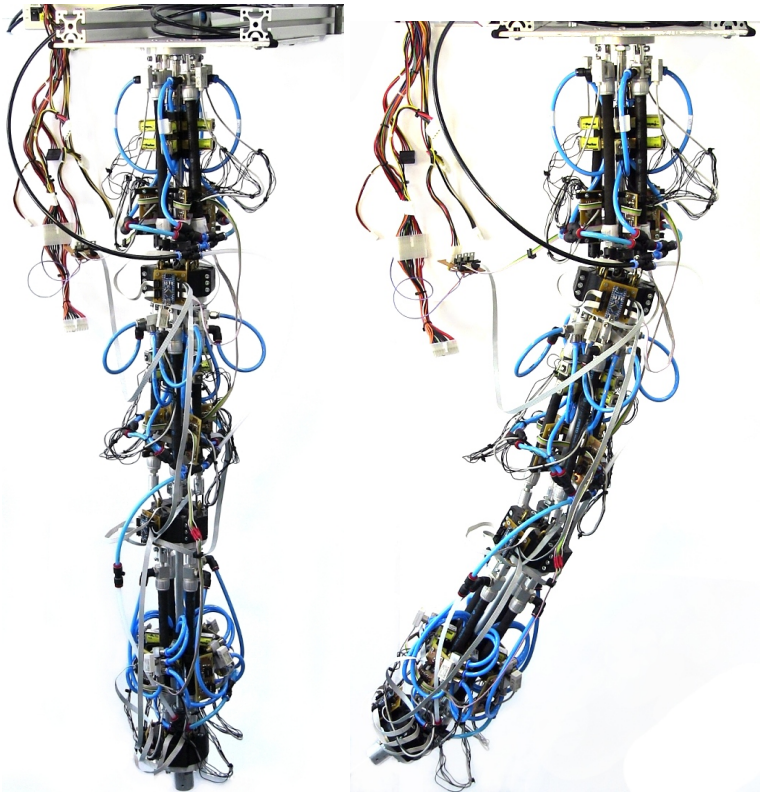

(a) Straight state (b) Deflected state

Figure 3.30: Discrete worm-like robotic mechanism

with three PAMs each, which means 12 PAMs in total, the same number as used for the discrete mechanism. Pneumatic, electrical and mechanical interfaces of each segment are designed to ensure fast module exchange, expansion or reduction. Hence, adequate plug devices are integrated. An arrangement of four serially attached segments is depicted in Figure 3.31. The motion abilities are presented in Figure 3.32, highlighting bending in different directions, shortening and relaxing. Table A.2 in the appendix summarizes the masses of the components of the setup, considering both continuum and discrete case.

3.7 Comparison with known mechanisms

To get a basic estimation about the economic factors and a classification of how the presented mechanisms distance themselves from known mechanisms of the state of research, relevant considerations are shortly discussed in what follows. When looking at the overall costs of the presented mechanisms, it is worth mentioning that the total costs for the setup are based on hardware costs in terms of acquisition costs. If these mechanisms are compared to commercially available robots, the costs for such robots are sales prices, respecting original costs and profit (cf. [35]). The valves utilized are the most expensive components within the entire system, followed by the pressure sensors that are chosen. PAM actuators are only in third place. The overall costs are approximately 4300 Euro for the discrete and 4400 Euro for the continuum robot. For further information, Table A.1 in the appendix sums up the most important

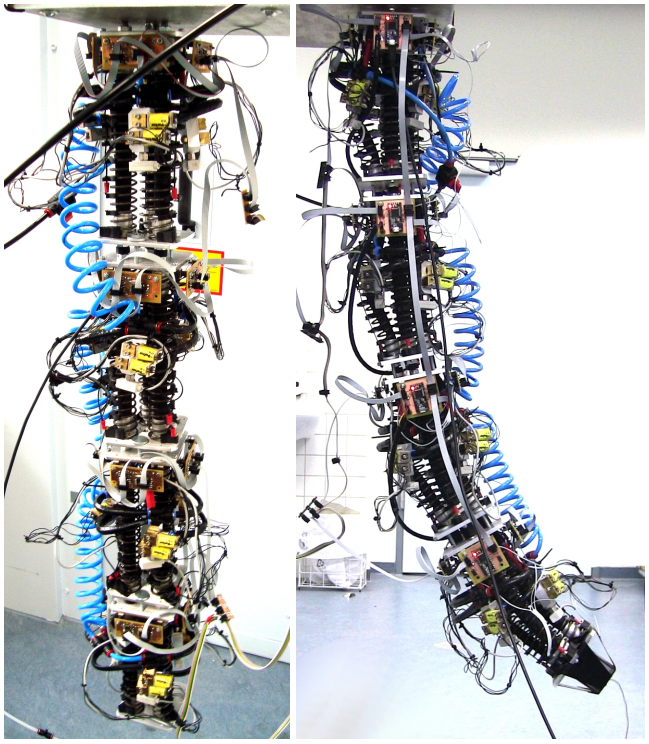

(a) Straight state (b) Deflected state

Figure 3.31: Continuum worm-like robotic mechanism

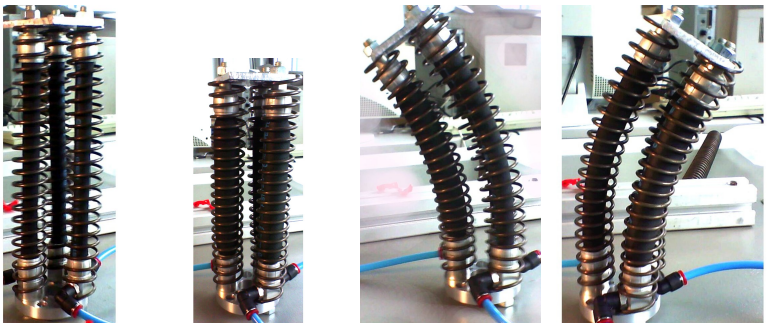

(a) Initial relaxed state (b) Full contraction (c) Bending left (d) Bending right

Figure 3.32: Movement states of continuum segment

cost-incurring components of the worm-like robotic mechanisms.

If one compares the worm-like robotic mechanisms with robots of the state of the art and the state of research, the costs are very low. However, different performance or features of the other types should be taken into account. In particular, the payload, the range of motion, and the precision of motion are decisive factors for differences in costs. Table 3.10 compares the worm-like mechanism with relevant robot arms, with both electric current (Bionic Robotics BioRob, Universal Robots UR5 and UR10, Kuka LWR) and pressurized air (Festo Bionic Handling Assistant BHA, FerRobotics ROMO) used as supply medium (cf. section 2.2). Of course, robots based on electric current or electric drives result in a higher position accuracy, but in contrast to the types with air supply medium, they are not inherently compliant. Compliance therefore must be controlled, which means high control effort. All robotic arms to be compared are compliant mechanisms, either inherently compliant or compliant due to control.

Table 3.10: Comparison of compliant mechanisms

Feature	*Worm discr./cont.*	*BHA*	*BioRob*	*ROMO*	*UR5*	*UR10*	*LWR*
Inherently compliant	yes	yes	yes	yes	no	no	no
DOF	6/12	9	4	5	6	6	7
Actuators	pneumatic	pneumatic	electric	pneumatic	electric	electric	electric
Reach	1050/ 1008 mm	1200 mm	760 mm	2000 mm	850 mm	1300 mm	790 mm
Accuracy	$\pm$8mm	$\pm$10mm [97]	1 mm	$\pm$2 mm	$\pm$0.1 mm	$\pm$0.1 mm	0.05 mm
Maximum velocity	0.6 m/s	n/a	1.0 m/s	n/a	n/a	n/a	n/a
Weight	4.0/4.8 kg	1.8 kg	4.4 kg	n/a	18.4 kg	28.9 kg	16 kg
Payload	1.2 kg	0.5 kg	2 kg	5 kg	5 kg	10 kg	7 kg
Costs (in 1,000 Euro)	4.3/4.4	n/a	29.9	69.5	22	28	$\sim$ 100

Chapter 4

Kinematics and dynamics

The next chapter discusses details about the kinematics and dynamics of the developed worm-like robotic mechanism prototypes. First, only the geometric aspects of the mechanical structures are examined, that is to say the forward kinematics, which is necessary to determine a mechanism's configuration or flange position and orientation. In a second step, the inverse kinematics of the introduced mechanical structures is drawn up. In further sections, the motion dynamics, taking forces and torques into account, is demonstrated and the analysis of motion dynamics is given.

4.1 Worm-like robot forward kinematics

Within the following two subsections the forward kinematics of both the discrete and continuum cases are addressed. The kinematics of the discrete robot is a simple task, the continuum style subtype demands a more sophisticated modeling to cope with the specific characteristics of a curved mechanism.

4.1.1 Forward kinematics – discrete case

The forward kinematics of a discrete serial robotic mechanism is a straightforward task, as the mapping of joint space to Cartesian space is always solvable. Thus, the positions, velocities and accelerations or any higher order derivatives can be determined with respect to either time or any other variables, such as generalized coordinates. The kinematic chain for this mechanism is an open serial kinematics and the motions are rotational movements about the cardan joint axes. All cardan joint dual-axes can be treated as an arrangement of two revolute joints that intersect. Correspondingly, the coordinate frames for both axes of one cardan joint share a common coordinate origin.

A principal task is the identification of frames and building the homogeneous transformation from one frame to the next frame. The homogeneous transformation matrix has the following representation, if Denavit-Hartenberg convention [21] for the forward kinematics is obeyed:

$$ {}_{i-1}T_i = \begin{pmatrix} \cos\theta_i & -\sin\theta_i & 0 & a_{i-1} \\ \sin\theta_i \cos\alpha_{i-1} & \cos\theta_i \cos\alpha_{i-1} & -\sin\alpha_{i-1} & -\sin\alpha_{i-1} d_i \\ \sin\theta_i \sin\alpha_{i-1} & \cos\theta_i \sin\alpha_{i-1} & \cos\alpha_{i-1} & \cos\alpha_{i-1} d_i \\ 0 & 0 & 0 & 1 \end{pmatrix} \quad . \tag{4.1} $$

This representation includes rotations, translations and the origins of the frames, resulting in a 4×4 matrix. The last column deals with the offset of the origins of both frames, where the entry 1 is added. Consequently, the position vectors have the dimension 4×1. In Equation 4.1 ${}_{i-1}T_i$ denotes the transform from a frame i to a frame $i-1$ with the angles θ_i and α_i according to the Denavit-Hartenberg (DH) parameters in Table 4.1. It is worth mentioning that here the proximal version of DH convention is used [18]. This proximal version is characterized by a labeling of the indices, in which two parameters are shifted, such that a relation is established between a current and a previous frame.

By means of a set of four DH parameters a robot can be described in its kinematics. In the case of the present mechanism, all θ_i variables describe revolute joint angle variables, measuring rotations about current z_i axes of frame i. All the other parameters are fixed link parameters that remain constant. a_i gives the link length between two frames i and $i+1$ from z_i to z_{i+1}, which is measured along the x_i axis, α_i refers to the rotational angle about the x_i axis transforming z_i into z_{i+1}, which is also called link twist. The link offset along z_i axis or the distance between x_{i-1} and x_i axes is represented by d_i.

The matrix above (Equation 4.1) is a combination of four basic rotations and translations about or along x_{i-1} and z_i axes, which can also be stated as [18]:

$$ {}_{i-1}T_i = Rot(x_{i-1}, \alpha_i) \cdot Trans(x_{i-1}, a_i) \cdot Rot(z_i, \theta_i) \cdot Trans(z_i, d_i) \quad . \tag{4.2} $$

The expressions in Equations 4.1 and 4.2 can be multiplied, such that a transformation between a serial arrangement of frames can be generated:

$$ {}_0T_n = {}_0T_1 \cdot {}_1T_2 \ldots {}_{n-1}T_n \quad . \tag{4.3} $$

A table of DH parameters as mentioned above is given in 4.1, written in a proximal notation. The choice of frames and parameters is basically not unique, since the convention does not have rules concerning the direction of the joint angle θ_i and also there is some freedom in the choice of the direction of x_i axes if frames are intersecting ($a_i = 0$). In the case of the developed mechanism, a serial kinematics including three cardan joints has to be mapped to appropriate DH parameters. Each cardan joint consists of a pseudo-serial arrangement of two axes, where both the link offset d_i and link length a_i are zero with constant link twist $\alpha_i = \frac{\pi}{2}$ in between. Additionally, each segment of the presented discrete worm-like robotic mechanism has a twist of $\frac{\pi}{4}$, which has to be considered within the α_i-terms of the DH parameters. The frames of Table 4.1 can be seen in Figure 4.1, showing all three segments of the discrete worm-like mechanism prototype with three cardan joints and six coordinate frames oriented according to the DH convention.

Table 4.1: Denavit-Hartenberg parameters

Joint	a_{i-1}	α_{i-1}	d_i	θ_i
0	l_0	$-\frac{\pi}{4}$	0	θ_0
1	0	$\frac{\pi}{2}$	0	θ_1
2	l_1	$-\frac{\pi}{4}$	0	θ_2
3	0	$\frac{\pi}{2}$	0	θ_3
4	l_2	$-\frac{\pi}{4}$	0	θ_4
5	0	$\frac{\pi}{2}$	0	θ_5

4.1.2 Forward kinematics – continuum case

The calculation of the forward kinematics of a mechanism of which the segments are characterized by a curvature is not as straightforward as in the previous case of the discrete system. In particular, the challenge is to transfer corresponding sensor values into a kinematic model that approximates the pose of each segment with best precision. As introduced in subsection 3.6.5, the evaluation of the stretch sensor data to measure the outer contour and thereby the position and orientation of the top plate of each segment is the key to get an estimation of the kinematics. One continuum style segment can be divided into three parts: (1) fixed rigid bottom plate, (2) continuously curved flexible PAM part, (3) moving rigid top plate (cf. Figure 3.11).

To deal with a kinematic redundancy [142] and an actually ”infinite-degree-of-freedom structure” [114] of a continuum robot, simplifications have to be made. Unlike the Bionic Handling Assistant BHA with its multi-layer actuators, which can be modeled using so-called Unit-Kinematics [97, 98, 99], a different approach is necessary for the continuum worm-like mechanism. The assumption that a continuously curved arc is a reasonable model of the flexible PAM part can be proven by experiments. Also state-of-the-art literature, such as [52, 77, 78, 131, 158], claim the significance of this approach. The idea behind is to simplify the shape model of the curved mechanism, such that all three DOF of one segment can be mapped by only three sensors, in spite of actually having a six DOF coordinate transform in between. This is why the assumption of a constant curvature within one segment has to be made, which constraints the mapping. The arc can also be seen as a segment of a torus (cf. [131]), which has a torus radius r_T that corresponds to the reciprocal value of the segment curvature $\kappa = r_T^{-1}$, a torus segment cross section radius r_S, a torus segment angle Θ, as well as a torus segment orientation angle Φ (cf. Figure 4.2).

Calculating the transformation between the fixed rigid bottom plate of one continuum segment to the moving rigid top plate is essential for solving the forward kinematics problem. This is done making use of three stretch sensors that are aligned with each PAM, i.e. if the PAM curves or elongates/shortens, the attached sensor moves correspondingly. The idea of the torus segment approach is to compute the transformation out of the lengths l_1, l_2 and l_3 of the three PAMs of each segment, which are determined with a stretch sensor each. Figure 4.3 highlights the frames of each segment together with its PAM lengths and transformation annotations.

All three PAM length values are the basis for the calculation of the relevant kinematic parameters r_T, Θ and Φ. For convenience a mean segment length l_S and a length squared difference term

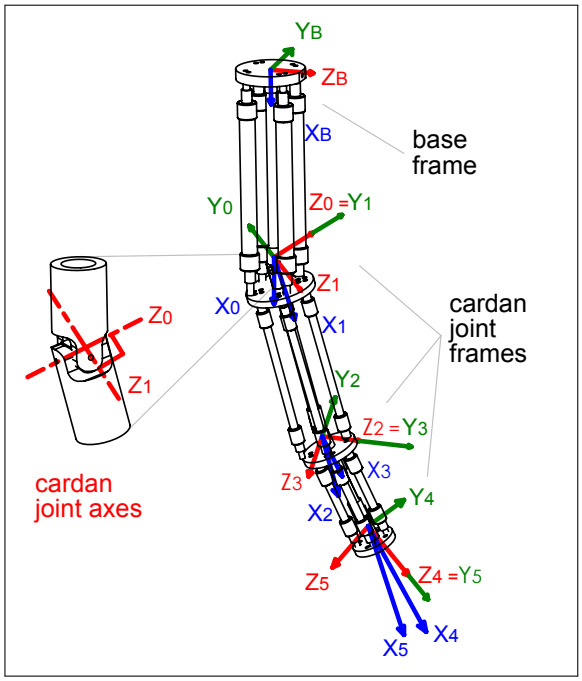

Figure 4.1: Robot frames – discrete case [34]

g are defined as follows [77, 78, 131]:

$$l_S = \frac{\sum_{i=1}^{3} l_i}{3} \quad , \tag{4.4}$$

$$g = \sqrt{l_1^2 + l_2^2 + l_3^2 - l_1 l_2 - l_1 l_3 - l_2 l_3} \quad . \tag{4.5}$$

With both Equations 4.4 and 4.5 the kinematic parameters can be derived:

$$r_T = \frac{3 l_S r_S}{2g} \quad , \tag{4.6}$$

$$\Theta = \frac{2g}{3 r_S} \quad , \tag{4.7}$$

$$\Phi = \tan^{-1}\left(\frac{\sqrt{3}(l_3 - l_2)}{l_2 + l_3 - 2l_1}\right) \quad . \tag{4.8}$$

The coordinate transformation of a given point p_{i-1} into a point p_i can be split in two pieces – a rotational part R^i_{i-1}, which deals with rotations between two frames during transformation and an offset part D^i_{i-1}, which is responsible for shifting the coordinate frame origin:

$$p_i = R^i_{i-1}(\Theta, \Phi) \cdot p_{i-1} + D^i_{i-1}(r_T, \Theta, \Phi) \quad , \tag{4.9}$$

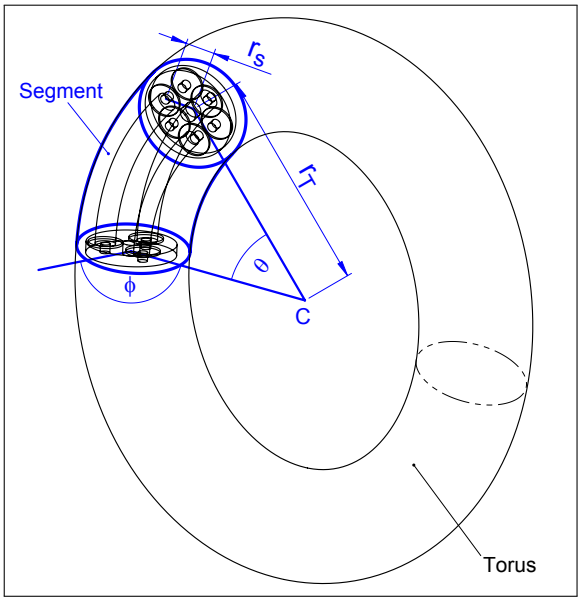

Figure 4.2: Torus approach (cf. [131])

with

$$
\begin{aligned}
R^i_{i-1}(\Theta,\Phi) &= R_z(\Phi)\cdot R_y(-\Theta)\cdot R_z(-\Phi) \\
&= \begin{pmatrix} \cos\Phi & -\sin\Phi & 0 \\ \sin\Phi & \cos\Phi & 0 \\ 0 & 0 & 1 \end{pmatrix} \cdot \begin{pmatrix} \cos(-\Theta) & 0 & \sin(-\Theta) \\ 0 & 1 & 0 \\ -\sin(-\Theta) & 0 & \cos(-\Theta) \end{pmatrix} \cdot \\
&\quad \begin{pmatrix} \cos(-\Phi) & -\sin(-\Phi) & 0 \\ \sin(-\Phi) & \cos(-\Phi) & 0 \\ 0 & 0 & 1 \end{pmatrix}
\end{aligned} \tag{4.10}
$$

and

$$
D^i_{i-1}(r_T,\Theta,\Phi) = \begin{pmatrix} 2r_T \sin\left(\frac{\Theta}{2}\right)\cos\left(\frac{\pi-\Theta}{2}\right)\sin\left(\Phi-\frac{\pi}{2}\right) \\ -2r_T \sin\left(\frac{\Theta}{2}\right)\cos\left(\frac{\pi-\Theta}{2}\right)\cos\left(\Phi-\frac{\pi}{2}\right) \\ 2r_T \sin\left(\frac{\Theta}{2}\right)\sin\left(\frac{\pi-\Theta}{2}\right) \end{pmatrix} \quad . \tag{4.11}
$$

Unfortunately, the equations above imply serious challenges in terms of numeric stability, which happens in case of very high values for r_T, i.e. if Θ goes to zero or if Φ is undefined. In these cases, the subsequent equations for $D^i_{i-1}(\Theta,\Phi)$ can be derived to treat such a singular configuration (cf. [131]):

$$
D^i_{i-1}(\Theta,\Phi) = \begin{pmatrix} l_S \sin X\left(\frac{\Theta}{2}\right)\cos\left(\frac{\pi-\Theta}{2}\right)\sin\left(\Phi-\frac{\pi}{2}\right) \\ -l_S \sin X\left(\frac{\Theta}{2}\right)\cos\left(\frac{\pi-\Theta}{2}\right)\cos\left(\Phi-\frac{\pi}{2}\right) \\ l_S \sin X\left(\frac{\Theta}{2}\right)\sin\left(\frac{\pi-\Theta}{2}\right) \end{pmatrix} \quad , \tag{4.12}
$$

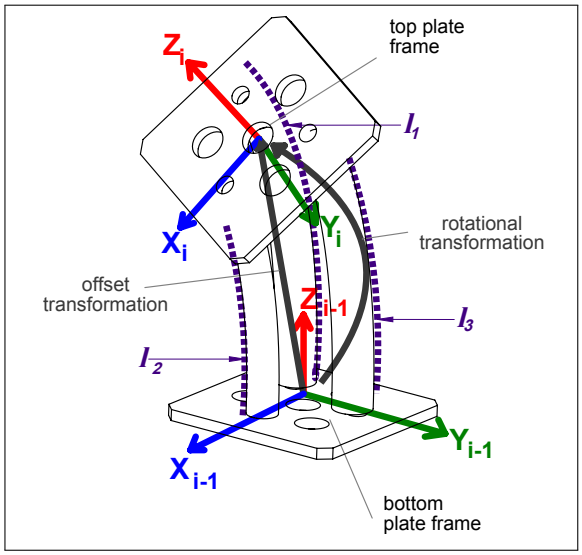

Figure 4.3: Robot frames – continuum case

with the replacement function $sinX$ [33, 131]:

$$\sin X = \left\{ \begin{array}{ll} 1, & \text{if } \sin(\frac{\Theta}{2}) = 0.0 \bigwedge |\frac{\Theta}{2}| < \pi \\ \frac{\sin(\frac{\Theta}{2})}{\frac{\Theta}{2}}, & \text{else} \end{array} \right\} \quad . \tag{4.13}$$

The replacement function serves as a simple switch that activates the fallback solution if $sin(\frac{\Theta}{2})$ goes to zero, i.e. in the case that the radius r_T of the torus segment becomes infinite or in other words, the segment is in a stretched position. Else the normal calculation of $sin(\frac{\Theta}{2})/\frac{\Theta}{2}$ is performed. In this way, the function tests numerically problematic $\frac{\Theta}{2}$ values, when the sine becomes zero, which also implies that the argument $\frac{\Theta}{2}$ itself becomes zero. If the limit case occurs, the rotation matrix R^i_{i-1} degenerates to an identity matrix and the offset part D^i_{i-1} gets zero values for its x and y components.

To generate the forward kinematics for the continuum case robot prototype, the previous transformation (Equations 4.9 - 4.13) has to be set up for each segment, and then these transformations are multiplied, in a similar way as already shown in Equation 4.3 of the previous subsection 4.1.1.

4.2 Worm-like robot inverse kinematics

Within section 4.1 the question of computing the mechanism's flange position was focused, which is a straightforward task for a discrete robot and a more difficult task in a continuum style robot case. In the next section the problem of the inverse kinematics is addressed. The effort of mapping Cartesian space to joint space for the serially arranged robots presented here is much higher than vice versa. Given specific positions and orientations of the flange of the robotic mechanism, a set of joint angles or muscle lengths should be determined, such that it is feasible to reach the point of interest. The latter arises the question if there is a solution for a specific position and orientation in Cartesian space at all or if this point is outside the reach

or workspace of the robot. Besides, there is the problem that certain positions/orientations of the mechanisms can be realized with different kinematic configurations. In literature this issue is called ”multiple solutions” [18]. Additionally to such issues, singularities might exist within the workspace of the robot, which have to be handled during control.

In general, it is desirable to have closed-form inverse kinematics solutions, which are faster than numerical solutions. However, these closed-form solutions only exist for specific robotic structures, such as six DOF kinematics, which either have three consecutive revolute joint axes intersecting at a common point or three consecutive revolute axes being parallel [143]. Since the robot structures presented in this thesis are of a different kind, such closed-form solutions don't exist.

4.2.1 Inverse kinematics – discrete case

The discrete worm-like robotic mechanism of this thesis is a serial robot, which has two DOF per segment, actuated by means of two perpendicular antagonistic pairs of PAMs, i.e. the setup with three segments comprises six DOF in total. The mechanism claims to be modular and expansible, and also the number of segments varies. Thus, an inverse kinematics approach should be as modular as possible.

Each segment is characterized by a cardan joint with two perpendicularly intersecting rotational joints. The following segment's double joint has an offset to the previous double joint, such that there is only a pairwise intersection of robot axes. In this way, the prevalent six DOF robot doesn't have three axes intersecting at a single point, which would be necessary for the existence of a closed-form inverse kinematics solution [17]. It can already be estimated from Figure 4.1 and 4.4 that such a mechanism reaches exactly the same flange position and orientation with infinite different configurations. Thus, there is no closed-form solution possible for the presented type of discrete worm-like robotic mechanism.

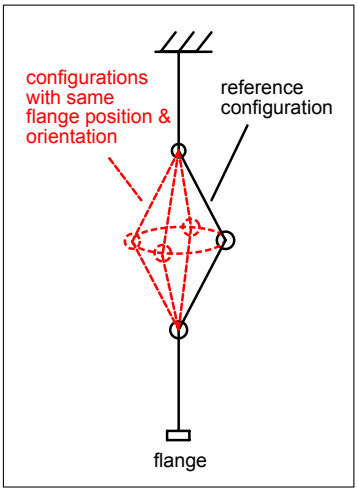

Figure 4.4: Multiple solutions – discrete case

Instead, numerical or recursive methods can help to solve the inverse kinematics problem. Two different kinds of approaches are discussed in what follows.

One possible numerical method is an iterative optimization approach, which is easy to implement in current software environments, e.g. Matlab (cf. [137]). The idea is to transfer the inverse problem into a constrained nonlinear optimization problem. These iterative optimization algorithms try to find a set of joint values q_i such that a desired flange position and orientation is reached, which means that Cartesian space is mapped to joint space. The delta between the desired and the calculated position or orientation is minimized, starting with a speculation in a first iterative step. Since there are many different solutions possible with different geometric configurations, additional constraints have to be integrated. One reasonable constraint is the limitation of the joint angles, which are mechanically restricted due to the maximum contraction of the PAMs, which results in maximum possible joint angles q_{max} or q_{min}. Another constraint can be set to minimize the overall deflection of the robot, such that the sum of the squares of the joint angles $min(\sum q_i^2)$ remains small. This also helps to save energy, because large deflections are more power consuming, as the PAMs have to be filled/exhausted to a greater extent, which means more consumption of electricity and compressed air. There might be the case that the desired pose is out of range, i.e. cannot be reached with the prevalent kinematics and thus would exceed the workspace. This suggests that the optimization problem can be formulated with an additional secondary condition that minimizes the offset between a desired and a calculated pose. The desired pose does not necessarily have to be reached.

In this way, the optimization problem can be defined as follows:

$$\begin{aligned} min((x_{des} - x_{calc}(q_i))^T (x_{des} - x_{calc}(q_i))) \quad &, \\ q_{min} < q_i < q_{max} \quad &, \\ min(\sum q_i^2) \quad &. \end{aligned} \tag{4.14}$$

For instance, such a nonlinear optimization problem can be solved using Matlab $fmincon$ command, which activates a gradient-based method. It can treat objective and constraint functions that are continuous and have continuous first derivatives.[1]

Another approach is based on a recursive algorithm, which tries to find the inverse kinematics by testing segment angle configurations, starting with the base segment (cf. [136]). The algorithm aims to set each angle of the mechanism's segments such that an imaginary line (see blue lines in Figure 4.5) between the segment and the target position is followed by the subsequent segment. An iterative calculation rule is used to find appropriate test angles θ_i according to the following equation:

$$\theta_i^{initial} = \frac{1}{\cos \frac{\sqrt{p_x^2 + p_y^2}}{||p||}} \quad . \tag{4.15}$$

The algorithm starts at the base of the robot at an initial position $\theta_0^{initial}$ according to Equation 4.15, and tries to gradually align the subsequent segments, such that an imaginary line between the current joint and the target position becomes collinear to the segment's longitudinal axis. Gradually all the segments are tested in the same manner. If the position reached is not close enough to the target position (below a predefined error ε), the algorithm gets back recursively and increases/decreases the angle values of the joints until the error is within the tolerance. In order to improve the efficiency, the algorithm can be implemented in a way that the testing starts with angles that align the entire mechanism in a plane that is defined by three

[1] cf. http://www.mathworks.de/de/help/optim/ug/fmincon.html

points – the base, the current joint and the target point. Hence, a 3D problem in space is scaled down to a 2D problem. Also a test if the sum of all subsequent segment lengths is more or less than the distance between the actual joint and the target point can cause early termination of the current recursion step, which initiates a return to the previous segment joint. Besides, feasible maximum angles θ_{imax} have to be considered within the algorithm, which is another boundary condition. As a matter of principle, the computation effort for this algorithm depends on the step width of the angle increments that are tested. This width has to be a trade-off between calculation time and precision, since large step width might result in calculated end positions that are too far from the desired target position and thus don't meet the error tolerance requirements. Figure 4.5 depicts the idea behind this algorithm, using the aforementioned connecting lines (blue) that finally result in segment orientations (green) to reach the target within a certain error ε (red).

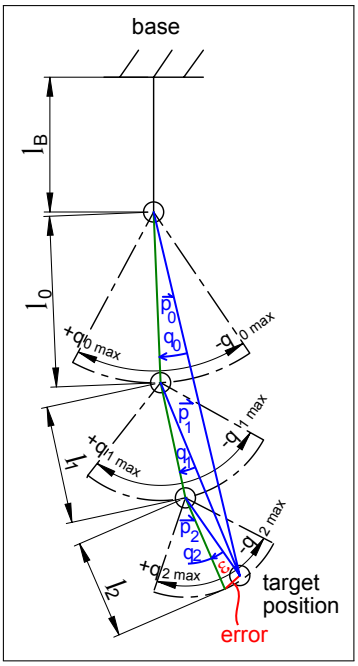

Figure 4.5: Principle of recursive algorithm

4.2.2 Inverse kinematics – continuum case

Similar to the discrete robot prototype, the continuum style mechanism is characterized by a serial arrangement of segments actuated by PAMs, but here each segment has three DOF, two revolute DOF plus one prismatic DOF. The latter is due to the ability of the mechanism segment to elongate or shorten along its central neutral fiber. In the prevalent prototype up to four segments are modularly coupled to one another, which are actuated by three PAMs per segment, building a triangular setup with 120° in between. Unlike other continuum robots with only bending abilities, i.e. two rotational DOF per segment such as [61, 114], for which analytic solutions can be found, there is no closed-form solution available for the inverse kinematics of the prevalent continuum style robot. The inverse issue is even more challenging than for the discrete case, as there is an additional DOF per segment. This DOF causes numerical

problems in case of pure elongation or shortening, i.e. if the segment is in a non-curved straight pose. Evidently, this problem can be shown in a similar way as within the discrete setup (cf. Figure 4.6).

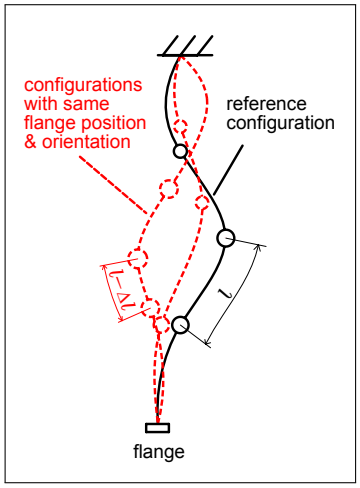

Figure 4.6: Multiple solutions – continuum case

Again, a numerical solution is the method of choice. Attention has to be paid to computation effort, performance and stability. As the computing power is very limited on the decentrally arranged microcontroller boards, the inverse kinematics has to be treated on a more powerful unit, for instance with a control PC.

Referring to the state of research, e.g. [127, 130, 132], learning algorithms can be extremely helpful if fast and precise control is to be achieved, in particular in the case of high-dimensional setups, i.e. large robotic mechanisms with lots of segments and a large number of DOF. The online goal babbling approach of [132] is a reasonable way to handle the inverse kinematics issue for the prevalent multi-section continuum robot. The approach is based on the idea that actuator commands q_t are monitored over certain time steps t, taking the geometric effect on the robot's pose p_t into account. To start the algorithm, an initial inverse estimate $g(p_0^*, \xi_0)$ is necessary that satisfies the equation

$$p_t = f(q_t) \quad , \tag{4.16}$$

which allows to generate further inverse estimates in order to approach the target position p_t^*. In this way, the required values q_t can be estimated:

$$q_t = g(p_t^*, \xi_t) + E_t(p_t^*) \quad , \tag{4.17}$$

with ξ_t as a function parameter and $E_t(p_t^*)$ as a noise term, which is used for performance reasons. Based on this equation, also trajectories can be generated, implementing of a set of values that should be reached. Here it is useful to add weighting functions w_t (cf. [132]) to the exploration algorithm, by means of which learning steps can be influenced, such that configurations are preferred that can be handled with minimum energy or, in other words, result in maximum flange movements triggered by minimum joint movements. Furthermore, weighting functions can also include mathematical means to guarantee the right movement direction in the estimation process. The final inverse kinematics estimate $g(p_t^*)$ is implemented as a linear

combination of linear functions that are only in use within the local sphere of action of their so-called prototype vectors (cf. [132]). After each time step t the inverse estimate is adapted such that the weighted square error

$$E_w^Q = w_t \cdot \|q_t - g(p_t)\|^2 \tag{4.18}$$

is minimized. Last but not least an online gradient descent is used to refresh the aforementioned function parameters ξ_t.

4.2.3 Workspace

For the design of robots it is important to consider movement abilities and geometric range. It is crucial to know which positions in space can be reached by a manipulator and also there is the question about the orientations of the manipulator's flange at these positions. Quite a lot of industrial robots are based on the idea that positioning and orientation should be two decoupled tasks such that most of the six DOF articulated robot arms are equipped with a wrist that integrates the last three axes intersecting at a common point. Usually the workspace of such a robot features symmetries, as joint angle restrictions are often mirror-angled in two directions starting at a home configuration, which is due to mechanical or wiring reasons. The workspace gives some indication about the robot's versatility and thus it is always decisive to meet workspace requirements in order to fulfill the corresponding range of duty. To get a reasonable estimation about what the mechanism's boundaries are, below a workspace analysis is accomplished for both the discrete and the continuum mechanism.

The length sum of a robot, based on link length and joint offset as introduced in Table 4.1, already gives a first evaluation of the overall dimension of a robot:

$$\sum_{i=1}^{N}(a_{i-1} + d_i) \quad . \tag{4.19}$$

The discrete robot with three serial segments results in a length sum of $280 + 350 + 350 + 70 + l_{tool} = 1050 + l_{tool}[mm]$, the continuum system with four equal segments has a dimension of $4 \times 252 + l_{tool} = 1008 + l_{tool}[mm]$.

However, the length sum according to Equation 4.19 doesn't consider the workspace of the robot. It is only useful to get a very rough estimation about how the maximum geometric reach looks like. In that sense the sum gives the total length of the mechanism in case of a completely stretched configuration. In the case of the presented worm-like robotic mechanisms, the workspace is a reachable workspace, which has to be distinguished from a dexterous workspace. The reachable workspace is defined by all the points in space that can be reached by the robot, whereas the dexterous workspace is a subspace in which all points have to be reached in arbitrary orientation. Although the worm-like mechanism has six actuated DOF in the discrete case and 12 DOF in the continuum case, the resulting DOF for the motion of the end-effector is less due to the redundancy of the joint arrangement. The dexterous workspace of the mechanisms is zero, the reachable workspace is illustrated in Figure 4.7 – shown for the discrete case. To be more precise, this figure shows the side view of the workspace, i.e. a 2D projection, which is actually a 3D workspace that is rotationally symmetrical[2] with respect to the central vertical axis.

[2] in a good approximation

As it can be seen in this figure, the workspace of the discrete setup has a shape similar to a saucer. The stroke of the mechanism is about 75 mm, the total angular movement of the entire mechanism is $\pm 27°$, and the total absolute angular movement of the end-effector is $3 \times \pm 16°$. One extreme configuration of the discrete worm-like mechanism is indicated with a blue line. In this extreme configuration the two angles of each cardan joint of all three segments reach their maximum deflection at 16°, which means that the entire setup's curvature has its maximum.

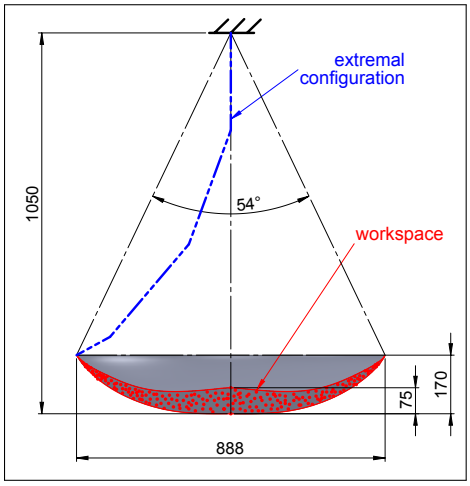

Figure 4.7: Reachable workspace – discrete case [34]

Another question that is tightly connected to the workspace of the discrete robot prototype is related to the joint angles that are feasible. These joint angles clearly influence the robot's workspace, but the joint angles themselves of course are affected by PAM type and lever arm. Figure 4.8 depicts the correlation between PAM membrane length, lever arm (i.e. the distance between the mounting point of the PAM and the cardan joint axis) and resulting joint angle. The reference for this figure is a Festo DMSP-10-160-RM-CM muscle with a lever arm of 30 mm, which is used in the prevalent setup (black line). One can see that for smaller ranges of lever arm an increase of the lever arm also increases the joint angle. The reason for this is the nonlinear behavior of the muscles. More lever arm means less force that is necessary to generate a certain torque at the joint. On the other hand more lever arm means more contraction that is necessary to result in the same angular position. The correlation between contraction and resulting force is nonlinear, and feasible joint angles are nonlinear with respect to the contraction as well. However, a practical joint angle limit can be set at about 45°, where the cardan joint and the rotary encoders mounted on the joints' axes cause a mechanical barrier or rotation limit. One can further compare different kinds of PAMs with respect to their diameter. Figure 4.9 gives an estimation about which joint angles can be reached with different PAM types (5 mm, 10 mm, 20 mm, and 40 mm inner diameter). Larger muscles generate higher forces and increased joint angles. However, compared to their absolute peaks, a steep decrease of these angles can be determined using PAM sizes 20 and 40. Muscle types DMSP-5 are very weak (only 135 N max. force) and unsuitable for mechanisms in the dimension range as presented within this thesis. As a compromise, DMSP-10 PAMs can generate acceptable joint angles and forces with reasonable lever arms.

Regarding a single continuum worm-like mechanism segment, both x- and y-axis movements

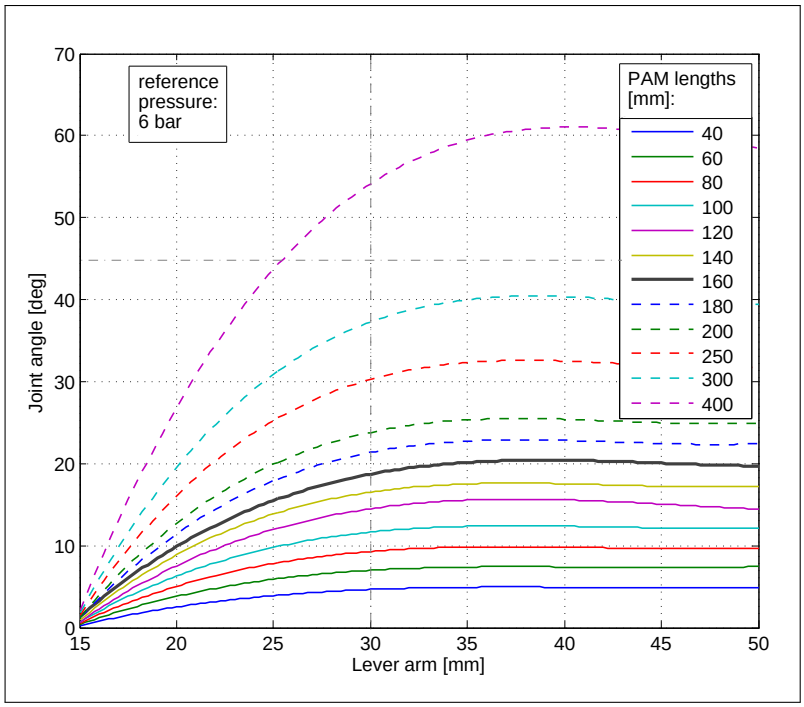

Figure 4.8: Feasible joint angles

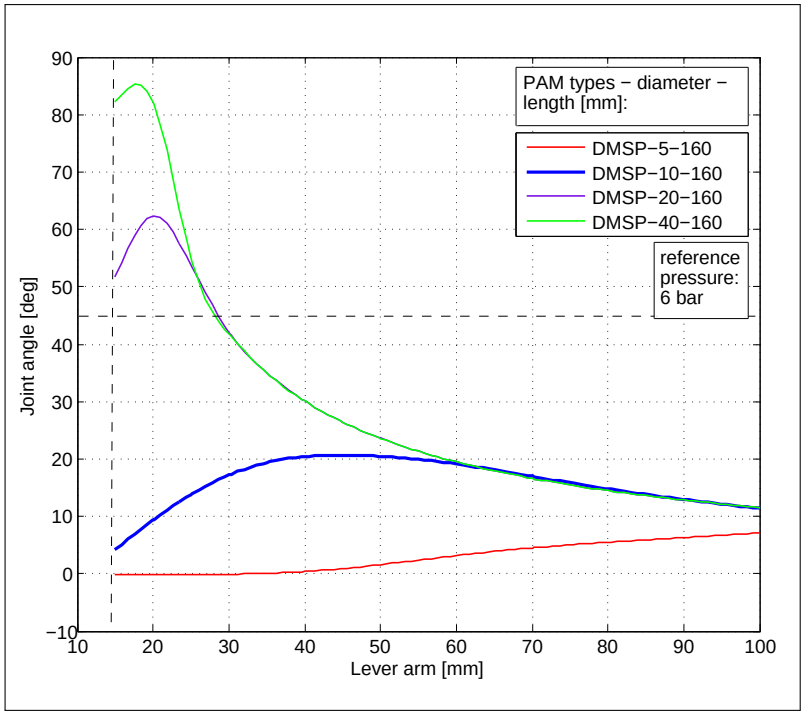

Figure 4.9: Comparison of PAMs

(right and left, back and forth) are in the range of $\pm$80 mm, z-axis motions (up and down) are feasible within 40 mm, which together results in a spherical shell as a first approximation. If several segments are attached to a worm-like mechanism, this spherical shell is magnified and the workspace enlarges widely. A 3D model of this shell is given in Figure 4.10, which integrates a 2D cross section in (a) and the corresponding 3D representation in (b). More on this can be found later on in subsections 6.2.1 and 6.2.2, in which positions and orientations of the continuum style segments including their derivatives are discussed in a detailed manner.

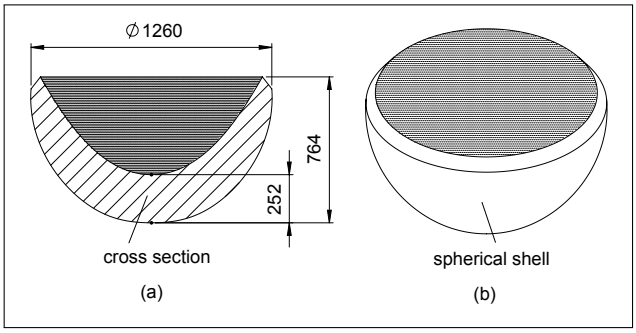

Figure 4.10: Reachable Workspace – continuum case

Additionally, it has to be considered that there are ”dead zones” (cf. [114]) within the kinematic chain of the continuum worm-like robotic mechanism, which are not flexible and thus, neither bending nor shortening/extending is possible. In order to minimize these dead zones, the distance between each of the continuum style segments should be as short as possible. Also it is plausible that the ratio of active and dead zones is influenced by the effective length of the PAMs, i.e. the length of the rubber tubes of the PAMs that really changes the robot's motion configuration.

4.3 Dynamics

This section gives a short outlook with respect to the dynamics of the worm-like mechanisms, in particular the set of differential equations of motions. Similar to the approach within the forward kinematics in section 4.1, each of the serially arranged links of the entire system has to be considered, such that a system of equations arises. With every single DOF the dimension of this system of equations increases. According to [18], the general dynamic equations can be written as follows:

$$\tau = M(\Theta) \cdot \ddot{\Theta} + V(\Theta, \dot{\Theta}) + G(\Theta) \quad , \tag{4.20}$$

in which $M(\Theta)$ is the mass matrix, $V(\Theta, \dot{\Theta})$ represents a velocity-dependent vector of centrifugal and Coriolis terms, and $G(\Theta)$ includes gravity components.

To result in corresponding differential equations of motion, both Newton-Euler and Lagrange formulations of the second kind (II) are common practice. For small systems, which means systems with only a low number of DOF, the Lagrange II approach is effective. However, for

systems with a high number of DOF, the calculation of partial derivatives is cost-intensive. In this manner, the projective Newton-Euler method is more practicable:

$$\sum_{i=1}^{n} \left[J_{T,i}^{T}(\dot{p}_i - F_{e,i}) + J_{R,i}^{T}(\dot{L}_i - M_{e,i}) \right] = 0 \quad , \tag{4.21}$$

with the following components:

- n – number of bodies,
- i – i^{th} body,
- $J_{T,i} = \frac{\partial \dot{r}_{0s}}{\partial \dot{q}}$ – the Jacobian of translation (for inertial systems: $J_T = \frac{\partial \dot{r}_{0s}}{\partial \dot{q}} = \frac{\partial r_{0s}}{\partial q}$),
- $\dot{p}_i = m_i \ddot{r}_{0s,i}$ – momentum change,
- $F_{e,i}$ – active forces,
- $J_{R,i} = \frac{\partial \omega_{0s}}{\partial \dot{q}}$ – the Jacobian of rotation,
- $\dot{L}_i$ – change in angular momentum,
- $M_{e,i}$ – active torques or transverse momentum.

Nevertheless, the representation of the Newton-Euler approach in Equation 4.21 is not very practical in case that forces or torques have to be calculated for a given position and acceleration ($\ddot{q}(\dot{q}, q)$). Accordingly, an appropriate change in the general motion equation that separates $\ddot{q}$ becomes:

$$M(q) \cdot \ddot{q} + h(q, \dot{q}) = Q_{ft} \quad , \tag{4.22}$$

with $M(q)$ being the mass matrix of the system and $h(q, \dot{q})$ being the vector of all forces excluding Q_{ft}, which represents the driving forces and torques.

These dynamic relationships can be utilized to enhance the robot control, which is presented in the following Chapter 5 or in section 5.2 dealing with the calibration of the PAMs including force considerations within an initially static condition. Such enhancements are of interest for application scenarios with fast movements, i.e. high velocities and accelerations. Also they can be used together with the knowledge gained in section 4.4 hereinafter.

Examples of inertia matrices for a discrete robotic worm-like mechanism with three segments are listed in Table 4.2, which are necessary for the calculation of the dynamic equations. Axis x and y are the joint axes, and z is in direction along the frame structure from one cardan joint to the next one, i.e. body-fixed reference frames are chosen with respect to the intersection of the two cardan joint axes. Similar tables can be generated for all four segments of the continuum worm-like robotic mechanism.

As a stage of expansion for the dynamics of the continuum worm-like robotic mechanism, an enhanced approach dealing with the principle of virtual power (cf. [133]) based on Kane's method (cf. [79]) might be implemented, which is not part of the current work within this thesis. Also there is related work that considers an exact Cosserat rod theory model for soft robotic manipulators, which incorporates gravitational loads of the mechanism's segments and resulting shear strains [151]. In this respect, it should be noted that there is recent literature including Euler-Bernoulli beam models for accurate flexible manipulators modeling, analysis and optimal design [50]. Again, such models would go beyond the constraints of this dissertation.

Table 4.2: Inertias and masses – discrete case

Segment 1 [gmm^2]		
$I_{xx} = 22765248.81$	$I_{xy} = 11440.78$	$I_{xz} = 11644.79$
$I_{yx} = 11440.78$	$I_{yy} = 22762970.46$	$I_{yz} = -11259.91$
$I_{zx} = 11644.79$	$I_{zy} = -11259.91$	$I_{zz} = 1154836.01$
$m = 1307g$		
Segment 2 [gmm^2]		
$I_{xx} = 16607376.84$	$I_{xy} = 11309.33$	$I_{xz} = 11515.78$
$I_{yx} = 11309.33$	$I_{yy} = 16603231.37$	$I_{yz} = -10725.45$
$I_{zx} = 11515.78$	$I_{zy} = -10725.45$	$I_{zz} = 1310595.84$
$m = 1261g$		
Segment 3 [gmm^2]		
$I_{xx} = 585521.99$	$I_{xy} = -11329.14$	$I_{xz} = 12274.81$
$I_{yx} = -11329.14$	$I_{yy} = 589101.41$	$I_{yz} = 13092.94$
$I_{zx} = 12274.81$	$I_{zy} = 13092.94$	$I_{zz} = 344383.69$
$m = 340g$		

4.4 Model-based enhancements

To enhance the control quality for the worm-like robotic mechanisms, parameters such as stiffness, damping and friction shall be taken into account within the following paragraphs. Purely theoretically estimated parameters have the drawback of questionable validness, especially for the case of highly integrated systems that combine lots of different single components. This way, parameters are hard to identify (e.g. damping of the PAMs). Hence, parameter identification is conducted by means of experiments.

As far as the stiffness parameter identification is concerned, the work is already done within the muscle calibration, which is presented later on in section 5.2. This muscle calibration combines characteristics about contraction, force and pressure of the PAM. Considering the changes in force and contraction, an equivalent spring stiffness c can be determined. It is interpreted as a rotational stiffness c_T with respect to the cardan joint motion, considering the torques T generated by the muscle forces as a pair including their lever arms and the resulting changes of the rotational angle α. This spring stiffness is dependent on the pressure of the PAM and denotes as follows:

$$c_T(p) = \frac{T}{\alpha} \quad . \tag{4.23}$$

Regarding the damping and the friction of the system, different tests by free oscillations can be carried out. The following example discusses the discrete robotic mechanism. Similar experiments can be conducted with the continuum robotic setup, but one has to consider the extra

effort for calculation of the angles of the segments and the fact that three PAMs result in an asymmetric arrangement. Further, the third DOF of each segment must be observed, which makes additional tests with free oscillations in longitudinal direction necessary.

In the discrete case, the robotic setup is modified, such that the damping parameters of one PAM pair are extractable. To do so, the robot comprising three segments is mounted upside down and all PAM pairs – except the one that is to be measured – are replaced by stiff turnbuckles. Only one DOF is moveable. Different kinds of experimental scenarios are tested: (I) swinging out with varying deflections: min. 4.1°, med. 8.4°, max. 10.8°; (II) swinging out with varying pressure; (III) swinging out with additional load; (IV) swinging out without PAMs: determination of mechanical friction only.

The discrete robotic setup allows easy determination of joint angle data φ, by means of which a damping parameter d can be derived. This procedure comprises four steps (1)-(4).

(1) Oscillation tests are performed and the angle data of the moving joint are logged. With these data the logarithmic decrement Λ can be determined:

$$\Lambda = \frac{1}{n} \ln \left(\frac{\varphi(t_k)}{\varphi(t_k + nT)} \right) \quad . \tag{4.24}$$

The angle values φ are taken into account at a specific time t_k, and n is the number of full waves with the periodic time T.

(2) The general formula for damping calculation is used as a basis for further parameter determination [29], including Lehr's damping ratio D, mass moment of inertia Θ and torsional stiffness c_T:

$$d = 2D\sqrt{\Theta c_T} \quad . \tag{4.25}$$

Θ comes from CAD data, c_T is gained by calibration procedure (cf. section 5.2).

(3) For getting the unknown damping ratio D, another correlation between the logarithmic decrement Λ and Lehr's damping D is deployed:

$$D = \frac{\Lambda}{\sqrt{4\pi^2 + \Lambda^2}} \quad . \tag{4.26}$$

(4) Putting Equations 4.24 - 4.26 together, this yields an expression which makes it possible to calculate the damping parameter d directly from the oscillation tests and the set of logged angles φ:

$$d = \frac{2\Lambda\sqrt{\Theta c_T}}{\sqrt{4\pi^2 + \Lambda^2}} \quad . \tag{4.27}$$

The results from the tests by free oscillations with the discrete setup can be summarized in an approximation as given in Figure 4.11. This illustration shows the dependencies between damping parameter d and current pressure p. The variation of the damping parameter ranges within 72-83N m s and can be estimated linearly decreasing with increasing pressure. The effect of damping decrease at higher pressure has two reasons: (1) the air inside the PAM changes its density and damping behavior, and (2) the membrane of the PAM deforms and changes its material flexibility. Besides pressure dependency, there is also velocity or deflection dependency that can be determined within the experiments, but these dependencies are negligibly small compared to the ones due to the pressure. In addition, the velocities and deflections of the

segments are limited to ranges that do not affect this dynamic influence of the damping. Damping values at 0 bar, indicated as purple bullets in Figure 4.11, correlate with the joint friction superimposed by internal PAM friction.

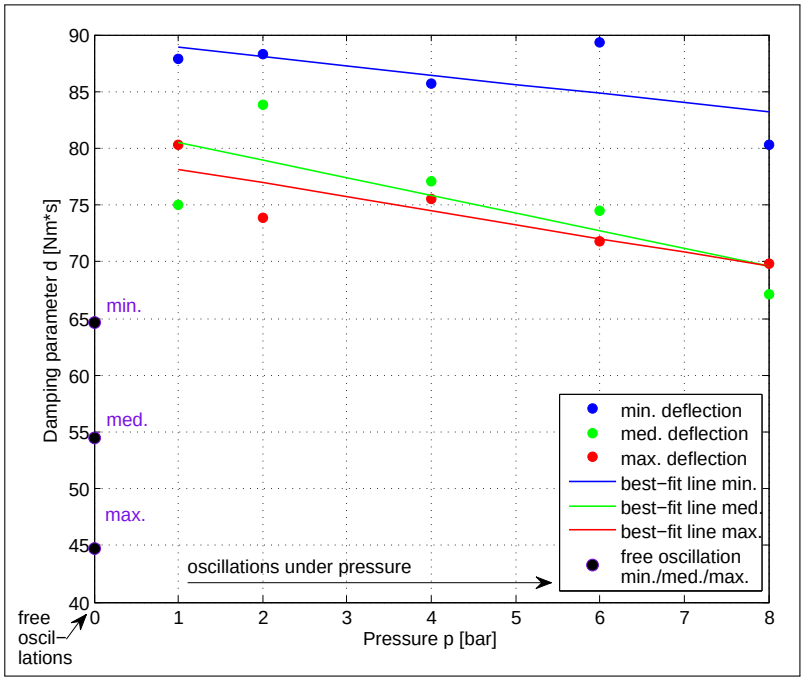

Figure 4.11: Joint damping [34]

4.5 Motion and dynamics simulations

To analyze the dynamics of both the discrete and the continuum worm-like robotic mechanisms, simulation environments are implemented utilizing Matlab engineering tool.

Figure 4.12 depicts the simulation of the discrete mechanism with three segments. The model integrates the graphical representation of the links (red lines) and the cardan joints (green bullets). Basis of the modeling of the physical system is an implementation of the Newton-Euler equations as given in 4.21 and 4.22. In this regard, reachable positions, velocities and accelerations, which cause corresponding forces and torques, can be identified. The parametrization is mainly focused on geometric inputs, such as link lengths as well as mass or inertia values for relevant moving parts of the system. Both friction and damping values are considered (cf. Figure 4.11). To run a simulation, it is only necessary to set reasonable initial values for the kinematic configuration of the robot, i.e. positions or angles of the segments plus their velocities.

All reachable forces and torques depend on the physical embodiment of the actuators used. Figure 4.13 shows the correlations between the nonlinear forces with respect to muscle contraction. DMSP type PAMs are available with an inner diameter range from 5 mm to 40 mm. The maximum pulling force for a DMSP-40 type is more than 5 kN at 6 bar air pressure.

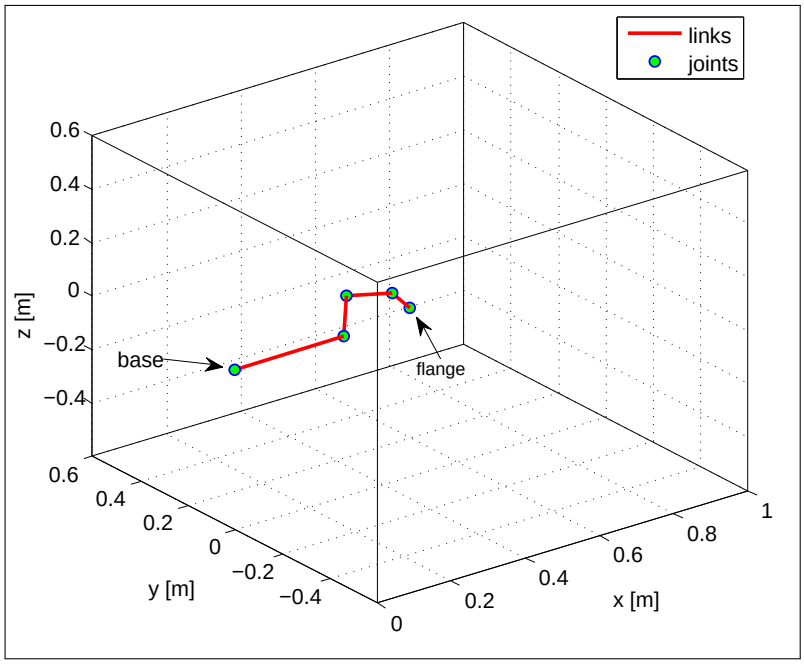

Figure 4.12: Simulation – discrete case, 5 s, $\theta_i = \pi/8$, cf. [138]

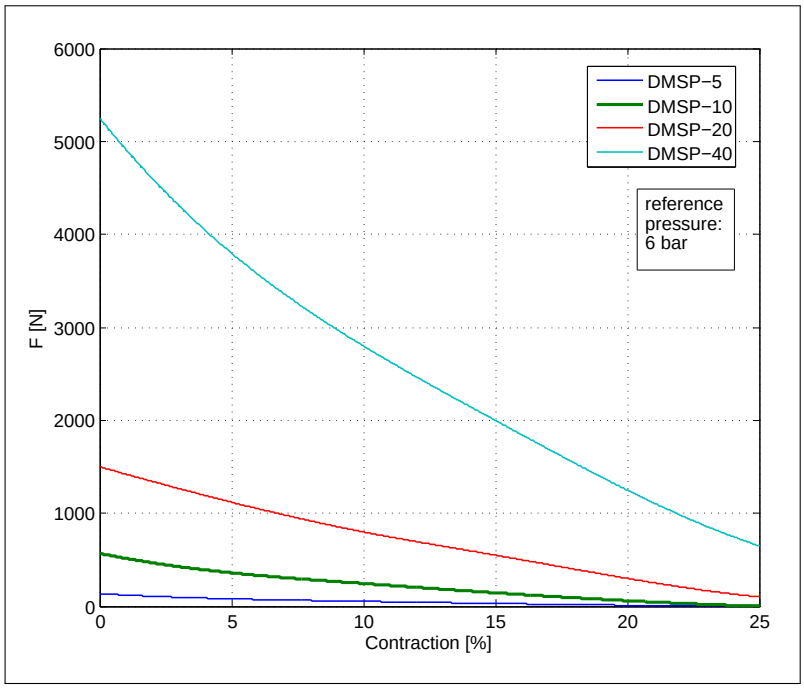

Figure 4.13: PAM forces

Detailed considerations of concrete values for the dynamics of the discrete robotic setup are given later on in subsections 6.1.1, 6.1.2 and 6.1.4.

In a similar way, the continuum worm-like robotic mechanism is discussed within subsections 6.2.1, 6.2.2 and 6.2.4. As the continuum system differs in appearance, also the simulation is different for this kind of robot. Instead of using straight lines and bullets, the visualization is founded on the torus segment model that was introduced in Figure 4.2, which includes bending abilities of the links. Figure 4.14 depicts such a visualization with an example of four segments (depicted alternating in violet and green) [131]. It is based on an adapted version of the open software library from CoR-Lab (Research Institute for Cognition and Robotics at the University of Bielefeld).[3] This simulation allows to estimate the motions of the system and also indicates the goal babbling inverse kinematics test positions – target points, test points and reached points. The Cor-Lab library serves as a basis for an enhanced simulation built in Matlab, which further considers dynamics, i.e. forces and torques.

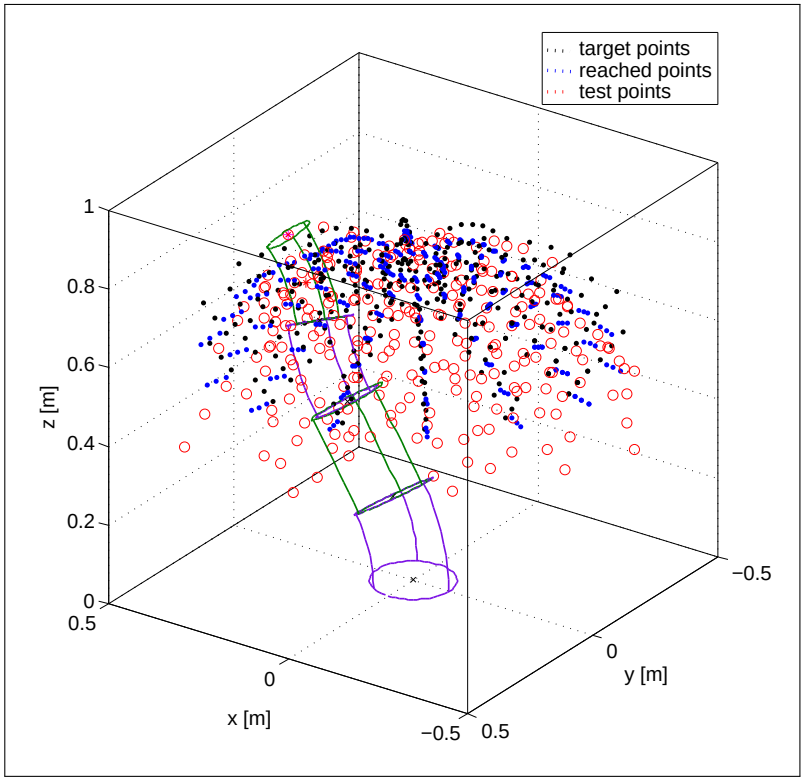

Figure 4.14: Continuum case simulation based on Cor-Lab open software library [131]

In this context, it is noteworthy to mention that there are already software packages available to simulate continuum style robotic structures in real-time [30]. Also there are dynamic models for similar robots, e.g. the Bionic Handling Assistant, which use fine-grained parametrization [38]. Moreover, there are path planning approaches for compliant pneumatic robots, e.g. based on neural networks [161]. However, such extremely detailed considerations are not part of this thesis.

[3] cf. url: http://www.cor-lab.org/software-continuum-kinematics-simulation, last accessed August 12, 2013; cf. [131] for further information

Chapter 5

Control implementation

Two kinds of prototypes were described in Chapter 3 and corresponding kinematic or dynamic discussions were given in Chapter 4. The next chapter deals with details about the implementation of the control of the worm-like robotic mechanisms. It must be considered that the implementation has to be designed as elementary as possible to get along with very simple and cost-effective embedded onboard hardware. Thus, control approaches or sensor signal filtering methods with high computational effort shall be avoided. Initially, the control strategy is presented in section 5.1, which is followed by the muscle calibration in 5.2 and the pressure control within 5.3. For the discrete case, angle control loop specifics are explained in section 5.4, stretch sensor control for the continuum style variant is revealed in 5.5. The chapter closes with considerations concerning the control hardware architecture in section 5.6.

5.1 Control strategy

Finding the adequate control strategy for a compliant robotic system is accompanied by a trade-off between reasonable control effort, control quality and expenses for hardware components. The system behavior of the prototypes is nonlinear, so the question rises how these characteristics can be modeled and simplified to guarantee control loops that can be computed on cost-efficient hardware solutions. Model-based control that includes all parameters of these complex pneumatic systems, such as detailed considerations of temperature influence or internal muscle damping effects, goes beyond the scope of justifiable control effort.

One of the main contributions to this nonlinearity comes from the compressible fluid. This fact also supports the idea of using air feed tubes between the valves and the actuators that are as short as possible, such that the nonlinear effects of the compressibility of the air can be kept within limits. As a matter of principle, the suggested decentral hardware architecture allows to utilize even extremely short feed pipes. However, the flow of the fluid within the control valves also causes challenges [20, 65]. Regarding damping and air flow aspects, section 4.4 of the previous chapter already introduced relevant estimations that can be used in the following control approach.

Second most important influence is caused by the PAM actuators. These actuators can be modeled as pneumatic cylinders with variable diameter with respect to contraction, moving against

a spring that has a contraction-dependent tension [65]. It is worth mentioning that the nonlinear behavior of the PAM within an antagonistic-controlled compliance environment is a prerequisite in order to control the compliance, i.e. to influence the stiffness parameters [125]. Details about the PAM characterization are given in section 5.2. In this manner, the control strategy utilizes a basic PID force control. Key feature here is a precisely calibrated nonlinear PAM that enhances the control quality substantially. When these nonlinear characteristics are integrated sufficiently, the control precision increases. Also it is a concern that too complex algorithms should be avoided, else there would be computation bottlenecks if the system was built with simple hardware. Additionally, specific attention is given to a completely modular approach of the entire system, which should be reflected in a modular and decentralized control architecture (cf. section 5.6). This modularity is coupled with both an extensibility of the setup, which means the number of segments of the robot, and a scalability of each of these segments. Thus, the architecture needs to have a high degree of flexibility.

5.2 Muscle calibration

As introduced in section 5.1, precise calibration of the PAMs is necessary to result in high control accuracy. There are some specification data of the PAMs available from the manufacturer, such as working range diagrams [40]. Also calculations based on the Festo MuscleSIM software tool[1] can be used. However, experiments have shown that each PAM should be regarded separately, since there are individual differences in PAM properties, which cause control precision problems.

In particular, there are divergences with respect to material parameters, e.g. effected by material aging, and geometry influence due to inevitable manufacturing deviations. It is crucial to ensure a precise calibration and to generate usable PAM characteristics [14, 83]. Three different parameters have to be taken into account: (1) muscle pressure, (2) muscle force and (3) muscle length.

(1) The muscle pressure can be determined using a pressure gauge that is mounted close to the PAM (cf. subsection 3.6.3). This sensor returns numeric pressure values that can be correlated to a physical unit, such as pascal or bar.

(2) Muscle forces can be calibrated by applying defined external forces. These external forces can either be additional loads, which are attached to the robot, or the weight force of the robot itself. It is necessary to know about the kinematic configuration of the system, i.e. the balance of forces and torques with respect to their lever arm etc., which satisfies static equilibrium. In particular, for calibration of more than one segment of the system it is beneficial to use the weight of the following segments to calibrate previous segments. Only for the last segment an additional weight is relevant. With this method the calibration can be eased, for there is no necessity to disassemble single segments once they are attached together.

(3) The determination of the muscle length is two-fold: (I) for the discrete robotic setup making use of cardan joints between the segments, rotary angle encoders attached to the joints' axes are read out, so the actual muscle length does not have to be computed (the shortening of the muscles as the cause of joint motion is implied anyway); (II) for the continuum robotic setup based on flexible PAMs, stretch sensors are fixed to the muscles to detect their length. Both

[1] Festo MuscleSIM Version 2.0.1.5 (2005)

rotary encoder and stretch sensor data are used to calculate the kinematics and the dynamics in a second step. For simplification reasons, the PAM characteristics are generated with respect to a quasi-static state. Dynamic effects are considered separately, as previously mentioned in section 4.4.

Due to the fact that the volume of the characteristics data-sets obtained by the calibration procedure is quite high, another post-processing step is carried out to reduce this data volume. For each PAM, low complex but accurate functions are processed that can be also computed by low-cost microchips. An evolutionary symbolic regression approach is used, which is based on software tool Eureqa by Cornell Creative Machines Lab[2]. This program intends to find the simplest mathematical formulas to describe the measurement data, i.e. it tries to extract hidden mathematical correlations out of the data provided. Within this entire symbolic regression approach several sub-steps are necessary, as depicted in Figure 5.1.

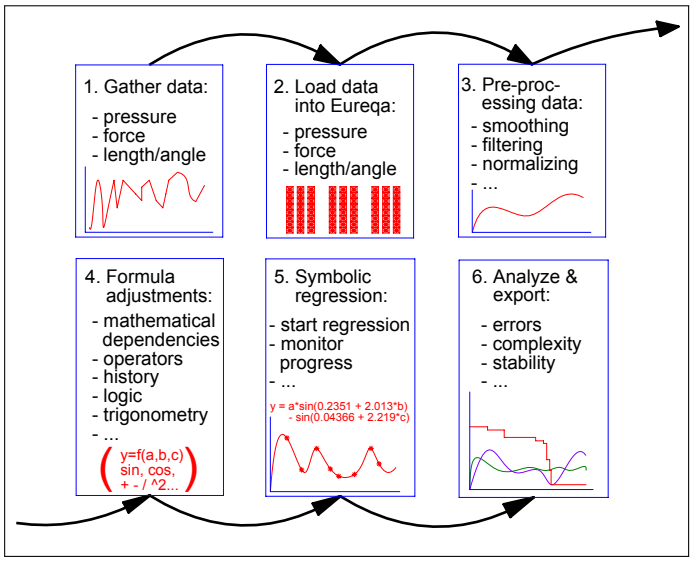

Figure 5.1: Symbolic regression process

In a first sub-step, characteristics data have to be gathered, i.e. muscle pressure, force and angle (discrete case) or length (continuum case). Various forces are applied, using either external loads or loads caused by subsequent robot segments. The calibration device, which is optionally equipped with additional weights, is depicted in Figure 5.2.

For each measurement, different pressure is used, the resulting angle or length is measured, and actually applied force is calculated and stored in a common file. As the muscles are antagonistically arranged within the discrete robot, calibration expenses in this case can be also reduced by considering these two PAMs as a matched pair that generates one DOF. Overall, a set of 200 measurement data points are gathered. Initially, a pressure is set and the angular encoder position value is detected (discrete case) or the length of the muscle considering the stretch sensor is saved (continuum case). Then, the respective muscle force is computed as mentioned previously.

In a second stage, these data are loaded into Eureqa. A third sub-step deals with pre-processing of the data, which means filtering, normalizing, smoothing, removing of outlying data or handling

[2]see creativemachines.cornell.edu/eureqa

Figure 5.2: Muscle calibration device

of missing data. Subsequently, the fourth step includes various adjustments for the generation of formulas. Different basic or logic operators can be chosen, the use of history or trigonometry can be arranged. The most important adjustment is feasible using mathematical dependencies, which means that equations can be given that have to be satisfied by the output correlations. These dependencies have to be figured out separately. An identification of these equations is based on a PAM model that was introduced by Hildebrandt [65]. The muscle is considered as a one-way cylinder that moves against a spring with contraction-dependent tension. Also the cross section of the cylinder piston is variable, which is again related to the contraction of the PAM. This leads to a correlation as follows, in which p represents the pressure, f means the muscle force and l is the current length or joint angle:[3]

$$p(f,l) = f_1(l)f + f_2(l) \quad . \tag{5.1}$$

Within sub-step number five the regression computation is started. While running, it can be monitored. Finally, a last sub-step allows to analyze and export the formulas provided, such that they factor in certain quality indicators, e.g. complexity, stability and range of errors.

As an example, results for the low-cost formulas that are fitted for each of the four muscles of one discrete segment ($01-04_{discrete}$) are shown (cf. [34]):

$$p_{01,discrete}(\alpha,f,c) = \frac{80.17c - 70.12f}{184.59 - 64.99\alpha + 910.72\alpha^2} + 0.04 - 0.67\alpha + 3.28\alpha^2 \quad , \tag{5.2}$$

$$p_{02,discrete}(\alpha,f,c) = \frac{319.80c + 190.75f}{542.20 - 113.74\alpha + 2738.90\alpha^2} - 0.08 + 0.13\alpha + 3.32\alpha^2 \quad , \tag{5.3}$$

$$p_{03,discrete}(\alpha,f,c) = \frac{43.19c - 37.40f}{90.00 + 24.56\alpha + 25.53\alpha^2} + 0.01 - 0.42\alpha + 0.37\alpha^2 \quad , \tag{5.4}$$

$$p_{04,discrete}(\alpha,f,c) = \frac{56.84c - 39.54f}{104.86 - 57.54\alpha + 1022.21\alpha^2} - 0.04 - 0.02\alpha + 6.30\alpha^2 \quad . \tag{5.5}$$

The pressure p_i of the PAM depends on the joint angle α, the muscle force f and the stiffness value c. By stiffness c the compliance of the joint can be set up. PAM characteristics functions

[3] muscle length and joint angle are kinematically correlated

for all other PAMs – either in the discrete or the continuum case – have comparable functions with adapted values for the constants.

An example of PAM characteristics of the discrete robot case, determined by means of the previously described regression approach, is shown in Figure 5.3. The characteristics are reduced as line plots for one PAM. Forces are denoted in Newton, angles in degrees, and the pressure is shown in bar.

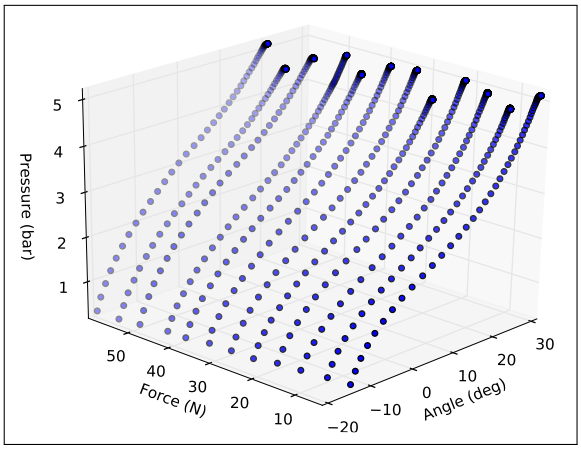

Figure 5.3: Muscle characteristics – reduced line plot [32, 81]

Triangular surface plots for muscles one to six, generated out of these characteristics data using Matlab, are depicted in Figure 5.4. Muscle characteristics representations seven to twelve are outsourced to the appendix within Figure A.1. Both figures show the example of the discrete robot case. The basis for these plots are three different PAM types that were used in a first stage of development, namely DMSP-10-160N-RM-CM, DMSP-5-130N-RM-CM and DMSP-5-50N-RM-CM. From the plots it is visible that the DMSP-5 PAM types can carry much less loads (maximum 135 N), which results in less contraction and therefore limited joint angles. Accordingly, in a second stage of development of the worm-like robot only DMSP-10 PAM types are integrated, which can bear up to 630 N. Nevertheless, one can see that each of the PAMs behaves differently, which means that a calibration of all the muscles can enhance control quality.

In the continuum style robot case, resulting characteristics have very similar structure, except that length information derived by the stretch sensors has to be converted to a usable information about the kinematic state of a segment.

5.3 Pressure control

As stated in section 3.1, a preliminary stage of development used rather simple binary on-off valves by FAS, type Chipsol, which were replaced by proportional valves by Parker, type MDPRO. For one pair of these proportional valves a separate pressure controller is utilized. Such a decentralization is due to modularity and also for space reasons.

An interior control loop has to deal with the pressure control, which is the central stage within a cascaded control strategy (cf. sections 5.4 and 5.5). It comprises a pressure controller board

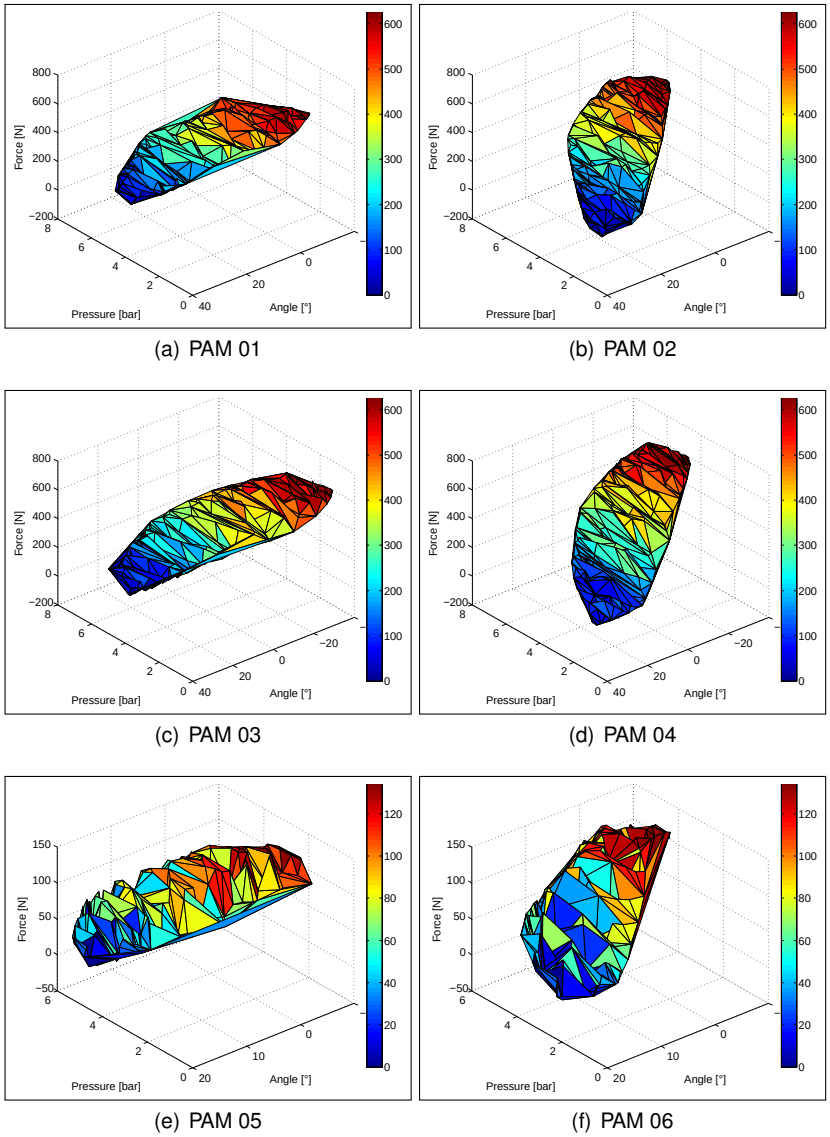

(a) PAM 01 (b) PAM 02

(c) PAM 03 (d) PAM 04

(e) PAM 05 (f) PAM 06

Figure 5.4: Muscle characteristics (I)

that allows to transform analog sensor signals coming from the pressure sensor (0-5V), which again have to be prepared by an ADC, being integrated inside an ATTiny microcontroller. Depending on the desired pressure that has to be set, the microcontroller converts pressure signals and links them to the subordinate current controllers, one for inlet and one for outlet. This way, the current controllers represent the innermost control stage of the cascaded control. The output of the microcontroller or the input for the current controllers are PDM (pulse density modulation) signals. In contrast to PWM (pulse width modulation) the PDM doesn't have a pre-defined frequency, but the relative density of the pulses is considered, which has advantages in terms of usage with slower microcontrollers, such as the ATTiny.

The actual control is realized as a standard PID controller (cf. Figure 5.5), characterized by controller output $u(t)$, error e, which is the delta between actual and desired pressure, proportional gain K_p, integral gain K_i, derivative gain K_d, instantaneous time t and integration variable τ.

Equation 5.6 shows the non-interactive PID form:

$$u(t_k) = K_p e(t) + K_i \int_0^t e(\tau) d\tau + K_d \frac{d}{dt} e(t) \quad . \tag{5.6}$$

It is implemented in a discretized form on the microcontollers with the controller output $u(t_k)$, control gain K_p, integral time T_i and derivative time T_d, which can be written as follows:

$$u(t_k) = u(t_{k-1}) + K_p \left[\left(1 + \frac{\Delta t}{T_i} + \frac{T_d}{\Delta t} \right) e(t_k) + \left(-1 - \frac{2T_d}{\Delta t} \right) e(t_{k-1}) + \frac{T_d}{\Delta t} e(t_{k-2}) \right] \quad . \tag{5.7}$$

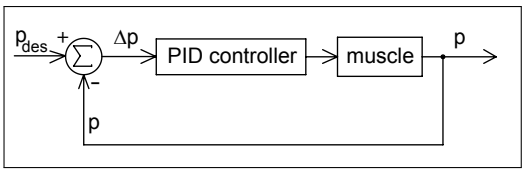

Figure 5.5: PID pressure controller

All controller parameters are obtained from experiments and tuned manually. First, the proportional term P is adjusted, setting integral as well as derivative term zero, thereby detecting the critical gain. Once this is done, the derivative term D is added, considering the natural oscillation frequency behavior. As a next step, the integral term I is set, basically in a range of about 10 % compared to the gain value of the derivative term. The entire process needs several tuning loops until a reasonable control precision is guaranteed. In particular, the D term is very sensitive, i.e. the main cause for instabilities and overshooting. As the operating frequency of the muscles is very limited[4], for practical use high frequencies are not relevant and the aforementioned issue is not significant. Therefore, a detailed stability analysis is not within the scope of this thesis.

For the discrete robot setup it has to be taken into account that each muscle can only contract, i.e. pre-stressing is needed to allow PAM movements in both directions about a cardan joint axis. In this case, half of the shortening length of the muscle, 12.5 % of the PAM length, has to be reserved for expanding or shortening of the antagonistic PAMs. Only then contraction and extension is possible with the same value for both muscles of the antagonistic PAM pair.

An overview about the customized pressure controller board is shown in Figure 5.6. The correlation between the pressure controller and the superordinate angle controller (cf. section 5.4) is concerned in section 5.6. For specifics regarding the electronic setup, the reader should refer to subsection 3.5.2.

5.4 Angle control – discrete case

Based on the pressure controller that was explained in the previous section 5.3, the second step of a cascaded control strategy is taken – the outer angle control loop for the discrete case. An overview of this angle control loop for one segment is given in Figure 5.7. This outer loop

[4] the max. operating frequency mainly depends on the muscle contraction; theoretically values between 3 Hz and 150 Hz can be reached [41]; in the setup presented here values with up to about 10 Hz are dominant

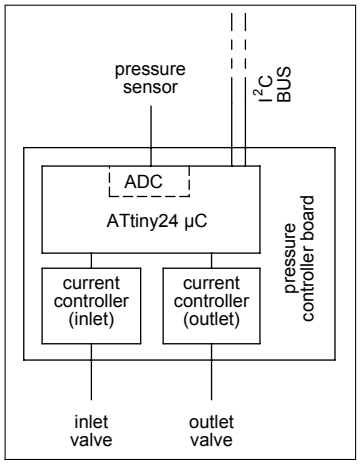

Figure 5.6: Implementation of pressure controller [32]

allows to control the positions of the discrete worm-like robot, which is rotatable about all of its cardan joints. Accordingly, each of the joint angles has to be controlled to reach a certain position or to move along a given trajectory. This is done utilizing position data received from the rotary encoders, which are fixed to the cardan joint axes. Two encoders are installed on one cardan joint, which has two perpendicular axes. Reading the sensor data of these two encoders, which are related to the same cardan joint, allows to control the position of one segment of the discrete robot. Each encoder measures one cardan joint axis, which means that one encoder output ensures to perform a subordinate pressure control loop with one PAM pair.

Once the angle values are set for the two antagonistic PAM pairs, a position control loop can be started, integrating pressure control loops for all of the four PAMs. Pressure sensor data are used to perform the subordinate pressure control loop, which basically drives the PAM. Encoder sensor data allow to generate a position control loop, in which the angles of each joint are adjusted, such that an overall desired kinematic configuration can be reached. This desired configuration has to be defined separately, e.g. within an external control PC. Such an external control PC comprises a setpoint generating unit or, as the case may be, even a trajectory generating unit in order to output joint angle commands to drive the system. These input commands for the angular control loop are sent to a PID force controller based on angle deviations, and one PID controller takes care of one DOF – or in other words – one pair of pneumatic muscles. Also these input commands or the set of desired joint angles are sent to two more control loop components, a muscle force solving stage and a muscle characteristics stage. Muscle forces are always related to torques, since all the PAMs are connected to the joints using supporting discs or lever arms. The force solving stage is necessary to calculate the equilibrium of forces that affect to each cardan joint axis, i.e. the antagonistic forces of both PAMs for one DOF have to follow an equilibrium condition. Additionally to the muscle forces also stiffness forces or external forces can be added on the force solving stage. Stiffness forces in this sense are forces that influence the stiffness behavior of the muscles, which means that the PAMs can be adjusted harder or softer. For this purpose, the PAM pair of one DOF is fed with the same stiffness force value, but with different signs for both feedings.

External forces can be additional loads, friction or forces due to damping as introduced in section 4.4. The PID controller output is harmonized with the stiffness and external forces, and in this way the muscle force solver is fed adequately. The calculated forces coming from the

solver are forwarded to the characteristics stage, which also receives the desired angles as input. Within the characteristics stage the correlations between muscle force, muscle pressure and its length or the resulting joint angle are used. In this manner, for each muscle an output pressure is extracted, based on the desired angle and force, which serves as the input. Exactly the relations from section 5.2 are exploited. To close the angle control loop, the actual angle sensor data of each joint axis are returned to the input side of the PID controller, which are subtracted from the desired angular values to get the angle error. The integration of sensor inputs, force PID computation, muscle force solving as well as processing characteristics all run on Arduino Nano boards (cf. subsection 3.5.1), one board for each segment. Calculations for pressure adjustment and valve currents are performed on customized pressure controller boards (cf. subsection 3.5.2).

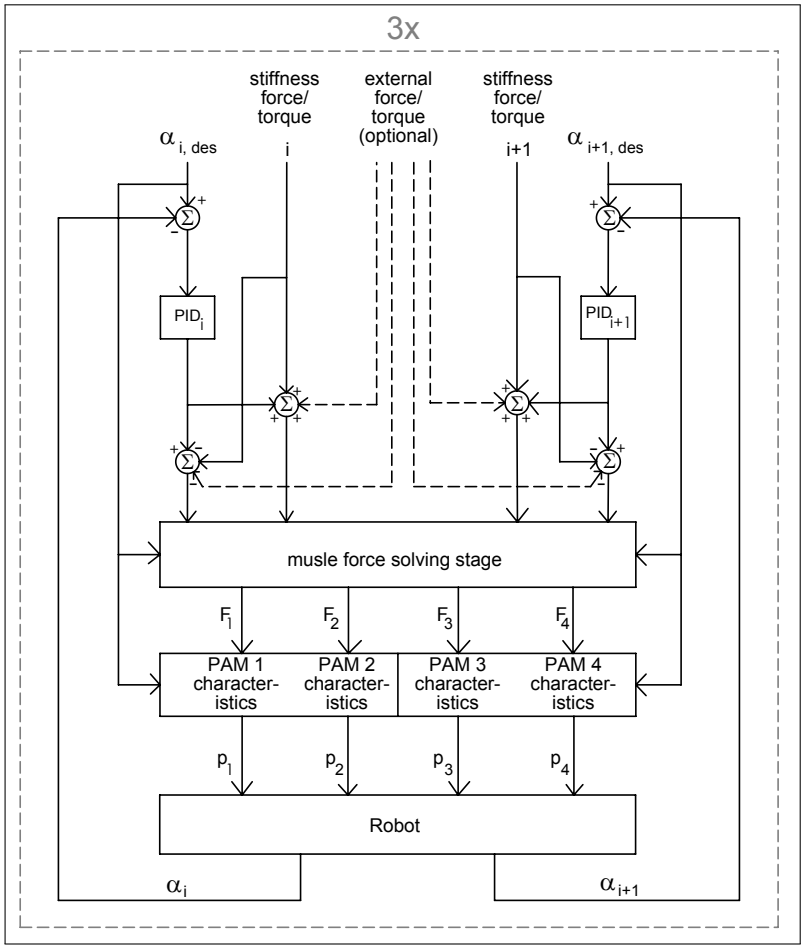

Figure 5.7: Angle control (cf. [32])

To emphasize the correlation of the set of six robotic joints including all the PAMs, Figure 5.8 depicts the angle control in a wider range. This cascaded control scheme (cf. [34]) has an innermost current controller loop, which is used to set the current to open the proportional valves. Each of the pairs of the eight valves within one segment (four valves for inlet, four for outlet) – or the 24 valves of the entire worm-like robot with three segments – has one assigned current controller (CC). According to the microcontroller output voltage, a proportional valve current is adjusted, which is done by hardware components (cf. subsection 3.5.2). As already

treated in section 5.3, superior to this current controller loop there is a pressure loop utilizing pressure controller boards (PC), which care about all of the 12 PAMs. The outermost position loop is basically the angle control stage that was introduced above. A control unit, such as an external PC, serves to input setpoints or trajectory commands, but also offers the option for including a GUI to simplify the control handling.

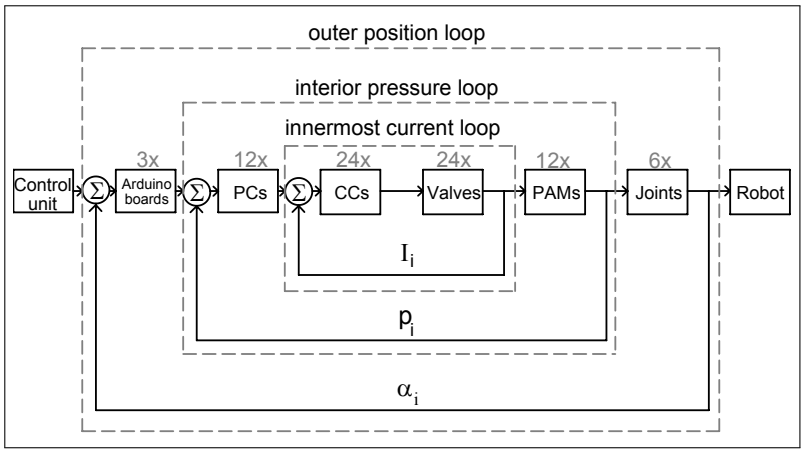

Figure 5.8: Cascaded control – discrete case [34]

5.5 Stretch sensor control – continuum case

Similar to the previous section 5.4, a position control for the continuum robot case depends on the evaluation of adequate position sensor data. Figure 5.9 highlights the position control strategy that integrates the stretch sensor control in a segment-based context, similar to what was shown in Figure 5.8 of section 5.4. In the future, stretch sensor signals are merged with 6D gyroscope and acceleration sensor data to close the position feedback loop. However, the stretch sensors are currently the main instruments to gain feedback for position control (length information of the PAMs l_i), which is only enhanced by additional 6D sensors (yaw rates $\dot{\alpha}_i$ and accelerations $\ddot{x}_i$). These 6D sensors are interfaced to Teensy 3.1 main controller boards, which deal with the elaborate processing of the sensor data. In the current stage of development, these 6D sensors are used to evaluate the stretch sensor data and for tracking reasons. All stretch sensors are connected to their corresponding pressure controller boards. The integration of Teensy boards instead of Arduino boards (as used in the discrete case) is motivated by increased control effort of the flexible continuum mechanism that integrates computationally expensive sensors (cf. subsections 3.5.1 and 3.6.6).

As introduced in subsection 3.6.5, the stretch sensors suffer from a major drawback, namely hysteresis. It can be determined that the sensor output is characterized by a peak once it is released, followed by a slow decay behavior. The time that is necessary to relax the sensor, such that its original resistance condition is reached, takes several minutes (cf. Figure 3.25). If one considers several elongations after one another, the sensor resistance increases in a zigzag manner (cf. Figure 5.10). Additionally, these resistance values R gathered from the stretch sensors have to be mapped to muscle length values l, which are necessary for the

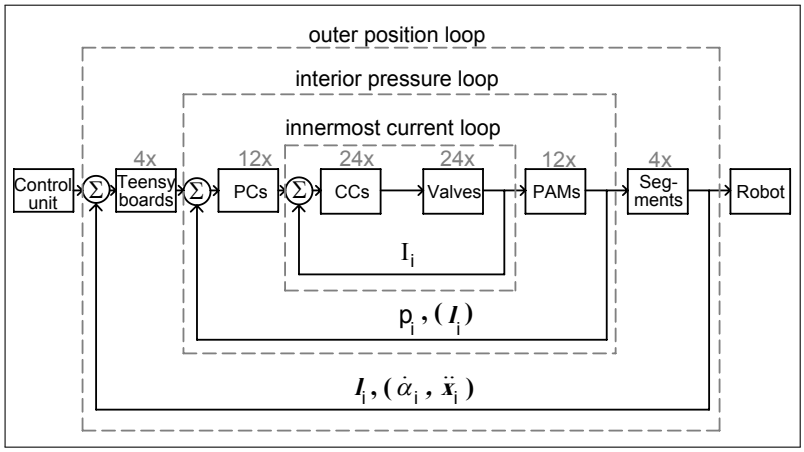

Figure 5.9: Cascaded control – continuum case [33]

actual stretch sensor control in the next step:

$$l = l_{relaxed} \cdot (1 - \frac{R - R_{min}}{R_{max}}) \quad . \tag{5.8}$$

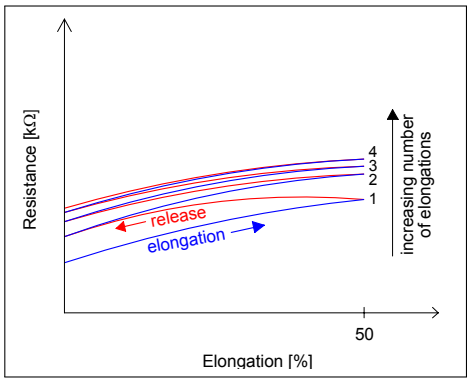

Figure 5.10: Hysteresis behavior of stretch sensor

Nevertheless, to realize a control using these stretch sensors, a compensation of this hysteresis or relaxation is necessary. In [155] an advanced compensation method based on Preisach model [126] is presented, which separates static hysteresis from relaxation. For this reason, a dynamic hysteresis operator is added to also deal with the fact that the output values of the sensor gradually decrease at constant elongation. However, this approach leads to a sensor evaluation quality that still has an error between 5.9 % and 10.4 %. That's why a different approach is applied, which is based on sliding mode control [33, 66, 144, 145, 146, 149, 153, 160]. Sliding mode control is a robust method for complex nonlinear systems. It can deal with input parameter changes and noise. A complex system is decoupled to result in separate subsystems, which are easier to handle [134]. More concretely, all PAMs are treated with separate sliding mode controllers, which take care of the stretch sensor feedback. The relevant relation between the PAM length l, the muscle pressure parameter p and the valve current i is interpreted with the system equation below:

$$\dot{l} = f(p, i) \quad . \tag{5.9}$$

According to the sliding mode theory the system has to slide along a sliding surface, which is correlated to the PAM length or the actual and desired stretch sensor length l and l_{des}. The surface can be determined by the following term:

$$s(l) = l - l_{des} \quad . \tag{5.10}$$

It has to be guaranteed that there is only sliding possible on the surface, i.e. $\dot{s}(l) \stackrel{!}{=} 0$. Therefore, the differential sliding mode condition yields:

$$\dot{s}(l) = \frac{\partial s}{\partial l}\frac{\partial l}{\partial t} = f(p,i) \stackrel{!}{=} 0 \quad . \tag{5.11}$$

Basically the task is to identify the objective function for the valve current, which can be written as:

$$i = g(p,\dot{l})|_{\dot{l}\stackrel{!}{=}0} \quad . \tag{5.12}$$

In other words, valve currents have to be found, which don't affect PAM movements. Three steps are necessary for the final implementation of the sliding mode approach. First, the maximum valve values are registered for an arbitrary start length of the artificial muscle. Second, the gathered valve currents are fitted by means of a linear function:

$$i_{min} = g(p) \quad . \tag{5.13}$$

In a final third step, the correlation above is brought together with a P-controller with a weighting term K_p for error tuning:

$$i = i_{min} + K_p(l - l_{des}) \quad . \tag{5.14}$$

5.6 Decentralized modular architecture

The control and the hardware architecture of the worm-like robotic mechanism, equal for both discrete and continuum style prototypes, are based on a decentralization and modularity approach (cf. [32]). This approach specifies that the entire robot is composed out of single segments, which can be easily connected with respect to mechanical, electrical and control interfaces. This enables extensibility, i.e. a robot can be generated with a variable number of segments without the need to make large-scale changes. The power electronics and control hardware boards are distributed all over the robot, which means that each segment has its own main controller board and one pressure controller board per PAM is used as a power electronics stage for switching the valves. In contrast to the hardware itself, the power and data wiring is centralized, which means that a set of wires is arranged through the entire robot, leading from one board to the next one, such that a serial cabling structure is the outcome. Each cable connection is realized by plug-in connections to guarantee fast assembly or extension. Similarly, the air pressure feed line, which is not focused on in this regard, is centralized as well, i.e. a single feed tube goes through the robot that locally supplies the PAMs or valves by stub lines.

The aforementioned main controllers for each segment are based on Arduino Nano 3.0 boards in the discrete case and Teensy 3.1 boards in the continuum case (cf. subsection 3.5.1). A

power supply is realized using a microcontroller adapter shuttle board, which is connected to a 5 V feed wire. In the discrete robot case this 5 V supply is additionally used to feed the two rotary encoders that belong to the corresponding main controller. Hence, the main controller adapter boards are used to interface the position feedback sensors. In the continuum style case instead of encoders, 6D sensors are connected to the Teensy main controllers. The segments of the continuum prototype are equipped with three stretch sensors each, which are coupled with the pressure controller boards.

The Arduino or Teensy boards of several segments are arranged in an i^2C bus network. i^2C is a bus that only needs two wires, one clock line SCL and one data line SDA. Due to that the wiring of the robot can be reduced. Also there are a lot of different economical and small-size microcontrollers available that support this bus, such as the Atmel or Arm based chips. These microcontrollers all offer on-chip interfaces for i^2C, which make this bus a very suitable and cheap solution.

In the early 1980s, the i^2C bus was introduced and patented by Philips to communicate between single components [109]. Since then it has become a de facto industry standard [16], which is specified in an official document available from NXP Semiconductors[5]. This master-slave oriented bus can address up to 128 bus participants, which would equal up to 128 segments. Also multi-master support is given for the i^2C bus. All subordinate pressure controllers ("PC", four controllers per segment in the discrete case, three controllers for the continuum style case) are also connected using an i^2C bus, but this bus is handled separately from the main controller network in a multi-master design. Each of these pressure controllers integrate one pressure sensor, which is driven at 12 V, and two current controllers to switch the inlet and outlet valve for one PAM, which is done at 9 V. To allow a flexible and modular integration of the boards, the Arduino Nano and Teensy microcontrollers are shuttled on adapter boards, which offer connectors for all subordinate pressure controllers, feedback sensors and i^2C bus link. Basically each of the main controller boards (Arduino or Teensy) offers USB interface, which can be either used to flash the boards or to send superordinate control commands. In this way, overall motion commands can be sent to one of the main controller boards, which then becomes the master board. Accordingly, the main controller chips offer i^2C to USB bridges, which allow to communicate with a superordinate exterior control unit, e.g. a conventional PC.

In Figure 5.11 all of the aforementioned correlations are shown in a schematic, describing the entire setup of the decentralized modular control hardware architecture. It must be distinguished between the discrete and the continuum robotic prototype. The presented discrete worm-like robot is based on three segments, comprising four PAMs and four pressure controller stages each. In contrast, the continuum style robot has four segments with three PAMs and three pressure stages each. This fact has been taken into account within Figure 5.11. Corresponding boxes with respect to the continuum or discrete worm-like robotic mechanism are highlighted with dashed black lines.

[5] i^2C bus specification and user manual, see http://www.nxp.com/documents/user_manual/UM10204.pdf, last accessed October 15, 2013

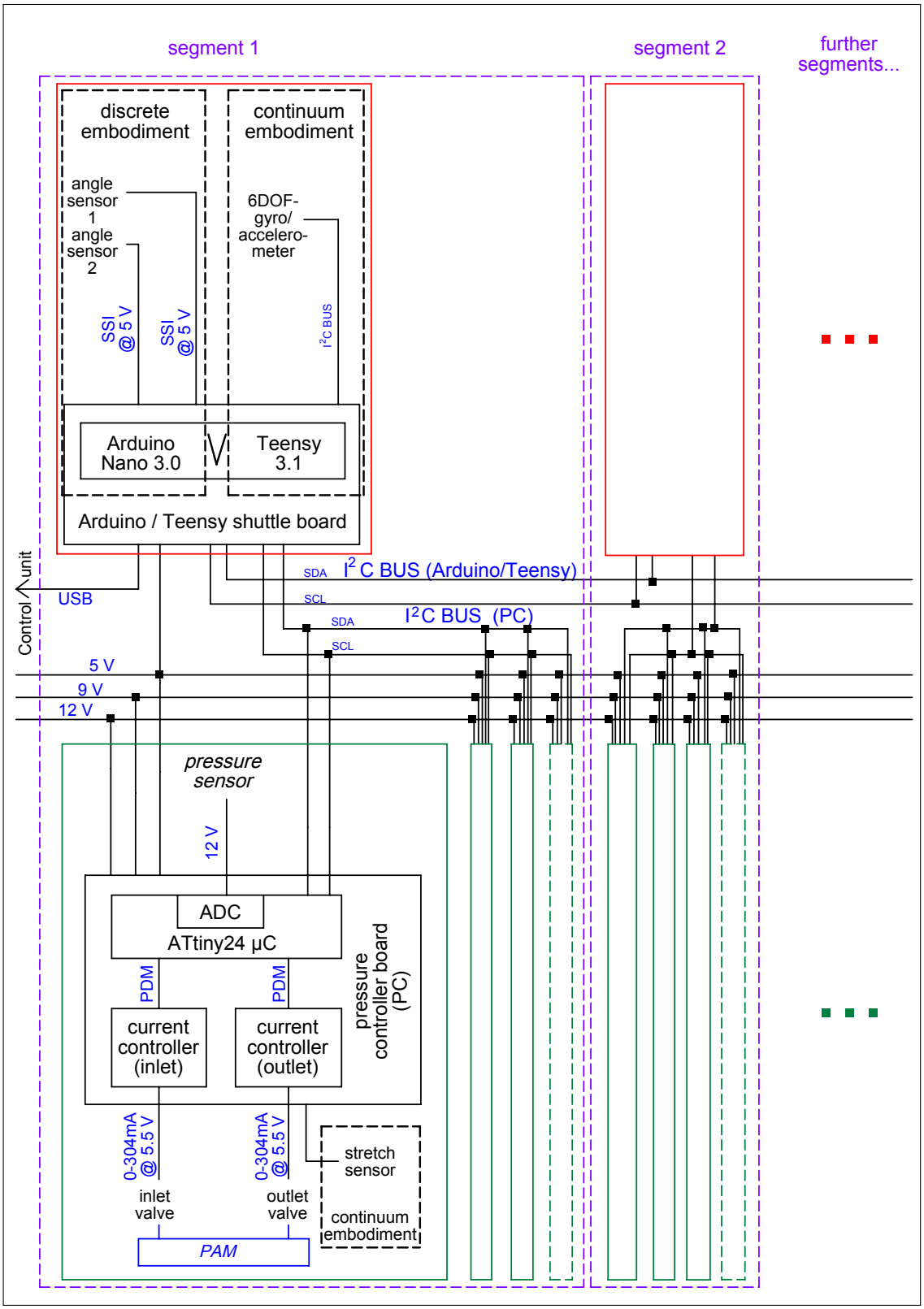

Figure 5.11: Hardware architecture

Chapter 6

Experimental results

For the evaluation of the decentral modular control concept of the worm-like robotic prototypes, experimental tests have to be conducted. In this manner the target achievement of targets already set in Chapter 2 can be ensured. According to previous predictions, the modular arrangement should result in benefits in terms of control performance, as there is a very direct connection between pneumatic actuator supply and PAM actuators. The following experimental investigations focus on position and force measurements, taking modularity aspects into account. Experiments are divided into tests with the discrete worm-like robot and the continuum worm-like robot. In the continuum style case, additional movement tests are performed, which determine the workspace. The question about workspace is much harder to answer for the continuum mechanism than for the discrete one.

6.1 Experimental tests – discrete case

To estimate the quality of the proposed decentralized control approach with respect to the discrete robot prototype, different analyses with one and three segments are performed, utilizing a PID controller and calibrated PAMs (cf. section 5.2). Motion or angle measurements are all conducted with the absolute magnetic rotary encoder joint angle sensors, which have a 12 bit resolution and can be read out at a frequency of maximum 1 MHz, as introduced in subsection 3.6.4. Force or torque measurements are based on a load cell sensor and a Wheatstone Bridge, which are more precisely described in subsection 6.1.4. All experiments are conducted five times and gained results are averaged. Feasibility and precision of motions are crucial criteria, as well as power generation and compliance. First one segment and in a second step three segments are evaluated. Also the differences of the actual decentralized setup and a centralized comparative system are covered.

The most important specifications of the measuring devices and their adjustments for the experiments are summarized in Table 6.1, which are the basis for all discrete case tests, i.e. position (cf. subsections 6.1.1, 6.1.2, and 6.1.3) and force or torque identifications (cf. subsection 6.1.4).

Table 6.1: Testbed features for experiments – discrete case

Feature	*Value*
Analog SMC PSE-510 pressure sensor (data processed with ATtiny 24)	
Repeatability	0.3 % F.S. or less
ADC resolution	10 bit
Max. read-out frequency	50 kHz
Absolute rotary encoder (ams AS5145H)	
Resolution	12 bit
Max. read-out frequency	1 MHz
Load cell force sensor (Phidgets CZL635)	
Rated output error	$\pm$150 µV/V
Precision	0.05 %
Force range	0-200N
Max. read-out frequency	125 Hz
Wheatstone Bridge (PhidgetBridge 1046)	
Differential voltage resolution	24 bit
Data rate	8 ms
Output interface	USB

6.1.1 One-segment tests

Each of the mechanism's segments has the same layout. For this reason, first tests are carried out on a segment isolated from a modular arrangement. Understanding one module of the mechanism helps to get a feeling for what can be achieved with a serial linking of several segments.

In an initial step just one cardan joint axis is moved, actual and desired angles utilizing rotary encoders are recorded and processed. The most critical movements are close to the horizontal state of the moving disc, i.e. when the joint angle is very small or even zero. That's why tilt angles only up to $\pm 3.6^\circ$ are tested, which are performed as rotary sine wave movements. Figure 6.1 depicts the experimental setup that is used for these tests.

Measuring results of this initial examination are summarized in Figures 6.2(a)-6.2(b). Figure 6.2(a) depicts the actual angles θ in a solid line and desired angles θ_{des} as a dashed line. The angle errors $\Delta\theta$ are plotted separately within Figure 6.2(b). An overall mean angle error of approximately 0.14° and a maximum deviation of about 0.45° can be recorded. These maximum deviations occur within the aforementioned horizontal positions at very small angles. At this horizontal position the cardan joint and the moving disc reach a labile state of equilibrium, which causes larger errors. Also there are peaks visible at the reverse points. The reason for

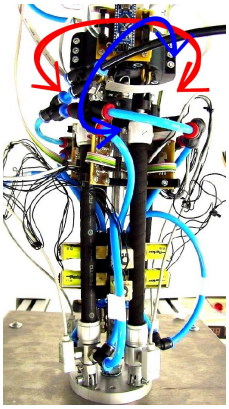

Figure 6.1: Movement tests with one segment – discrete case

this behavior is the reversal of the PAM pair shortening, as for moving the joint always one PAM shortens while the other one has to stretch. When the movement goes from one direction to the other direction, both PAMs of one antagonistic pair have to switch from shortening to stretching and vice versa.

As a second step, both PAM pairs of a first segment are considered, based on the same setup as introduced before. Instead of applying a single sine wave to one joint, both cardan joints of the segment are moved in a sinusoidal manner. This results in a circular movement of the upper disc. Measuring data of this experiment are concluded in the Figures 6.2(c)-6.2(d). Actual and desired angles of the first (blue) and the second (red) PAM pair are shown in Figure 6.2(c), corresponding errors in Figure 6.2(d). Simultaneous motions of both joints lead to mutual influence, hence the errors are higher than in the single joint case. The overall mean error angle of both joints is 0.43° – 0.36° for the first PAM pair and 0.49° for the second pair. Maximum deviations are recorded with 1.4° and 1.3°. Slightly different behavior of the two joints is caused by different calibration effects, as each of the PAM pairs is calibrated separately. This again is due to material deviations and the calibration procedure itself, since muscle parameters are identified using sensors with limited ADC resolution and also due to the fact that the generated fitting functions have mapping accuracy imperfections.

The third examination with the single segment aims to analyze the influence of additional loads. For this purpose, the setup is attached to a table and aligned in parallel to the floor, i.e. the longitudinal axis of the segment is horizontal (cf. Figure 6.3). Another rod is fixed to the moving disc of the segment and a laterally moveable weight is fixed on this rod. This configuration allows to adjust various loads or torques for the cardan joint axes, as the distance between the weight and the joint is variable. In this way, torque values of 0.7 N m, 2.1 N m, and 2.5 N m are evaluated.

Figure 6.4 presents the results of the different load scenarios. Two interesting phenomena can be identified. There is a difference between the first and the second PAM pair for all payloads. Background of this difference is the orientation of the segment, i.e. the first PAM pair is aligned parallel to the floor and arranged in one plane, which is perpendicular to the floor. Instead, the muscles of the second PAM pair are in a plane that is parallel to the floor. This way, only the first pair has to deal with gravity components. Another interesting fact is that with an increase of load there is only minor growth of mean errors at the first axis and even reduction of errors at the second axis. It is logical to assume that greater loads mean greater mass moments of

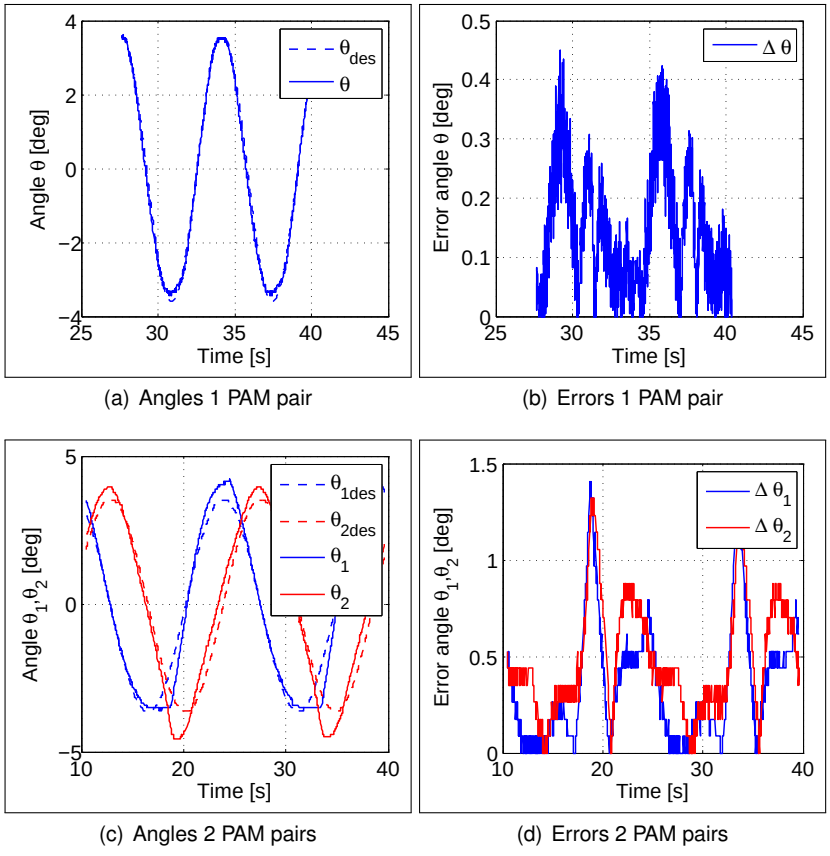

(a) Angles 1 PAM pair (b) Errors 1 PAM pair

(c) Angles 2 PAM pairs (d) Errors 2 PAM pairs

Figure 6.2: Movement experiments sinusoidal joint motions – discrete case (I) (cf. [32])

inertia, which can smooth the motions. As long as the loads are within the payload range of the PAMs, it can be determined that the motions are steadier if additional load is applied. Table 6.2 outlines all measurement results with the first segment.

6.1.2 Three-segment tests

Subsequent to what was stated in the previous subsection 6.1.1, tests were also conducted with an assembly of three segments, i.e. a first prototype of a worm-like robotic mechanism in a discrete embodiment (cf. Figure 6.5). All of the segments are equally equipped with the same types of PAMs, valves and sensors.

Three different kinds of experiments are carried out to identify movement accuracy. In a first step, sinusoidal movements of all three segments S1-S3 (six joint angles Θ_1-Θ_6) are performed in an open loop (cf. appendix Figure A.2). Second, these movements run in a closed loop considering angle encoder feedback (cf. Figure 6.6). The rotational speed is adjusted to a normal speed of 1 °/s. A third experiment identifies the influence of higher velocities, i.e. these tests are examined with triple speed 3 °/s (cf. appendix Figure A.3). All experiments are based on short air feed tube connections, which means that the stub lines between the valves and the actuators are as short as possible (about 0.1 m only). The entire mechanism is hanging upside down with the base segment S1 mounted on a plate (cf. Figure 6.5).

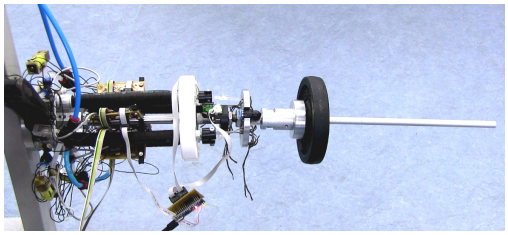

Figure 6.3: One-segment test under load – discrete case

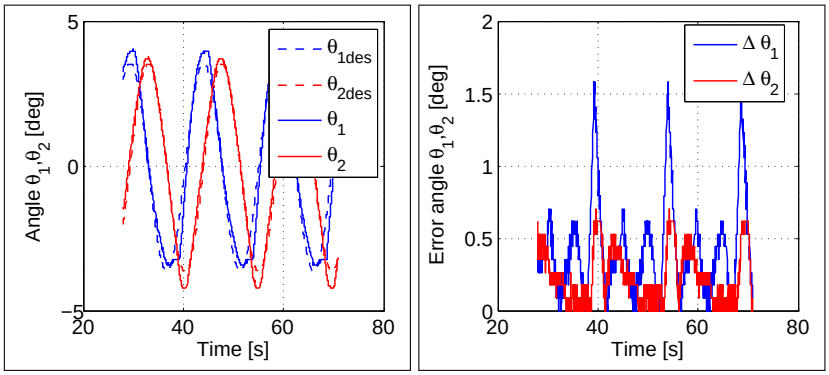

(a) Angles 2 PAM pairs, 0.71 N m load (b) Errors 2 PAM pairs, 0.71 N m load

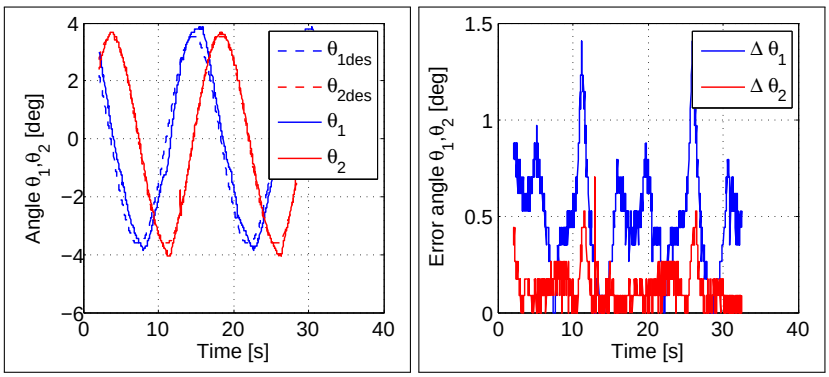

(c) Angles 2 PAM pairs, 2.08 N m load (d) Errors 2 PAM pairs, 2.08 N m load

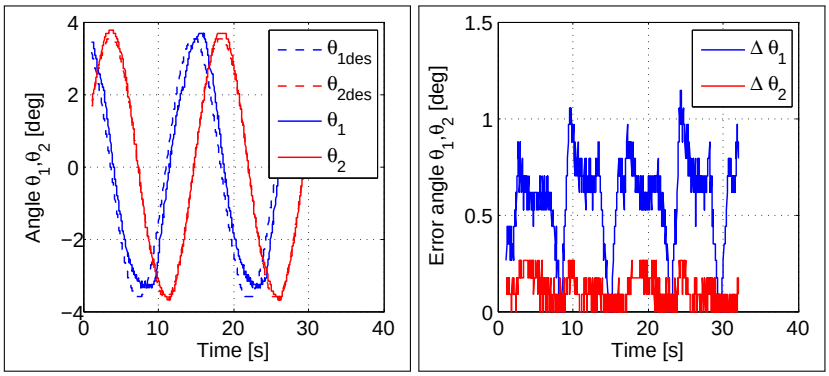

(e) Angles 2 PAM pairs, 2.51 N m load (f) Errors 2 PAM pairs, 2.51 N m load

Figure 6.4: Movement experiments sinusoidal joint motions – discrete case (II) (cf. [32])

Table 6.2: Experimental results for one segment – discrete case

Test case	*Mean error pair 1*	*Max. error pair 1*	*Std. deviation pair 1*	*Mean error pair 2*	*Max. error pair 2*	*Std. deviation pair 2*
One-axis movement	0.14°	0.45°	0.10°	—	—	—
Two-axes movement	0.36°	1.41°	0.32°	0.49°	1.32°	0.29°
0.7 N m load	0.43°	1.58°	0.33°	0.24°	0.70°	1.89°
2.1 N m load	0.49°	1.41°	0.27°	0.13°	0.70°	0.11°
2.5 N m load	0.58°	1.14°	0.23°	0.10°	0.26°	0.08°

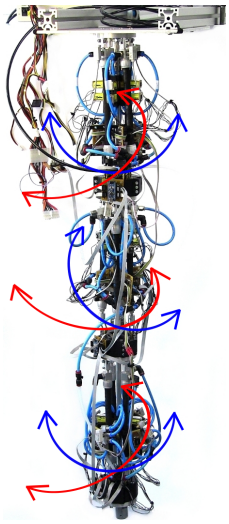

Figure 6.5: Movement tests with three segments – discrete case

Results of these three different measurements are outlined in Table 6.3. The deviations in open loop[1] have maximum values and it is visible that the inertially fixed first segment S1 has much fewer positioning problems than the following segment S2, and S3 has some more deviations. As expected, closed loop experiments with the mechanism lead to a better performance. S1 reaches a position accuracy with a mean error of 0.5° for both cardan angles θ_1 and θ_2. The subsequent segment S2 features angle deviations of 1.0° and 1.4° for θ_3 and θ_4, which are higher than for S1. Differences are caused by the fact that the previous segment S1 as well as the following segment S3 already have some deviations or vibrations themselves, which have influence on the behavior of S2 in between. The last segment S3 has slightly fewer angular position errors with 0.9° and 1.1° for θ_5 and θ_6. Hence, the deviations of S3 are higher than the ones of S1, but diminished compared to S2. In contrast to S2, S3 doesn't have vibration influence from neighboring segments at both ends, but only from one side. It is easier for the controller to follow the given trajectory with more accuracy. Deviations of the two angles of one cardan joint are caused by minor divergences of the calibration for the PAM pairs, which again

[1] considering only pressure sensor feedback, but not angular sensor feedback

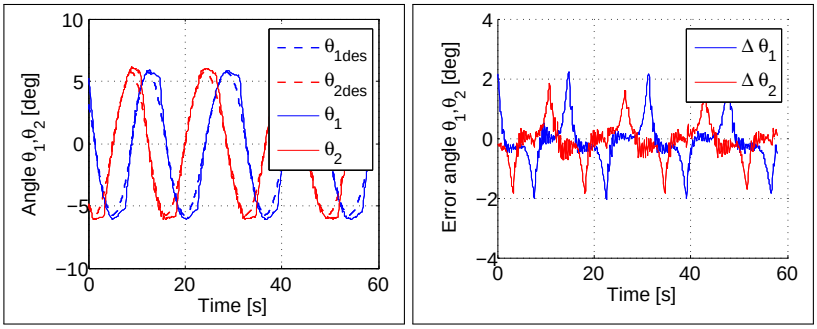

(a) Angles normal speed/short tubes S1 (b) Errors normal speed/short tubes S1

(c) Angles normal speed/short tubes S2 (d) Errors normal speed/short tubes S2

(e) Angles normal speed/short tubes S3 (f) Errors normal speed/short tubes S3

Figure 6.6: Movement diagrams closed loop – discrete case (cf. [34])

is due to material properties and manufacturing precision. Thus, it can be summarized that the inertially fixed segment S1 shows the best performance at lower speeds, followed by S3, which is only influenced by S2, whereas S2 suffers from highest deviations caused by impacts from both S1 and S3. When it comes to increased speed, i.e. triple speed of 3 °/s, there is only marginal discrepancy of segment S3 and some more with S2 as compared to normal single speed. However, there is much more angle error that occurs within S1 applying high speed. It can be explained by the fact that the increased velocity is coupled with dynamic effects, and segments closer to the inertially fixed base have to deal with greater dynamic torques or forces. This effect gets worse, the faster the system is moved and the less distance is between a segment and the basement.

Table 6.3: Experimental results for three segments – discrete case

Type	*Mean error pair 1*	*Max. error pair 1*	*Std. deviation pair 1*	*Mean error pair 2*	*Max. error pair 2*	*Std. deviation pair 2*
Open loop S1	2.45°	5.53°	1.50°	5.20°	10.65°	2.53°
Closed loop S1	0.52°	2.24°	0.54°	0.45°	1.84°	0.43°
Closed loop triple speed S1	1.61°	5.27°	1.28°	1.39°	4.39°	1.00°
Open loop S2	3.47°	9.24°	2.54°	4.68°	10.81°	2.99°
Closed loop S2	1.02°	2.51°	0.65°	1.42°	3.06°	0.93°
Closed loop triple speed S2	1.17°	2.61°	0.74°	1.50°	3.46°	0.96°
Open loop S3	4.72°	10.23°	2.70°	6.41°	13.10°	3.09°
Closed loop S3	0.92°	2.33°	0.57°	1.12°	2.43°	0.63°
Closed loop triple speed S3	0.91°	2.22°	0.60°	1.05°	2.54°	0.66°

6.1.3 Comparison of decentral vs. central feed

As announced in section 6.1, additional tests that compare decentral vs. central feed and their impact on control quality shall be conducted. According to one of the hypotheses of this dissertation, there should be a control accuracy benefit of a single central air feed tube with very short stub lines, directly located at each segment, compared to a decentral feed line arrangement with very long pipes, all ending at a basement. To identify the influence of the feed line length, movement experiments with pipes are considered, which have an additional length. Instead of short stub lines with only 0.1 m, as used in subsection 6.1.2, the tubes have a size of 3.1 m. This way, the existing robotic setup can be used without completely rearranging all the valves, which should actually be located at a common basement and are to be connected with long lines to all of the segments. Putting extended pipes between valves and actuators allows to emulate a system with decentral feed, which still utilizes the central feed arrangement, given by the current prototype. So the mechanism as depicted in Figure 6.5 is only modified by integrating longer stub tubes, which can be easily implemented thanks to the *PushFit* connectors of the pneumatic system. In the following, Figure 6.7 shows circular movement tests with long tubes at normal speed (1 °/s). Triple speed tests at 3 °/s are depicted in the appendix within Figure A.4. Table 6.4 presents the experimental results with 3.1 m tubes in a bundled way. If these results are compared to the ones highlighted in Table 6.3, which deals with short stub lines (0.1 m length), several conclusions can be drawn. Comparing single speed values, the maximum errors of S1

have most significance with an increase of 17.5 %, S2 errors have a value of 9 % and S3 only 4 %. Triple speed evaluations show maximum error increase of 2 % for S1, 34 % for S2, and 4 % again for S3. The error growth at S1 using long tubes is more dominant at lower speed, but for S2 the faster movements are more harmful. However, S3 is less influenced by the elongation and behaves similar at both velocities. In order to better understand the deterioration of the angle errors with longer tubes, reference is made to section 6.3, which gives more details about valve and pressure dynamics effects.

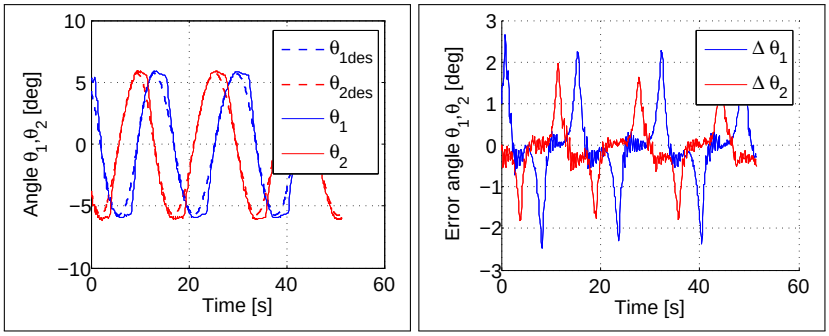

(a) Angles normal speed/3 m tubes S1

(b) Errors normal speed/3 m tubes S1

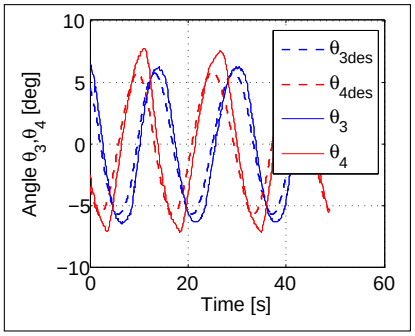

(c) Angles normal speed/3 m tubes S2

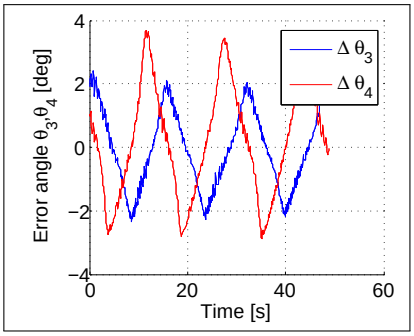

(d) Errors normal speed/3 m tubes S2

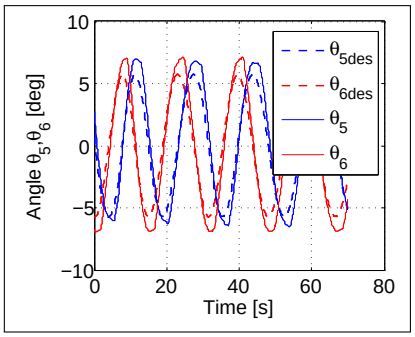

(e) Angles normal speed/3 m tubes S3

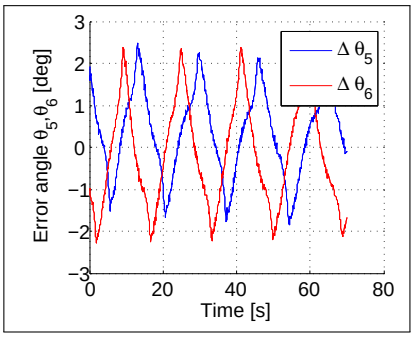

(f) Errors normal speed/3 m tubes S3

Figure 6.7: Movement diagrams with long tubes – discrete case

6.1.4 Force and torque tests

Additionally to the previously described motion tests, measurements of feasible force and torque generation of the segments are evaluated. It is possible to derive the power of the entire mech-

Table 6.4: Experimental results with long tubes – discrete case

Type	*Mean error pair 1*	*Max. error pair 1*	*Std. deviation pair 1*	*Mean error pair 2*	*Max. error pair 2*	*Std. deviation pair 2*
Long tubes normal speed S1	0.58°	2.66°	0.64°	0.44°	1.96°	0.46°
Long tubes triple speed S1	1.62°	4.39°	1.24°	1.48°	4.17°	1.10°
Long tubes normal speed S2	1.07°	2.42°	0.66°	1.48°	3.69°	1.00°
Long tubes triple speed S2	1.50°	3.46°	0.89°	1.95°	4.72°	1.21°
Long tubes normal speed S3	0.91°	2.47°	0.60°	1.10°	2.38°	0.64°
Long tubes triple speed S3	1.02°	2.34°	0.69°	1.16°	2.57°	0.72°

anism, in particular at the end of the last segment, which is the robot's flange. The torque is measured by means of a micro load cell, Phidgets type CZL635 (cf. Table 6.1), i.e. actually forces are measured. After a multiple point calibration the load cell is put at a certain lever arm with respect to the cardan joint axes, and one can derive torque values. Data preparation of the load cell strain gauges is performed using a Wheatstone Bridge device (cf. Table 6.1), which allows to identify pure shear forces. Figure 6.8 shows the load cell (highlighted with a white circle), its supporting rods and the Wheatstone Bridge (top right). The cell is rigidly connected to the central rod of a segment of the worm-like robotic mechanism, utilizing a metal distance bolt, which makes the detection of both tensile and compressive forces possible. For the experiment, the PAM actuators of the first segment are tensioned and thus torque is generated to move the subsequent segment, which rotates about the cardan joint axes. The load cell is placed such that it is exactly aligned with one of these joint axes. In this way, the torque capability of one segment joint is evaluated.

6.9 bar reference pressure is set during these tests, which is the maximum pressure for the valves. The output torque depends on the joint angle and thus on the contraction state of the PAMs. A maximum value of about 6.3 N m can be reached at a joint angle of 16°, at 0° the torque is only 3.8 N m. Results of an exemplary force or torque evaluation are given in Figure 6.9. This figure shows oscillating angle movements in the range between 0.3° and 1.2°. It indicates the variable output torque. The calculation of the allowable loads at the robot's flange are based on the torque values of a single segment. Considering the case of three segments results in the following forces. If the mechanism is mounted upside down, a lateral force of 5 N is possible for

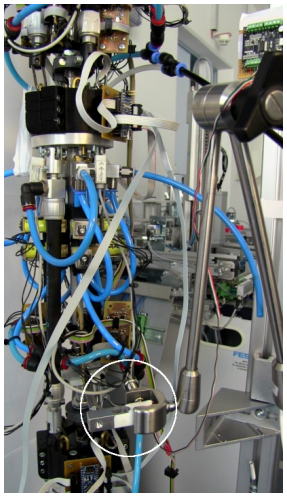

Figure 6.8: Setup for force/torque test with load cell – discrete case

a completely stretched configuration, and in a fully deflected state of all three segments a lateral force of 2.1 N and a weight of 5 N can be balanced.

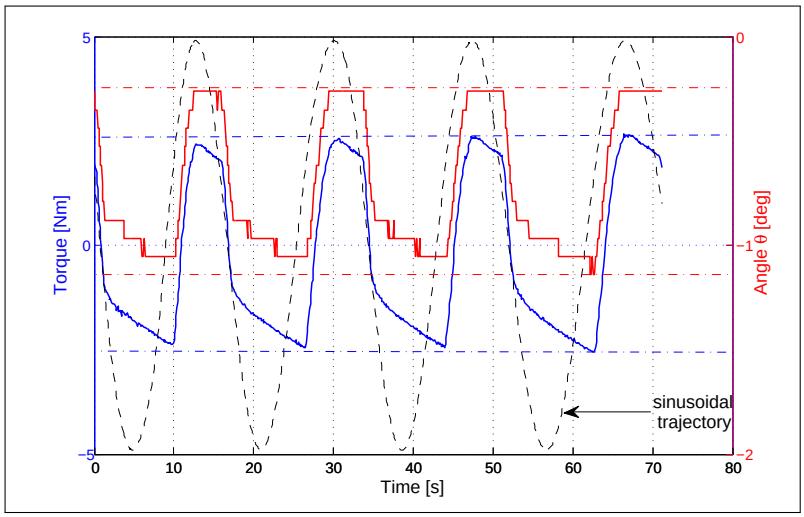

Figure 6.9: Torque tests – discrete case (cf. [34])

6.2 Experimental tests – continuum case

Similar to section 6.2 before, the continuum worm-like robotic mechanism prototype is evaluated with attention paid to control performance. The benefit of a decentralized setup shall be proved once again. In a first step, only one continuum segment is tested, in a second step all four segments of a continuum worm-like robotic mechanism are considered. In contrast to the discrete mechanism, an adequate detection of movement positions of the continuum robot is much more challenging. The reason for this is the difficulty that the kinematics model suffers from deviations, as the poses of the segments cannot be measured directly. More effort is

necessary to determine the geometric configuration of the flexible segments. Stretch sensors, as introduced in subsection 3.6.5, are used as primary position detectors, but to enhance the measurement accuracy, additional gyroscopes plus acceleration sensors are already prepared for future use. In order to be sure that the sensor feedback is valid, an external supplemental tracking system is applied for the experiments. The tracking system allows to monitor the flange movements at the end of the last segment. In this way, errors in measurements of single segments that accumulate towards the mechanism's end, can be cross-checked by an external measuring device that generates position and orientation information with respect to a world coordinate frame.

To get an overview about the measurement devices and their setting, relevant data are outlined in Table 6.5. Devices that were already utilized within the discrete case experiments, such as the pressure sensors and the load cell including the Wheatstone Bridge, are not listed again – the reader shall be referred to Table 6.1. For the experiments described later on, pressure sensors (cf. subsection 3.6.3), stretch sensors (cf. subsection 3.6.5), gyroscopes and acceleration sensors (cf. subsection 3.6.6), an electromagnetic tracking device, Teensy microcontroller chip ARM Cortex M4 (cf. subsection 3.5.1) and ATtiny 24 within the customized pressure controller board (cf. subsection 3.5.2) are utilized. The electromagnetic tracking system is chosen, because it has a high tracking resolution and does not suffer from shadowing effects, as it would be the case for an optical tracking system. However, it has to be considered that there are many metal parts on the mechanism's segments, which can distort the tracking. To avoid this distortion, the six DOF sensor that is tracked has to be placed with a distance of about 6 cm from the moving plate of the segment that is monitored. Regarding the experimental accomplishment, as in the discrete case, each experiment is conducted five times and measured data are averaged.

6.2.1 One-segment tests

An initial evaluation of the continuum case prototype is done with one segment. The length information of all three stretch sensors (cf. subsection 3.6.5), attached to the three PAMs, and gyroscope or acceleration sensor (cf. subsection 3.6.6) data are recorded while moving the segment. Simultaneously an external electromagnetic tracking system is used to identify the motions with 1.4 mm translational precision (RMS) and 0.5° orientation accuracy (RMS). Figure 6.10 depicts this experimental setup. It shows the test environment of the robot segment with an electromagnetic sensor mounted on top (centre)[2], a transmitter box (top left), an electronics unit (top right) plus a pre-amplifier (right and below electronics unit).

For a start, different kinds of movements are tested with a single continuum segment:[3]

- Back and forth – movement mainly along the x-axis,
- Right and left – movement mainly along the y-axis,
- Up and down – movement mainly along the z-axis,
- Circular – movement mainly in a sinusoidal manner, i.e. the moving top plate of the segment fulfills a precessing motion about its vertical z-axis,

[2] highlighted with a black circle; mounted using a non-metallic distance piece

[3] corresponding axes are with respect to the magnetic tracking system coordinate frame that is given by the transmitter box

Table 6.5: Testbed features for experiments – continuum case

Feature	*Value*
Stretch sensor (Images Scientific Instruments, signal evaluation via Teensy 3.1 ADC)	
ADC resolution	16 bit SAR
Max. sampling frequency	2 MHz
6-DOF gyroscope and acceleration sensor (MPU-6050)	
Interface	i^2C
ADC resolution	16 bit
Max. data rate gyroscope	1 kHz
Max. data rate acceleration sensor	1 kHz
Rate sensor range	$\pm$250 °/s
Accelerometer sensor range	$\pm$ 2 g
Total RMS noise gyroscope	0.05 °/s RMS
Noise performance acceleration sensor (power spectral density)	400 $\frac{\mu g}{\sqrt{Hz}}$
Electromagnetic tracking 3D Guidance medSAFE (Ascension Technology Corporation)	
Range of mid-range transmitter	$\pm$76 cm
Sensor (used with pre-amplifier)	model 180 6DOF
Interface	USB
Measurement rate	115 Hz
Static accuracy translation	1.4 mm RMS
Static accuracy rotation	0.5° RMS
Output	X, Y, Z coordinates, orientation angles

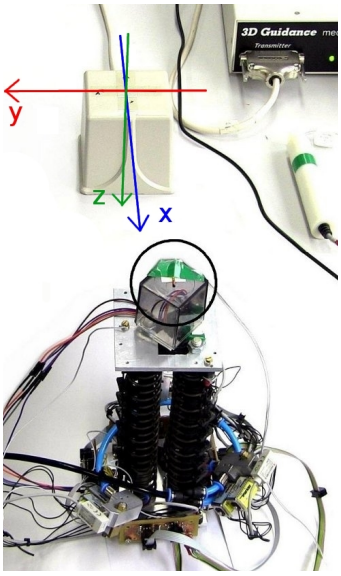

Figure 6.10: Setup for position tests – continuum case

- Jumpy – arbitrary movements with high velocity and acceleration.

Later on, positioning tests are conducted to identify the control quality based on stretch sensor or acceleration sensor and gyroscope feedback. Open loop measurements are included for a better comparison.

Extremal position tests according to the aforementioned itemization[4] are depicted in Figure 6.11. On the left hand side of this figure, example movements (back and forth, right and left, up and down, circular) are shown, and on the right hand side a combination of all of these motions is illustrated in a 3D Delaunay triangulation surface plot to get an impression about the reachable positions. All values are based on electromagnetic tracking measurement data, as already mentioned above in section 6.2.

A first overview about the workspace of such a single continuum style segment was given in subsection 4.2.3, where the spherical shell model was introduced, by means of which the maneuverability of the setup can be described.

Further considerations of reachable positions, velocities and accelerations of a single continuum style segment are summarized in graphics 6.12. These observations are based on randomly performed jumpy motions in order to see the potential of movements of one segment. All motion commands were initiated using a 3D *SpaceMouse*[5] as an input device. The same considerations are taken into account dealing with angles (azimuth, elevation, roll), angular velocities and accelerations. A corresponding figure can be found in the appendix within A.5.

Relevant measurement results and kinematic limits of a single continuum style segment are presented in Table 6.6. In the upper part of the table, maximum values for positions that can be approached as well as maximum velocity and acceleration rates are shown. Regarding the rotational case, angles and angular velocities or angular accelerations are included in the lower part of the table. The values for both x- and y-directions are equivalent, but the ones in z-

[4] with the exception of the jumpy movements, which are omitted for reasons of clarity
[5] space navigator utilizing a six DOF sensor by 3D connexion GmbH

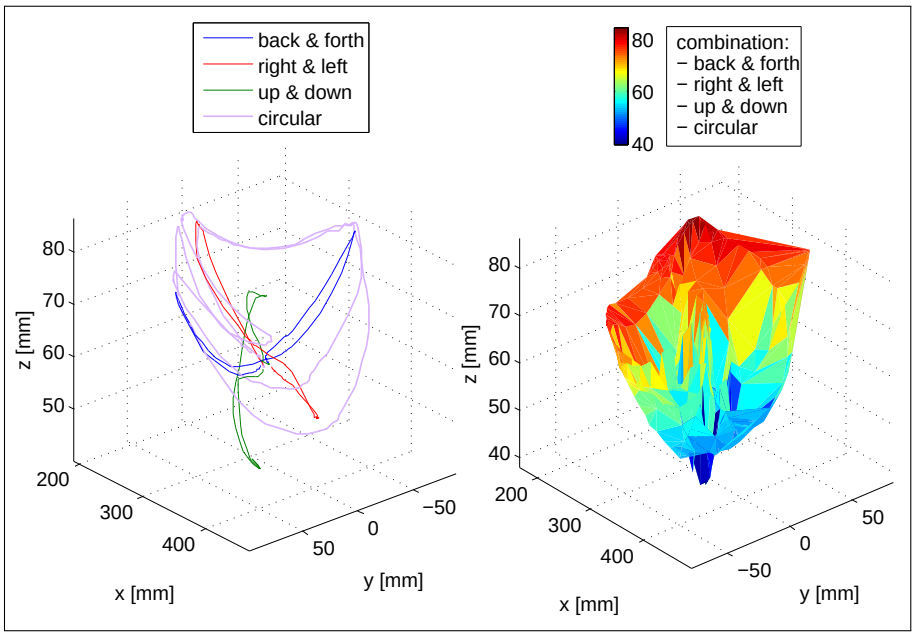

Figure 6.11: Position tests with one segment – continuum case

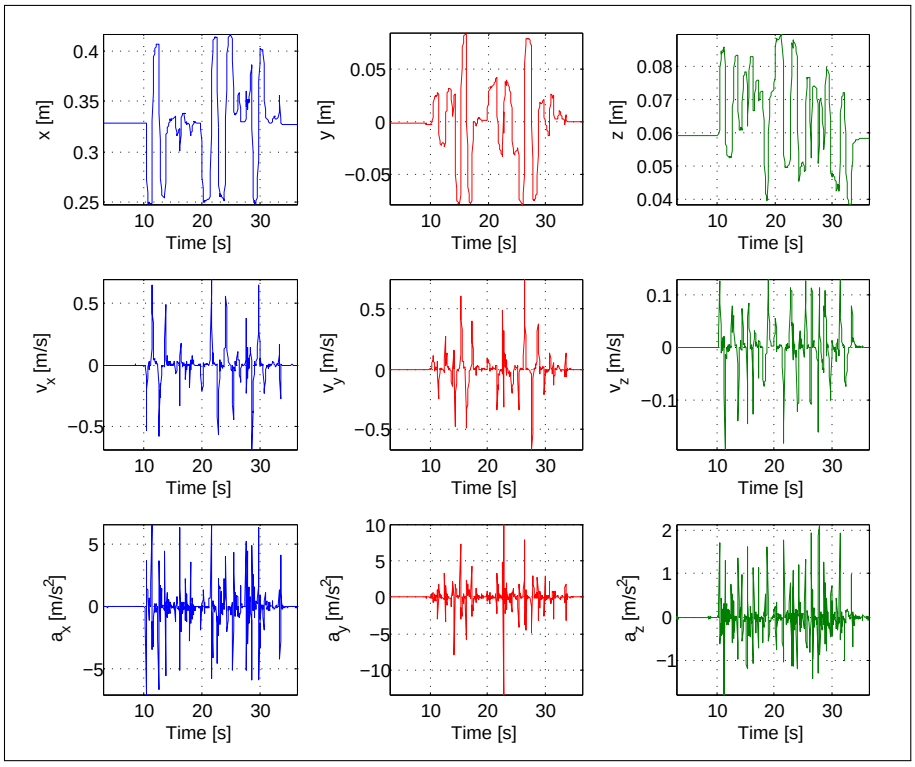

Figure 6.12: Position, velocity and acceleration tests with one segment – continuum case

direction vary widely. Positions/angles and their time derivatives in x- and y-direction depend on the bending of the PAM actuators, any z-direction changes go together with only shortening and extension of the muscles. Bending of the muscle actuators is caused by differential shortening/extension of the PAMs, which amplify pure position/angle changes (including their time derivatives), as there is a kind of lever arm, which is almost equal to the actual length of the muscle that is actuated. Movements in only z-direction don't have much influence from such an amplifying quasi lever arm, that's why all z-components are far lower than x- and y-components. It should be noted that the term "azimuth" in this context is with respect to an inertial coordinate frame of the electromagnetic tracking system and its transmitter box (cf. Figure 6.10), i.e. there are no real azimuth motions about the z-axis (torsion about the central axis or "neutral fiber") feasible if one considers a coordinate system fixed to the body. All PAMs can only shorten/extend or bend around themselves, but twisting is not possible. Azimuth angles, velocities and accelerations are simply due to shaking effects, as there is no driven DOF about the z-axis.

Table 6.6: Summary of position, velocity and acceleration ranges of one segment – continuum case

Feature	*Value*
Range in x/y-direction	± 80 mm
Range in z-direction	± 20 mm
Velocity in x/y-direction	± 0.6 m/s
Velocity in z-direction	± 0.15 m/s
Acceleration in x/y-direction	± 7 m/s^2
Acceleration in z-direction	± 2 m/s^2
Azimuth angle	$\pm 1.1°$
Elevation angle	$\pm 31°$
Roll angle	$\pm 30°$
Azimuth angular velocity	± 37 °/s
Elevation angular velocity	± 173 °/s
Roll angular velocity	± 253 °/s
Azimuth angular acceleration	± 602 °/s^2
Elevation angular acceleration	± 1790 °/s^2
Roll angular acceleration	± 2843 °/s^2

Complementary to the experiments above, tests to identify the control accuracy of the setup are performed in the following. The quality of the control of the robotic system is measured in two steps:
(1) Open loop positioning of one segment,
(2) Closed loop positioning of one segment with stretch sensor feedback.

(1) Positioning tests in an open loop with recorded stretch sensor values already confirm the

challenges that are coupled with continuum kinematics. Figure 6.13 illustrates back and forth movements, which are separated into recordings for Cartesian x/y/z motions and each of the three stretch sensor lengths. Additionally, left and right, up and down, circular and randomized movements are depicted within figures in the appendix (cf. Figures A.7, A.8, A.9, and A.10).

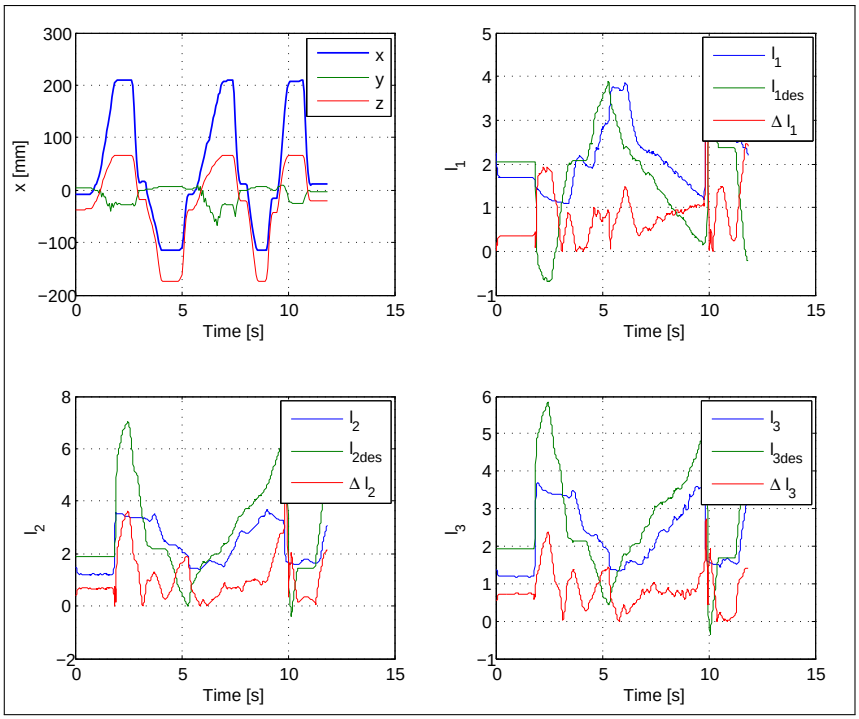

Figure 6.13: Open loop back and forth movement of one segment – continuum case

(2) Experiments in a closed loop with stretch sensor feedback are discussed in the following. As it can be already seen in Figure A.8, up and down motions suffer from maximum deviations. Kinematic specifics, such as singularity issues in case of pure elongation/shortening, are responsible for these high discrepancies. For this reason, closed loop tests are carried out that consider such up and down movements. As mentioned before in section 5.5, a control based on a sliding mode approach is implemented to deal with the nonlinear stretch sensor signals with hysteresis effect. Sensor signal noise and reduced response time due to this hysteresis effect of the stretch sensor is the main cause of errors (cf. Figure 5.10). Figure 6.14 illustrates the movement behavior. It is visible that there are high sensor signal distortions shortly after the reversal point of the given sine trajectory. This is in accordance with what was shown in Figure 3.25, i.e. the irregular sensor relaxation contributes to the feedback noise. However, the sliding mode control approach is able to bring the sensor values immediately back to the trajectory of the set values. Table 6.7 concludes the results of the experiments described in (1) and (2).

6.2.2 Four-segment tests

By analogy with the previous tests in subsection 6.2.1, investigations are carried out with four identical continuum style segments. These four modular units are attached to one another, utilizing knurled screws for an easy assembly and disassembly. In total, the serial arrangement

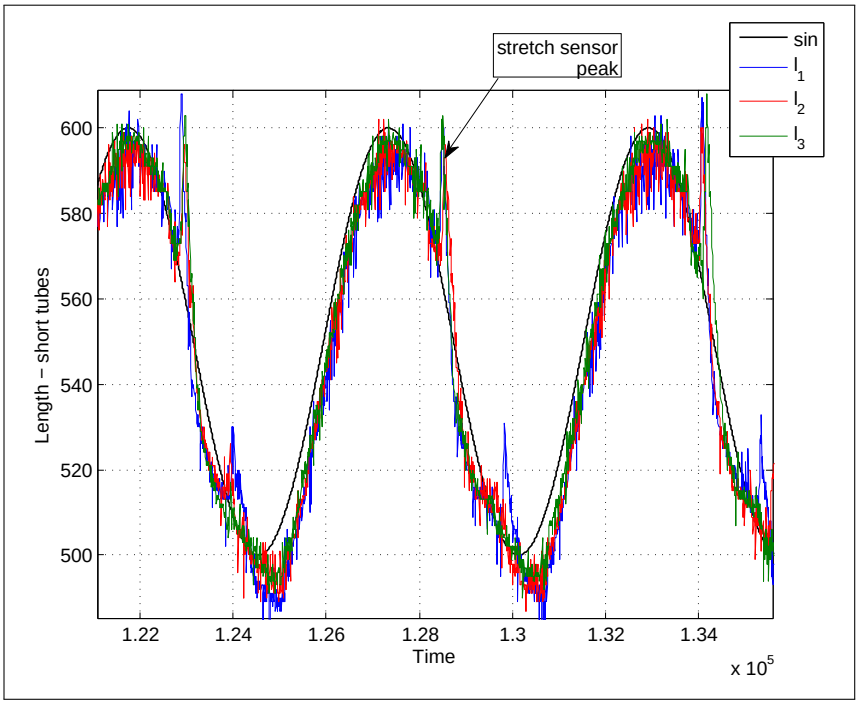

Figure 6.14: Closed loop up and down movement of one segment – continuum case

of four segments ends up in a continuously flexible worm-like robotic arm with an overall number of 12 DOF. Various movement experiments are performed with the robotic setup, which is mounted upside down[6]. These experiments utilize feedback of an electromagnetic tracking system, stretch sensors and acceleration sensors plus gyroscopes. In a first step, the idea is to determine extremal positions, velocities and accelerations that can be reached with a setup comprising four segments. In a second step, the question about control accuracy is taken up, i.e. closed loop positioning tests are conducted.

Initial movement tests consider positions, velocities and accelerations, similar to the ones in 6.2.1. The overview of back and forth, right and left, up and down, and circular position changes is illustrated in Figure 6.15, which gives a first impression of the dimensions of movements with the four-segment setup.

Test results related to positions, velocities and accelerations of four continuum style segments are highlighted in Figure 6.16. To gain relevant information, jumpy motions in various directions are caused, utilizing a *SpaceMouse* interface device. Translational tests are depicted in Figure 6.16, rotational tests are put in the appendix (cf. Figure A.6).

Limits derived from these tests are summarized in Table 6.8. In contrast to the single-segment results within Table 6.6, here the absolute ranges are much larger: in x-direction about seven times, in y-direction more than six times, in z-direction 17 times. These are caused by the amplifying effect of the lever arm and the bending of each segment. However, the curvature of the entire setup is not constant. The robot is based on identical segments that are all equipped with the same types of actuators, so the curvature becomes larger at the unattached end, as the system is hanging upside down. Proximal segments have to carry more payload than distal segments, which causes the differences in curvature. X- and y-directions have slightly distinct

[6] inverted arrangement compared to the upright standing of one segment within Figure 6.10

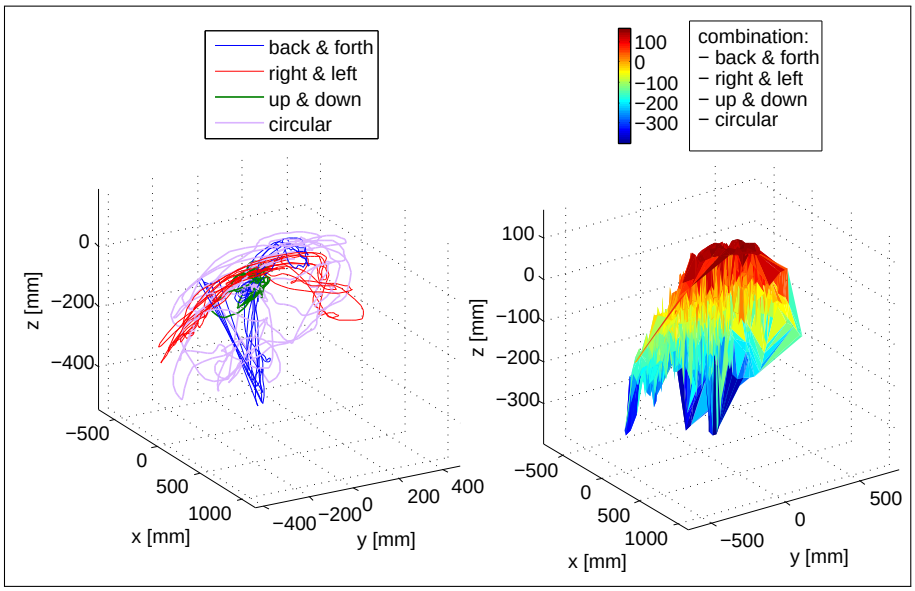

Figure 6.15: Position tests with four segments – continuum case (cf. [33])

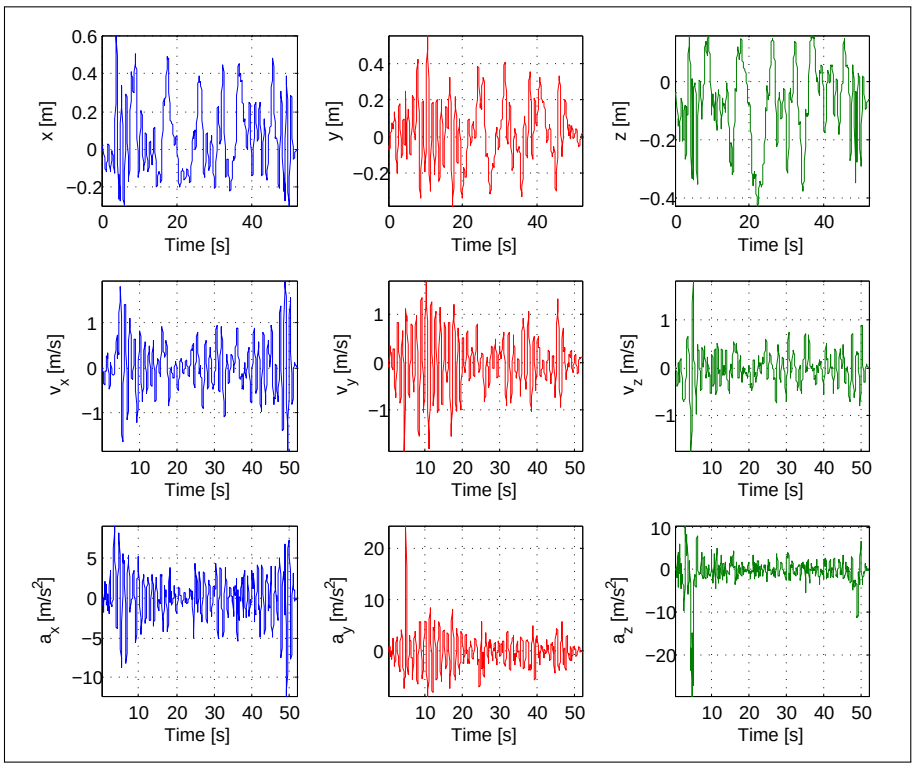

Figure 6.16: Position, velocity and acceleration tests with four segments – continuum case (cf. [33])

Table 6.7: Open/closed loop results for one segment – continuum case

Type open loop	*Mean error* l_1	*Max. error* l_1	*Std. deviation* l_1	*Mean error* l_2	*Max. error* l_2	*Std. deviation* l_2	*Mean error* l_3	*Max. error* l_3	*Std. deviation* l_3
Back and forth	15.8 %	67.0 %	10.9 %	14.0 %	60.1 %	11.5 %	13.3 %	43.9 %	7.9 %
Left and right	27.8 %	74.3 %	17.4 %	11.9 %	58.5 %	7.6 %	10.8 %	70.2 %	11.1 %
Up and down	17.5 %	58.6 %	11.8 %	23.5 %	56.3 %	15.9 %	21.7 %	45.8 %	13.7 %
Circular	17.1 %	52.7 %	12.6 %	18.7 %	43.5 %	11.4 %	20.8 %	61.1 %	19.4 %
Random	24.5 %	52.7 %	13.6 %	22.0 %	61.9 %	13.4 %	20.3 %	53.5 %	13.7 %
Type closed loop	*Mean error* l_1	*Max. error* l_1	*Std. deviation* l_1	*Mean error* l_2	*Max. error* l_2	*Std. deviation* l_2	*Mean error* l_3	*Max. error* l_3	*Std. deviation* l_3
Up and down	1.7 %	9.2 %	1.2 %	1.5 %	8.3 %	1.0 %	1.3 %	9.2 %	1.0 %

ranges, as the arrangement of three PAMs leads to asymmetry[7]. High values for the range in z-direction are due to shortening and bending (sideways) of the segments. If only pure shortening is considered, a maximum range of about 160 mm is given. Both velocity and acceleration in z-direction are lower than for the other directions, which is influenced by the weights/inertias of all serially arranged segments. High azimuth angle peaks are due to oscillation effects that occur during the tests, which are conducted without any feedback control. As already mentioned for the previous one-segment test case, there are no real azimuth motions[8]. Divergences between elevation and roll motions can be explained by the asymmetric arrangement of the PAMs, as indicated in the previous subsection, and by the fact that the feed lines plus wiring components lead to additional dissymmetric behavior.

The experiments above are carried out without any feedback control. In this paragraph the positioning precision of the entire system shall be investigated. The goal is to get an idea about the achievability and the limit of an implemented feedback control system, which is based on a sliding mode control in order to deal with the noisy length sensors. Similar to the one-segment tests, sinusoidal oscillations with a frequency of 0.2 Hz are set to move all four segments up and down continuously. For an evaluation of this test the stretch sensor signals of the proximal segment are recorded. This first segment is the one that has to carry all the other distal

[7] x-axis is an axis of symmetry, y-axis is not; cf. coordinate frame depicted in Figure 6.10, which is aligned with the system of four segments attached upside down, i.e. inverted to the one-segment setup

[8] torsion of the mechanism is not actuated, but oscillation effects cause twist of the segments that are connected with springs and PAMs only

Table 6.8: Summary of position, velocity and acceleration ranges of four segments – continuum case

Feature	*Value*
Range in x-direction	$\pm$585 mm
Range in y-direction	$\pm$518 mm
Range in z-direction	$\pm$342 mm
Velocity in x-direction	$\pm$44 m/s
Velocity in y-direction	$\pm$37 m/s
Velocity in z-direction	$\pm$0.4 m/s
Acceleration in x-direction	$\pm$46 m/s^2
Acceleration in y-direction	$\pm$40 m/s^2
Acceleration in z-direction	$\pm$4.5 m/s^2
Azimuth angle	$\pm$19°
Elevation angle	$\pm$71°
Roll angle	$\pm$65°
Azimuth angular velocity	$\pm$63 °/s
Elevation angular velocity	$\pm$1210 °/s
Roll angular velocity	$\pm$2100 °/s
Azimuth angular acceleration	$\pm$665 °/s^2
Elevation angular acceleration	$\pm$4770 °/s^2
Roll angular acceleration	$\pm$4010 °/s^2

segments and consequently position control of this segment suffers from the most deviations. In Figure 6.17 an extract of this oscillation is depicted for a period of 12.5 s. In addition, the test is conducted with an electromagnetic tracking system, which determines the motions of the flange of the continuum worm-like robotic mechanism. Results of the electromagnetic tracking – recordings for the z-motions – are illustrated in Figure 6.18. Table 6.9 presents the deviation results as relative values with respect to the overall motion range of the entire mechanism, given for short air feed tubes with a length of 0.1 m.

6.2.3 Comparison of decentral vs. central feed

Similar to the tests in the discrete case in 6.1.3, control tests with long and short air supply tubes between the valves and the PAMs are carried out to emulate the behavior of a decentral and a central feed. This again indicates the benefit of short stub lines in contrast to long tubes coming from a distant valve cluster basement. Two different tube lengths were chosen: 0.1 m and 2.1 m. Figure 6.19 shows the recorded stretch sensor length data within a movement based

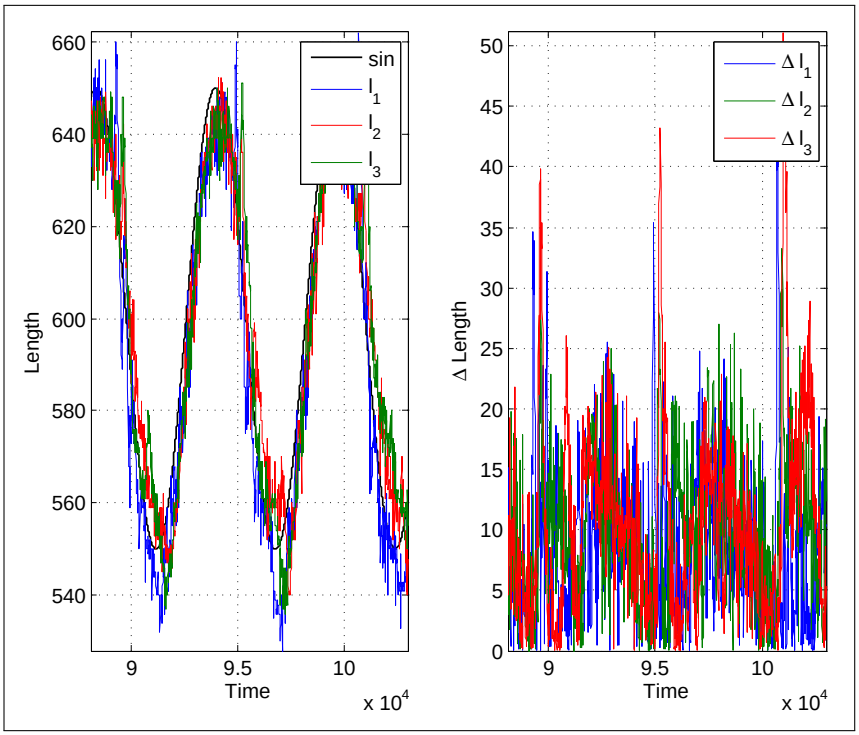

Figure 6.17: Sinusoidal control test with four segments – continuum case (cf. [33])

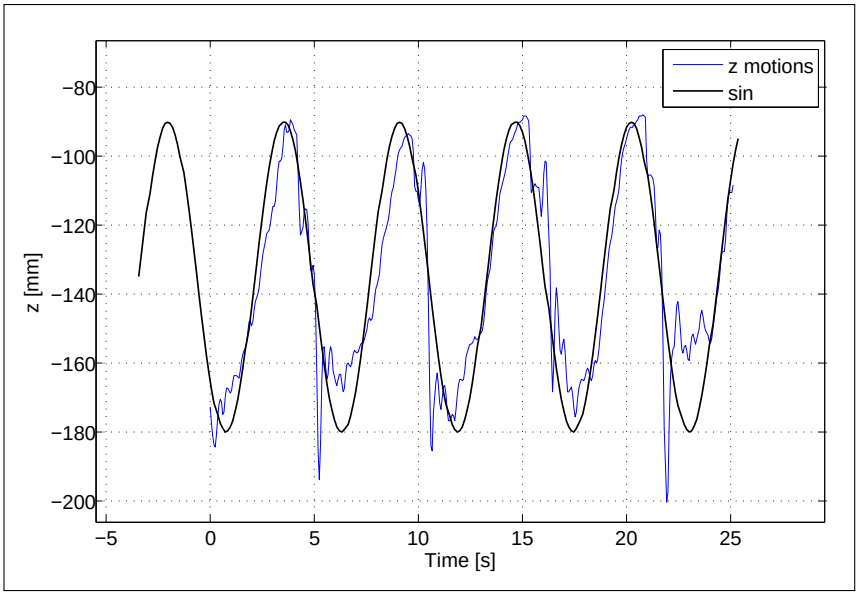

Figure 6.18: Sinusoidal electromagnetic tracking test with four segments – continuum case

Table 6.9: Control results for four segments – continuum case

Type closed loop	*Mean error* l_1	*Max. error* l_1	*Std. deviation* l_1	*Mean error* l_2	*Max. error* l_2	*Std. deviation* l_2	*Mean error* l_3	*Max. error* l_3	*Std. deviation* l_3
Up and down (0.1 m)	1.4 %	7.6 %	1.0 %	1.6 %	5.8 %	0.9 %	1.7 %	8.5 %	1.4 %

on sinusoidal up and down oscillations of one continuum segment. Table 6.10 outlines the test reading, which includes the short tube tests according to Table 6.7. As a result, all length errors increase with the tube extension. The numbers are given as relative values – compared to the mean range of sensor signals. Most dominant are the maximum deviations, which differ appreciably.

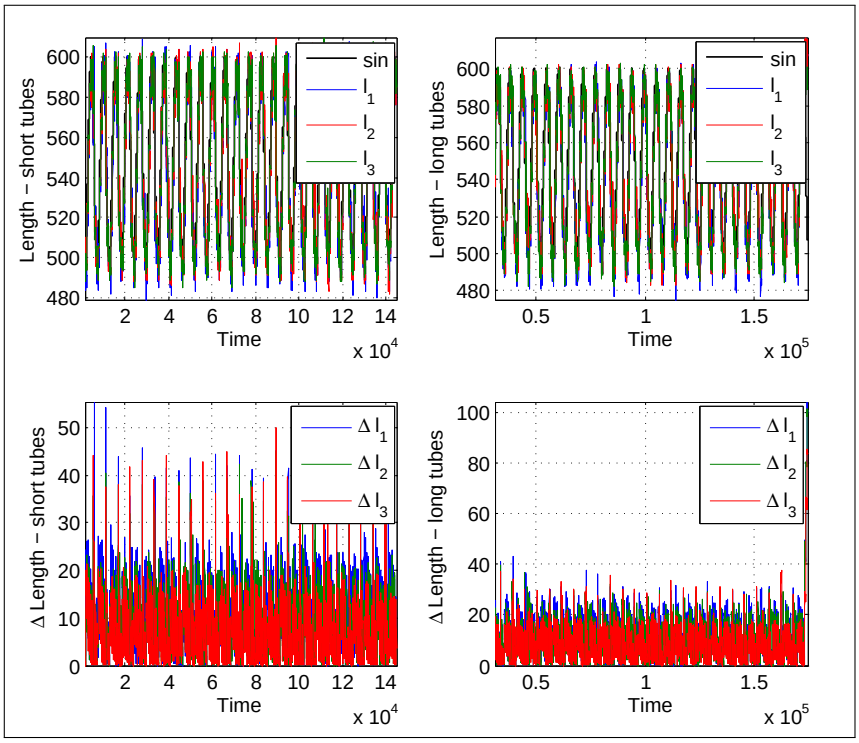

Figure 6.19: Closed loop up and down movement of one segment with varying tube length – continuum case

6.2.4 Force tests

Similar to the method described in subsection 6.1.4, force tests are carried out with the continuum style worm-like robotic setup, utilizing exactly the same measurement devices (cf. Table 6.1). Again, a load cell is fixed to a bar made of steel, and the load cell has to bear com-

Table 6.10: Short/long tube results for one segment – continuum case

Type closed loop	*Mean error* l_1	*Max. error* l_1	*Std. deviation* l_1	*Mean error* l_2	*Max. error* l_2	*Std. deviation* l_2	*Mean error* l_3	*Max. error* l_3	*Std. deviation* l_3
Up and down (0.1 m)	1.7 %	9.2 %	1.2 %	1.5 %	8.3 %	1.0 %	1.3 %	9.2 %	1.0 %
Up and down (2.1 m)	1.9 %	19.1 %	1.6 %	1.7 %	18.7 %	1.6 %	1.5 %	15.7 %	1.3 %

pression forces in x-, y- and z-directions (coordinate system cf. Figure 6.10). Tests with different numbers of segments (from one to four) are performed. Each time the load cell pushes against the moving top plate of the first, second, third, and fourth segment. As the continuum setup can elongate and shorten, forces in z-direction are more relevant than within the discrete prototype case. Maximum forces are epitomized in Table 6.11. Tensile forces in z-direction are given for two examples of different muscle contractions – 0 % and 20 %.

Table 6.11: Maximum forces – continuum case

1 segment		*2 segments*	
Force	*Max. value*	*Force*	*Max. value*
F_{-x}/F_{+x}	16.3 N/12.6 N	F_{-x}/F_{+x}	10.9 N/5.8 N
F_{-y}/F_{+y}	8.8 N/7.7 N	F_{-y}/F_{+y}	7.0 N/6.1 N
$F_{z,0\%}/F_{z,20\%}$	1740 N/65 N	$F_{z,0\%}/F_{z,20\%}$	1730 N/55 N
3 segments		*4 segments*	
Force	*Max. value*	*Force*	*Max. value*
F_{-x}/F_{+x}	7.0 N/3.4 N	F_{-x}/F_{+x}	7.0 N/4.7 N
F_{-y}/F_{+y}	4.9 N/5.3 N	F_{-y}/F_{+y}	4.5 N/4.8 N
$F_{z,0\%}/F_{z,20\%}$	1720 N/45 N	$F_{z,0\%}/F_{z,20\%}$	1710 N/35 N

6.3 Valve and pressure dynamics

Valve dynamics, which is caused by pressure dynamics, has considerable impact on the control accuracy of a pneumatic system, as the valves have to properly adjust the PAM pressure and regulate the entire setup. Tests are conducted to measure the pressure change depending on different valve currents and starting pressure (cf. [137]). This is done in order to reasonably

interpret results from the figures in subsections 6.1.3 and 6.2.3, in which movement experiments are executed using different tube lengths.

The measurements are realized by means of a logic analyzer tool – Saleae Logic Analyzer[9]. Pressure signals come from analog SMC PSE-510 pressure sensors (cf. subsection 3.6.3) with a repeatability of about 0.3 % F.S. Table 6.12 shows a summary of the analyzer tool and its main settings. Characteristics of the pressure sensors were already listed in Table 6.1.

Table 6.12: Testbed features for pressure dynamics experiments

Feature	*Value*
Saleae Logic Analyzer (8 channels)	
Sample rate pressure signal	max. 25 kHz
Sample rate valve current signal	max. 25 kHz

Pressures are set in orders of 0-6.9bar, currents alter between 160 mA and 300 mA, which is the minimum amount of current necessary to open the valve and the maximum allowed current for the coil. The experimental setup comprises one PAM, corresponding inlet and outlet valves, both pressure controller boards, and the Saleae Logic Analyzer device. The latter receives measured data via i^2C bus and transfers it to a GUI PC that allows data collection and post-processing. As a result of these experiments, phase diagrams can be extracted – Figure 6.20(a) for the inlet phase and Figure 6.20(b) for the outlet phase. The pressure change rate depends on the valve current as well as on the valve reference pressure. Within the inflow cycle, the pressure change rates starting from 0 bar increase quickly to a maximum of 3.3 bar. With growing saturation of pressure these rates diminish. This phenomenon is due to the flow characteristics of both valves, the fittings and the PAMs, which are not investigated in more detail. During the exhaust process, which is to be interpreted from right to left (cf. Figure 6.20(b)), phase lines behave quite similar. Inlet and outlet cycles end up with comparable flow rates and pressure changes. The inlet cycle deals with little higher pressure change rates, i.e. about 4.5 bar/s more than within the exhaust phase. This hysteresis behavior is not excessively high, it is in the range of approximately 23 %. Accordingly, the valve dimensions are reasonably chosen, because of the exhaust flow not being substantially lower than the inlet flow. In such a situation, if exhaust rates were extremely lower than inlet rates, either outlet valves with larger orifice would have to be chosen or a second outlet shuttle valve should be implemented, which supports the original outlet valve. In this context, the reader is referred to relevant literature [28].

Figures 6.20(a) and 6.20(b) also indicate that low valve current generates oscillation effects during the opening process of the valve. A threshold of the current that is independent from the starting pressure has to be overcome to get the opening of the valve started[10]. In physical sense this means, that the current of the electromagnetic coil of the valve has to be fed with enough current, such that the inertia of the moving valve components as well as the counter force of the valve spring can be compensated.

This thesis puts forward the hypothesis that the stub tubes, which connect the PAMs of each segment to their valves, are critical in terms of length, i.e. longer stub lines result in control

[9] cf. http://www.saleae.com/logic, last accessed: October 10, 2013

[10] at least currents of 160 mA were necessary for the evaluated worm-like prototypes

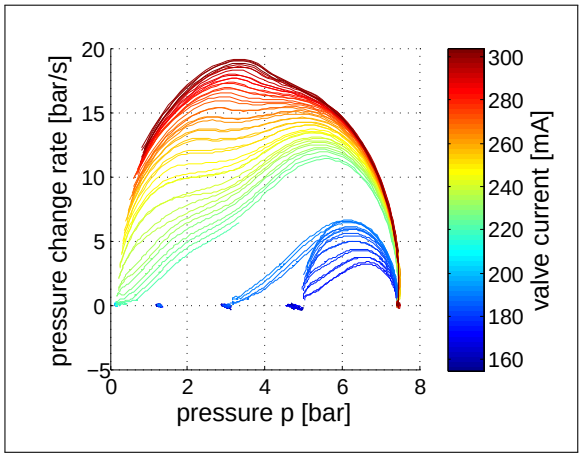

(a) Inlet phase 0.1 m

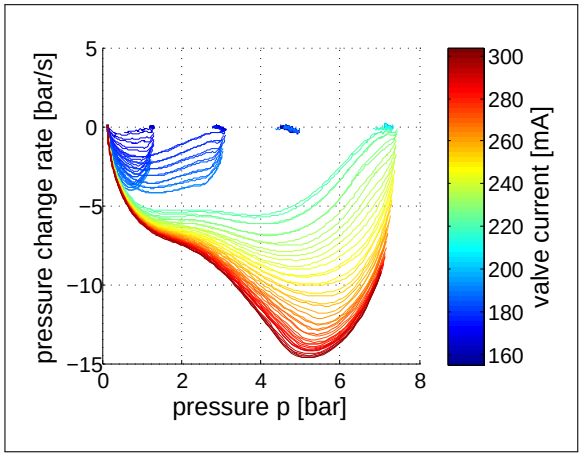

(b) Outlet phase 0.1 m

Figure 6.20: Valve phase diagrams (cf. [34, 137])

inaccuracies. It is beneficial if these lines between the valves and the PAMs are very short. Then the response time is reduced and the response behavior of the muscles is improved. In this manner, the dead volume in the pipes is diminished as well. An advantage in control performance is postulated, which has to be proved by experiments. To estimate the negative impact of longer stub tubes between valves and muscles, pressure change tests are carried out with different stub tube length. Results from the Figures 6.20(a) and 6.20(b) are taken as a reference for the tests with longer hoses. The evaluations with varying tube length (1 m - 5 m)are shown in Figure 6.21.

An integration of longer tubes allows to emulate a similar behavior as a centralized supply feed architecture approach. This can be achieved without the necessity of a modification of the robot, i.e. the positions of the valves remain the same, only the feed line length is increased. To illustrate the results obtained, Figure 6.22 compares the pressure change rates and indicates the dependencies on the lengths, which summarizes the findings of Figure 6.21.

The relative pressure change rates decrease significantly if stub tubes are elongated. Both inlet and outlet flow changes are highly dependent on the tube length, which proves the idea of keeping these lines as short as possible. The higher the pressure change rates, the better

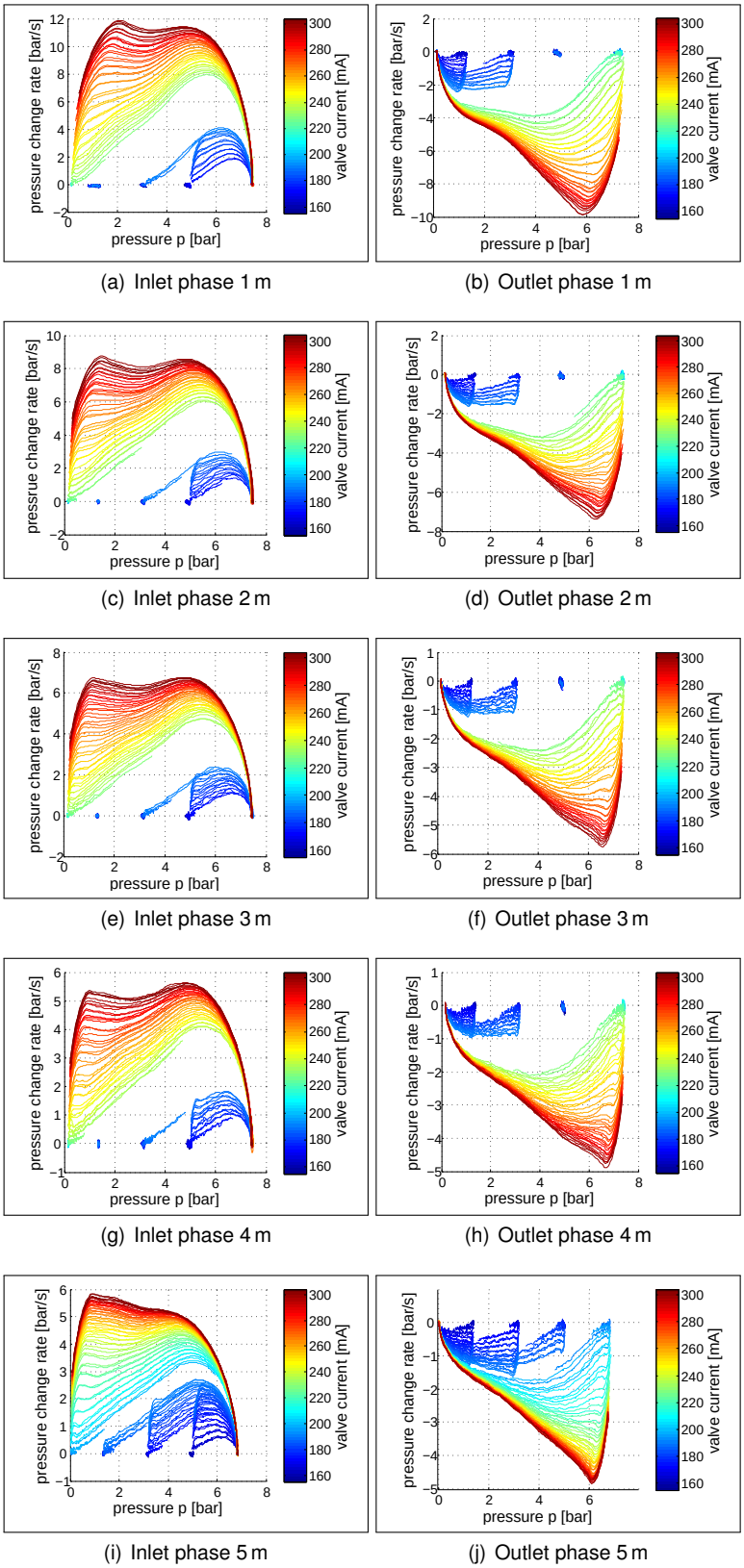

(a) Inlet phase 1 m (b) Outlet phase 1 m

(c) Inlet phase 2 m (d) Outlet phase 2 m

(e) Inlet phase 3 m (f) Outlet phase 3 m

(g) Inlet phase 4 m (h) Outlet phase 4 m

(i) Inlet phase 5 m (j) Outlet phase 5 m

Figure 6.21: Valve phase diagrams with additional tube length

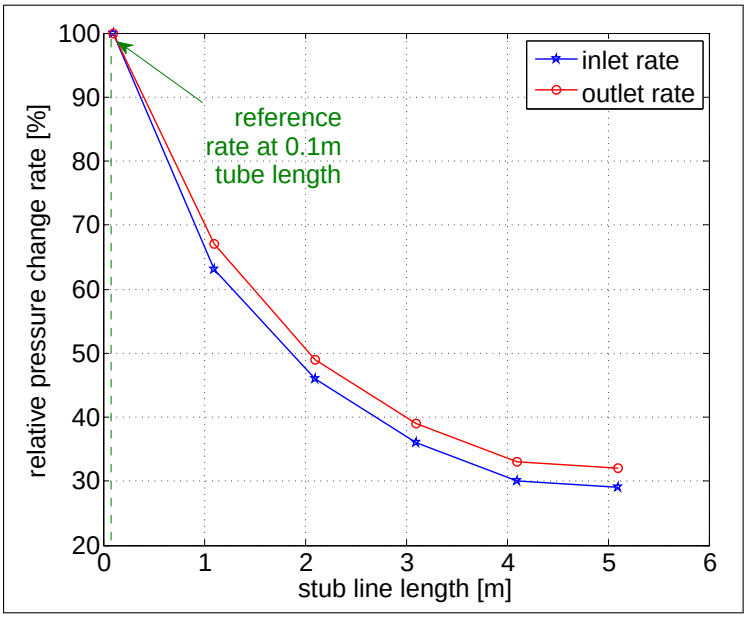

Figure 6.22: Comparison of pressure change rates

the pressure control response time, which affects the control quality. According to Figure 6.22 the decrease of the rates is extremely serious regarding elongations in the dimension of up to one or two meters. Starting from shortest stub tubes with about 0.1 m it can be estimated that even extensions in centimeter scale have strong impact on the pressure change behavior. The pressure dynamics of a pneumatic system has significant influence on its dynamic behavior and transition times within movements along given trajectories (cf. [37]).

Chapter 7

Application outlook

Section 1.1.1 shortly outlined possible application scenarios. To show the impact of the compliant mechanisms that are developed within this thesis, the next sections aim towards convincing examples from real life that could benefit from this novel technology.

The examples taken here can be classified into two main categories, scenarios with and without locomotion of the mechanism. First, robots without locomotion are considered. The examples cover various scenarios, e.g. mobile robot applications, robots for automatic vehicle refueling, and tank cleaning robots. Second, robot scenarios are presented which deal with reconnaissance in constrained spaces, e.g. pipe inspection or fire-fighting, in which the robotic mechanisms also need to have locomotion abilities.

All the scenarios below state the flexibility of the worm-like robotic mechanisms. It shall be proved that the concept of having compliant, modular and decentrally controlled robot mechanisms has crucial advantages in the disciplines demonstrated here. It is worth mentioning that some of the applications below deal with mobile robot scenarios that demand power supply on board. Power supply of the worm-like mechanisms is two-fold. Electric power is necessary to energize relevant controller boards, the valves and the sensors. This kind of power issue can be solved by using batteries, which can either be placed centrally in one specialized segment of the mechanism or they can be distributed within all segments. Fluid power is mandatory to drive the actuators. In the previous chapters, PAM actuators were chosen due to their extremely high power-to-weight ratio. However, the principle of a modular and decentrally arranged worm-like robotic mechanism based on a single fluid medium feed line can also be realized by integrating pneumatic bellows[1], pneumatic cylinders or even hydraulic cylinders. The mechanically relevant difference of the cylinders, compared to PAMs and bellows, is that the actuators are not inherently flexible, but they are rigid. Additionally, hydraulic cylinders need a hydraulic pump instead of an air compressor. Solving the power supply issue for a pneumatic system is easier than for a hydraulic system. A pneumatic system is not closed, i.e. the air of the outlet is not fed back to the system, and simply exhausts. Both pneumatic and hydraulic pumps are commercially available in small sizes, which allow on-board integration[2]. Nevertheless, the weight of these pumps increases the overall weight of the system. Within the first application shown below (cf. section 7.1), it is proven that very small-scale solutions for a supply within pneumatic systems are feasible, which are based on miniature diaphragm pumps combined with a compressed air

[1] instead of shortening and generating traction forces, bellows cause compressive forces during extension

[2] so-called miniature or micro power packs, e.g. based on diaphragm pump mechanisms

storage. Furthermore, this first application points out the advantage of limiting the fluid pressure in order to save energy, which is of interest in mobile applications.

7.1 Mobile robot application

As a first application, an enhanced embodiment of a worm-like robot is discussed, which is a continuum worm-like robotic mechanism, mounted on a tiny mobile platform, named Robotino. Robotino is an omnidirectional mobile robot by Festo AG & Co. KG, used for didactics purpose. It can carry various end-effectors, such as tool grippers. There are even extended Robotino platform versions, named Robotino XT (cf. [47]) and Robotino XXT (cf. [48]). They are equipped with a pneumatic pump, which allows to feed different implementations of the Bionic Handling Assistant, as introduced in Chapter 2 or section 2.2. A specification of the standard Robotino platform, as well as of the continuum worm-like robot arm, is highlighted in Table 7.1. Robotino is a mobile robot platform, which can reach a speed of up to 2.8 m/s, and is able to move in an omnidirectional manner. By attaching the robotic arm, its workspace can be widely enlarged. Additionally, a gripper with three fingers can be mounted on the arm, by means of which the worm-like robotic mechanism can pick items up to a payload of 0.8 kg. This gripper might even be a gripper with flexible fingers, such as the adaptive gripper DHDG with finray effect, as introduced by Festo AG & Co. KG [45]. Such grippers are built on generative manufacturing processes utilizing 3D printing machines, hence modifications are easily feasible with minimum effort. Figure 7.1 shows the entire setup, i.e. the worm-like robotic mechanism including a three-finger gripper, all mounted on a Robotino.

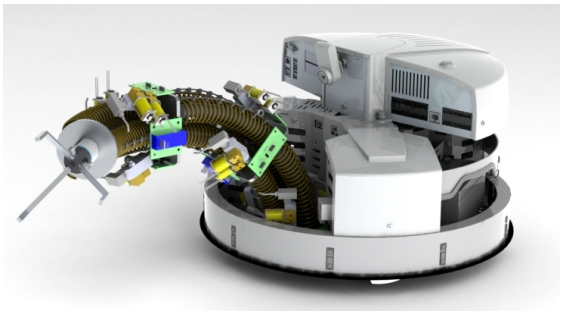

Figure 7.1: Worm-like robotic mechanism on Robotino

The worm-like robotic mechanism is based on three segments, which results in an overall length of 0.75 m (stretched). As the worm-like mechanism has a weight of 3 kg only, it can be easily carried by the Robotino platform, which has a maximum payload of up to 30 kg. Due to the lightweight construction of the robotic segments, relevant mass moments of inertia are low, which means that both translational and rotational motions of acceleration of the platform are hardly impaired. As mentioned before, the worm-like robotic mechanism for the tiny Robotino platform comprises three segments only. The entire platform has an outer diameter of about 0.45 m, and it wouldn't be reasonable to mount a very long (many segments) robot on it. So the benefits, which come from the decentral control approach together with the central feed line, are not as pronounced as in a scenario with a large scale platform and a robot utilizing a higher number of segments.

For the mobile robotics scenario as described here, an autarchic power supply for both electricity and compressed air is relevant. Robotino XT [47] already proved the feasibility of a supply on board of a mobile platform. However, the question about operating time still remains, which in the end is a matter of battery efficiency, volume and weight.

Table 7.1: Specification of Robotino platform

Feature	*Value*
Platform	
Weight	20 kg
Payload	up to 30 kg
Diameter platform	450 mm
Height platform	290 mm
Velocity	up to 2.8 m/s
Robot	
Number of continuum style robotic segments	3
weight	3 kg
Payload	0.8 kg
Length of robot arm stretched/shortened	0.75/0.63 m
Range back and forth/left and right	$\pm$240 mm
Range up and down	$\pm$60 mm
Velocity back and forth/left and right	$\pm$1.5 m/s
Velocity up and down	$\pm$0.3 m/s

7.2 Robot for automatic vehicle refueling

Automatic vehicle refueling is another application scenario, in which a compliant worm-like robotic mechanism can be of great benefit. A refueling robot replaces conventional pumps that have to be handled manually. During manual refueling several problems might occur. The human could choose the wrong type of fuel, breathes toxic fumes that escape in spite of suction mechanisms, touches the fuel nozzle that has some fuel residues (in particular, if diesel is used), or the human forgets to put in the fuel filler cap after refueling (cf. [129, 94]). Automatic refueling using a robot would overcome these issues. However, the challenge is to accurately place the pistol nozzle into the tank stub in order to prevent any damage of the car. A compliant robot is able to fulfill this task in a safe way, as the tool (pistol nozzle) is not supported absolutely rigidly, but can still move in any direction. So the tool can glide into the tank stub without high reaction forces relative to the filling opening. The compliance of the worm-like robotic mechanism might be adjusted in advance, which means that the overall forces and torques at the end-effector are limited and no damage occurs. To cover various types of vehicles (car, truck, bus etc.), the

entire setup has to be variable with respect to the dimension of these vehicles. Figure 7.2 depicts a possible arrangement of a refueling robot system, which integrates the worm-like robotic mechanism as a continuum style type within a gantry support frame. The worm-like robotic mechanism consists of an arrangement of eight segments, which results in a robotic arm with a total length of 2016 mm. To protect the system from both environmental effects and fuel, a covering has to be put on the robotic mechanism. Table 7.2 summarizes the specification of a robot of this kind.

Table 7.2: Specification of refueling robot

Feature	*Value*
Number of worm-like robotic segments	8
Weight of the hose	0.7 kg/m
Weight of the fuel inside the hose	0.3 kg/m
Weight of the fuel nozzle	2 kg
Length of the robot	2 m
Weight of the robot (incl. tool)	13 kg

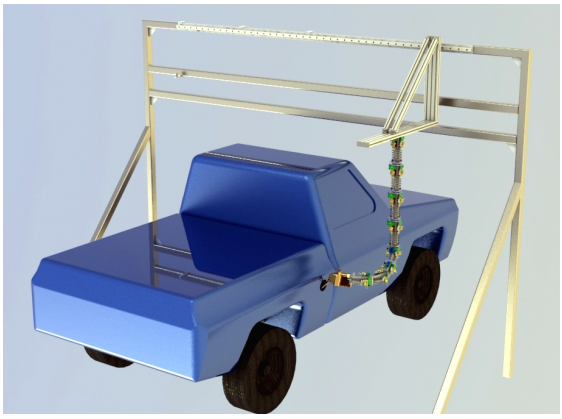

Figure 7.2: Refueling robot

7.3 Tank cleaning

Cleaning and disinfection of tanks, vessels or barrels, are necessary at regular intervals within food and drink industries. Usually these containers are difficult to access for cleaners, that's why there is a need to have adequate tools that don't have a problem with cramped conditions. Based on the fact that such cleaning scenarios are recurring, the idea of an automated system to do the job seems plausible. In the past, various cleaning tools, even robotic cleaning devices, were introduced (cf. [95] or [15] and Figure 7.3) to replace so-called cleaning-in-place systems, which utilize a fixed installed piping system with spray heads.

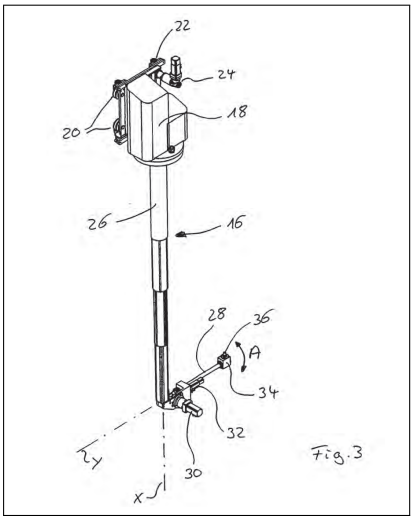

Figure 7.3: Cleaning system and cleaning process [95]

In contrast to fixed piping systems, movable robotic solutions can be used, which are flexible enough to enter containers with various geometries and restricted sizes of filling openings. The challenge is to come up with a cleaning system, in which contamination can hardly deposit. In this manner, a robotic system has to be equipped with a disinfectable or washable sleeve. At best, the robotic arm is able to clean itself. It carries a nozzle for spraying disinfectants or cleaning agents and the nozzle can reach all of the robot's sleeve. As the worm-like robotic mechanism of the continuum style type is highly flexible, advantage in this respect can be exploited. According to [95] it is helpful if the robotic arm hangs upside down from a slider that can be moved along a rail. Figure 7.4 depicts a possible prototype of such a cleaning system with a worm-like robotic mechanism. The robot is flexible to adapt to various container volumes, and the amount of necessary cleaning agents can be minimized compared to a system with rigid nozzle or piping setup.

Figure 7.4: Tank cleaning scenario

Table 7.3 presents specifics about the prototype as introduced here. It shows the summary of features that the worm-like robotic mechanism should have for this kind of application scenario.

Table 7.3: Specification of tank cleaning robot

Feature	*Value*
Number of worm-like robotic segments	12
Weight of the cleaning nozzle	3 kg
Length of the robot	3 m
Weight of the robot (incl. tool)	20 kg

7.4 Fire-fighting robot

As the worm-like robotic mechanism is able to bend flexibly, it is suitable for operations in confined spaces. One possible application might be fire-fighting, which is a scenario that deals with such confined spaces. The robot would use a fire hose as a support structure, which is moved and curved by means of fluid actuators. Hose sizes vary according to their concrete application (indoor or outdoor fire etc.), that's why scalable robotic systems are necessary to meet these adaption demands. The benefits of using such a fire-fighting robot are manifold, and various systems have already been developed (cf. [147]). Such a robotic system is equipped with an adequate protective sheathing or self-cooling mechanism. It can work inside areas that are too hazardous for firemen. In this regard, a robot is able to access sources of fire very closely and the fighting precision increases, which means that less extinguishing water is necessary and less damage is caused by water. In the following example, a realistic fire-fighting scenario shall be discussed, which follows the concept of a discrete prototype of the worm-like robotic mechanism (cf. 3.3).

In Germany and Austria, hose sizes of so-called type C and B with inner diameters of 42 mm and 75 mm are quite common for fire-fighting.[3] Hoses with up to 150 mm are available for special applications. The aforementioned hoses can be filled with different amounts of water: 1.4 L/m, 4.4 L/m and 17.7 L/m. The load on these hoses varies extremely if one considers that 1 L of water has a weight of about 1 kg. In average, standard hoses have a weight of approximately 0.5 kg/m (without water). Jet pipe nozzles or hollow stream nozzles (cf. [23] or [24]) generate an additional payload of about 2 kg. Important within these considerations is the reaction force of this nozzle when water comes out. In order to get an estimation of this force, the following empirical formula[4] can be used:

$$F_{reaction} = 0.22563 * volumetricflow * \sqrt{nozzlepressure} \quad . \tag{7.1}$$

The units used are l/min[5] for the volumetric flow and bar for nozzle pressure. In this manner, the maximum nozzle pressure as well as the volumetric flow of the system have to be taken into account. The assumptions of Table 7.4 are set as boundary conditions in order to result in adequate specifications for a fire-fighting robot.

Figure 7.5 represents an example of a construction based on the aforementioned assumptions. The system is designed with an overall diameter of about 330 mm, and the segment length is

[3] according to DIN 14811 Class 1, [22]

[4] cf. url: http://www.firetactics.com/NOZZLE-REACTION.htm; last accessed: December 9, 2013

[5] litres per minute

Table 7.4: Assumptions for fire-fighting scenario

Feature	*Value*
Hose type C	42 mm inner diameter
Weight of the hose	0.5 kg/m
Weight of the water inside the hose	1.4 kg/m
Weight of the hollow stream nozzle	2 kg
Maximum operating pressure	17 bar
Maximum volumetric flow	500 L/min
Reaction force	465 N
Range of the robot (freestanding)	5 m

approximately 260 mm. Each segment is actuated by a set of four antagonistically arranged hydraulic cylinders. The use of pneumatic cylinders or artificial muscles is not advisable here. Extremely large sizes of components would be necessary to handle very high forces. For this reason, hydraulic cylinders should be chosen, as these actuators have a very good force-to-dimension ratio (cf. Figure 2.3 from subsection 2.1.2). To actuate the hydraulic system, the hydraulic pump of the fire engine could be used, which is usually available for driving tools, such as spreaders. The robot has to work in a hazardous environment with extreme heat, so it is beneficial to use fire-resistant hydraulic fluid, and to equip the entire mechanism with a protective covering. Instead of hydraulic oil, even water could be used, but in this case it must be ensured that all of the components, in particular the valves, work flawlessly without corrosion problems. Additionally, a shield based on water spray mist can help to keep the mechanism cool enough to prevent the actuators and electronics inside the robot from damage. [90] introduces a robot with water used as hydraulic and cooling medium, following the aforementioned design aspects. Furthermore, sensors such as temperature sensor, gas sensor for detection of toxic gases, or flame sensors[6] can be attached to the robotic system. This enables sensitivity with respect to certain environmental conditions.

Another crucial aspect of a robot of this kind is locomotion. A long fire hose mechanism using powerful hydraulic cylinders leads to a high overall weight. For reasonable usage of the robot, it has to meet the demand of moving itself within a hazardous and constrained environment. There are different ways to implement locomotion strategies. [150] and [91] introduce some strategies, but one very simple solution is the generation of waveforms that are carried out by all of the segments. Two perpendicular waveforms can be used to move the system in a snake-like manner (cf. [107]), three waveforms even allow worm-like motions (cf. [115]).

7.5 Reconnaissance in constrained spaces

A further application scenario, in which the benefits of the flexible robotic mechanism come to bear, is reconnaissance in constrained spaces. For instance, constrained spaces could be

[6] e.g. Hamamatsu flame sensor type R2868

(a) Fire-fighting robot

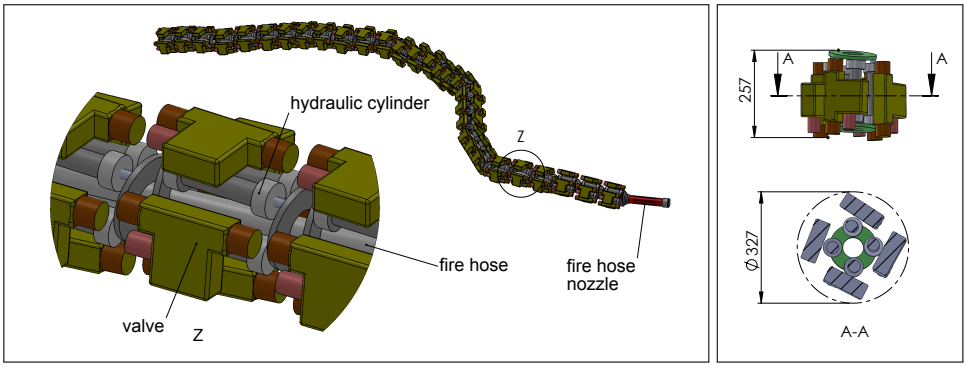

(b) Robot model (c) Robot segment model

Figure 7.5: Fire-fighting robot application

either pipework within industrial plants or areas of disasters, such as an earthquake or nuclear accidents. These scenarios demand reconnaissance instruments in order to inspect objects (pipework, reactor components) or search for buried objects and persons. Different approaches are known from prior art, e.g. wheeled snake-like robots [87] and miniature robots that can be thrown [163]. The control of these robots can be implemented in an autonomous or teleoperated manner [164], e.g. using a joystick as shown in [165].

The continuum worm-like robotic mechanism with its compliant actuators and flexible segments can be utilized as a reconnaissance system that works in a worm-like or snake-like manner. To act as a reconnaissance instrument, the robot has to be equipped with additional sensors, such as optical sensors (e.g. camera) or acoustic sensors (e.g. ultrasonic sensors). Temperature sensors or gas sensors etc., as mentioned in the previous section 7.4, allow further sensitivity with respect to specific scenario conditions.

Similar to the applications in section 7.1, independent energy supply for compressed air and electrical current is of essential significance. Two different kinds of on-board power supply are feasible: (a) central supply at the end of the robotic system or (b) distributed power supply units attached to each of the robot's segments. A distributed system has the benefit that the mechanical and electrical modularity of the system remains (cf. [107]).

Figure 7.6 considers a possible embodiment of a reconnaissance worm-like robotic mechanism, which is composed of 12 modular continuum style segments, similar to a system as

introduced in 7.3. Depending on the concrete application scenario, it can be helpful to integrate suction cups or passive wheels to enhance maneuverability. Furthermore, the system has to be equipped with a protective sleeve, which meets the application-specific demands, such as ex-protection or washability.

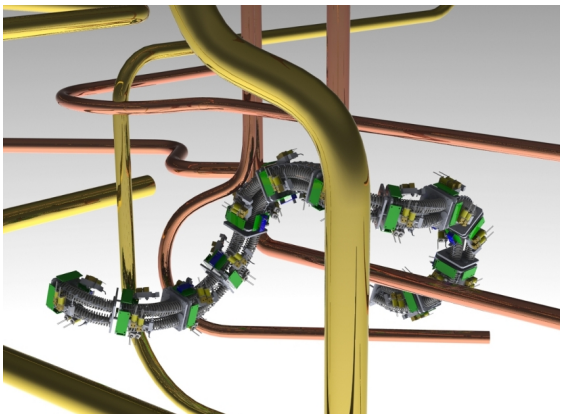

Figure 7.6: Pipe inspection scenario

Chapter 8

Conclusions and future work

The final chapter of this thesis gives the review of all the previous chapters, in particular with respect to the Chapters 3 and 6. First, a summary is presented about the main idea, the novelty and the benefit of the approach. Second, the future work is outlined, taking Chapter 7 into consideration. This second part provides straightforward clues towards further development, and also shows future visions, which intend to motivate for new robot designs based on the approach.

Conventional fluid or pneumatic robotic mechanisms are based on central medium supply, i.e. valves and driving electronics are located within a common basis of the mechanism. This typical setup causes difficulties in the case that the robotic mechanism is composed of a large number of links. In contrast, fluid robots can be designed in a way such that the entire robot becomes a modular and slim mechanism even if very many modules are assembled to a long robotic mechanism. The idea of this thesis is to prove the concept of such decentralized modular fluid mechanisms that have one central supply line, which means that there is no need for numerous parallel supply tubes that would limit the overall magnitude of the mechanism.

Two different kinds of worm-like or serpentine mechanisms were realized as prototypes. The construction of a first prototype utilizes a stiff support structure for the segments, which are connected to their neighbors with cardan joints, whereas the second prototype has a completely flexible structure with a stiff coupling between neighboring units. Both variants are equipped with pneumatic driving means, more specifically with pneumatic artificial muscles. These driving elements are inspired by biomechanics concepts, and as a matter of principle these actuators are lightweight, compliant and very efficient. Hence, both prototypes result in flexible robotic mechanisms with the fundamental advantage of being inherently compliant. This is of particular interest in the world of robotics, as compliance is extremely relevant in service robotics domains and the like. Thus, the system is ready to deal with safety requirements and upcoming norms (cf. 1.1.2) that are relevant during collaboration modes between humans and robots. Utilizing lightweight actuators and construction, which also affect the mass moment of inertia, leads to a weight of 1.2 kg per segment (case of the discrete prototype) and 1.0 kg (case of the continuous prototype). This again has positive influence on safety issues as the energy (both kinetic and potential energy) necessary to drive the system gets low. The driving elements are controlled by pressure, and different stiffness and forces can be generated with the system. Switching from a position control mode to a force control mode would be even possible without an additional integration of force or force-torque sensors. Consequently, safety issues that simultaneously

deal with force/torque issues, can be addressed without much effort.

Additionally to the benefits related to compliance and modularity, the presented approach comes with another main advantage, which is the extremely short distance between actuating means and valves. Due to these short supply tubes, which can only be short if both valves and actuators are placed on board of each robotic segment, the fluid medium does not have to pass long access channels in order to reach the actuators. As a consequence, the control of such segments is very direct, in the sense that there is hardly any dead volume in between, which could harm the control performance. This benefit becomes more dominant the more segments are integrated in the worm-like mechanism. Conventional fluid robots make use of bunches of supply lines to feed the actuators from a common basement, in which also the valve cluster is located. As soon as the robot becomes longer, these tubes are growing, i.e. dead volume increases and actuator reaction time gets worse. Furthermore, construction volume enlarges if the number of robotic segments aggrandizes, which is due to the high number of parallel tubes that are necessary to connect the actuators with the centralized valve cluster.

Both prototypes, discrete and continuum worm-like prototypes, allow soft robotic motions. However, the workspace of the discrete setup is limited by the angular range of each axis of one cardan joint, which is only $\pm 16^\circ$. As mentioned in Chapter 4 or Figure 4.8 and Figure 4.9, this angle is influenced by the length of the actuator, its diameter and the lever arm. If one considers stronger muscle types, such as the Festo DMSP-20 or DMSP-40, or even longer actuators, e.g. 300 mm instead of 160 mm as used here, joint angles of up to $\pm 45^\circ$ would be possible. In the continuous case, each segment can bend $\pm 30^\circ$, and the shape of each module is similar to a torus segment. Thus, the continuum style version is able to move in a serpentine-like manner. It has one additional DOF compared to the discrete prototype, which allows to shorten or extend in a longitudinal direction. In contrast, the discrete setup can only rotationally move about the cardan joints. As the mechanisms are arranged in a consistently modular way, it is very easy to extend an existing system without adaptation effort related to mechanics or software. Furthermore, the length, diameter or the type of each of the actuators can be modified according to the needs for specific applications. In this respect, the system becomes scalable in terms of size, workspace and payload. However, there are certain limits regarding size, as technical components, in particular valves, are not available in arbitrary dimensions. Considering self-supporting structures the units close to the basement have to carry higher loads, and the question arises if a completely modular setup with equal segments is reasonable for a specific application. In general, such completely modular self-supporting mechanisms are oversized at the manipulator tip and insufficiently sized at the base. Though, the problem of unequal loads doesn't exist for mechanisms that move on the floor only. For instance, serpentine mechanisms can be built as entirely modular structures.

This thesis introduced the concept of modular pneumatic mechanisms, worm-like robots with decentralized control architecture utilizing centralized power supply. Two different prototypes of such worm-like robots were developed. It was shown that the concept can be realized with different kinds of robots based on pneumatic artificial muscle actuators, which are known to be extremely lightweight and efficient. Both of the presented mechanisms are inherently compliant, which is of great benefit if it comes to applications where humans are in the loop. Limits of the prototypes, in particular in terms of payloads (1.2 kg for the presented mechanisms) and workspace were determined. However, it can be stated that these limits can be influenced to some extent. Consequently, by use of different geometries, larger actuators or even pneumatic or hydraulic cylinders instead of pneumatic muscles, these boundaries can be shifted. It should

be mentioned that the choice of either pneumatic or hydraulic actuators is a fluent passage, but in general hydraulic systems are more suitable for applications with high payloads and long self-supporting mechanisms, e.g. as presented in the fire-fighting robot scenario in section 7.4. A robotic arm driven by artificial muscles, having a reach of 2000 mm and a payload of 5 kg, as introduced in section 2.2 [39], is one of the largest lightweight pneumatic robot systems. As soon as both payload and reach or robot length increase, it is reasonable to select hydraulic actuators.

The thesis could already show two different prototypes of worm-like mechanisms to prove the feasibility of a modular and decentrally arranged pneumatic control approach. Current limitations, in particular in terms of size, payloads and suitability for specific application scenarios, can be addressed with diverse follow-up developments and extensions. Various directions of future work are possible, the most promising ones are covered in the following.

Present generative manufacturing techniques by means of rapid prototyping machines offer many options with respect to part design and implementation of functionality. For instance, the idea to build fluid or pneumatic actuators using such printers was already realized in the past. Both single-acting bellows [63, 103] and double-acting bellow constructions [76] can be generatively manufactured. The advantage of such rapid prototyping techniques is that there can be an extremely high integration of supporting structure of the robot and actuation means within a single part. In such a way, robot arms, such as the Bionic Handling Assistant by Festo AG & Co. KG, can be created [49]. Lightweight actuators, as presented in [44] or [102], aim towards this integration. In this respect, modern 3D printing machines offer new options and allow to print different materials within one printing process. Today even rubber-like material can be printed, which means that stiff and flexible materials can be combined for parts in order to adjust the compliance or movement abilities in a precise way. Bellows or cushions in various dimensions can be manufactured, which leads to unprecedented possibilities in robot construction.

Besides fluid actuators, one might also consider the valve as interesting parts to be manufactured based on printing technologies. Same is with hardware devices, i.e. printed circuit boards. Within the last few years, efforts were made in the direction of 3D printing of such devices, which is known under the term *liquidmetal*. Apple Inc., USA, already filed several patents in the domain of *liquidmetal* printing [122, 123]. These technologies might open up completely new applications, as the integration of electronics and valves is one of the key issues within the construction of worm-like mechanisms, as presented in this thesis and also in robotic construction in general. Additionally to the progress of 3D printing technologies, also piezoelectric valve technologies are more and more common (e.g. [120]). Valves are getting smaller and smaller, which makes it easier to result in a slimline and lightweight construction. Another relevant aspect is the cost-effectiveness of all components of the mechanisms, in particular actuator and supporting frame costs. 3D printing of robot components could help to build cheap mechanisms. To take it even further, one might think about disposable robots, on condition that the cost-performance ratio is high enough. Examples in robotics research prove that such cheap robots are already relevant [162].

In addition to the movements of robotic segments within a mechanism, the locomotion of the entire mechanism is a crucial topic as well. It becomes very interesting if one aims towards applications, in which the reachable workspace is so large that a robot fixed on a static basement is not suitable any longer. Also this is the case whenever mobile robotic platforms have problems to maneuver properly, such as in difficult terrains. For this purpose, locomotion strategies are of great significance. In the field of research, many different serpentine and worm-like robots have

been developed. Modular robots, such as [166], serpentine robots [100] or hyper-redundant serpentine robots [101], were studied. Even 3D joint serpentine robots [96] were introduced, which have more flexibility in maneuverability. Most of these mechanisms are actuated using electric drives, but also pneumatically driven systems exist [53].

Furthermore it shall be mentioned that the two robotic prototypes presented in this work might be modified in terms of joint and actuator technology. Compared to what was shown in Chapter 3, both prismatic joints or rotary joints could be arranged together, leading to more flexible kinematics. For this purpose, even bellows or other actuator technologies, such as electrostrictive polymer artificial muscle actuators [84], might be interesting. Depending on the concrete application scenario, these joints or links have to be equipped with a protective enclosure, such as a neoprene skin, expansion bellows or the like. This way, scenarios that demand washability, food-safety or explosion protection might be taken up.

Last but not least, as far as the control strategy is concerned, recent advances in alternative control techniques, such as the morphological computation approach [119, 121], could help to improve and simplify the control implementation of the worm-like mechanisms presented here. As it was shown, dealing with the nonlinear and compliant behavior of these high-dimensional robotic structures is a challenge. Instead of finding a workaround for these issues, the idea of morphological computation is to use them as a computational resource [59]. The robotic hardware structure itself contributes to the computation within the control of the system, which is a concept similar to reservoir computing [13, 135, 154]. Simulations could even prove the realization of such a morphological computation with feedback [60]. In particular, if it comes to worm-like mechanisms with a high number of segments, the integration of the morphological computation approach within future setups might be a promising means to deal with complex and mechanically flexible systems.

Appendix A

Related documents

Additionally to what was presented in the previous Chapters 3, 5, and 6, further relevant information is embedded in the following sections. The documents below complement the contents of the aforementioned chapters, presenting more in-depth analyses that support the statements within the thesis text.

In the following sections, supplementary tables that sum up the acquisition cost for the robotic setup and the masses of all components, as well as several muscle calibration plots and movement experiment figures are given. These documents enhance the main documents included in the thesis.

A.1 Acquisition cost for setup

As an extension to what was already mentioned in section 3.7 within Chapter 3, all costs for the components that are necessary to build up either a discrete or a continuum worm-like robotic mechanism are listed in Table A.1. It becomes clear that the valves cause the highest costs since the price of each of them is around 60 Euro and two of them are necessary for one actuator (i.e. 24 in total as in the robotic embodiments described in this thesis). Also the pressure sensors are rather cost-intensive, as sensors with industrial quality and housing are utilized. Significant savings are possible here. Last but not least, the muscle actuators cause major costs, which of course depend on the number of degrees of freedom. In the cases concerned, 12 actuators are installed, which result in total costs of 840 Euro. If one considers savings regarding the pressure sensors, the overall costs of around 4300 Euro for the discrete and 4400 Euro for the continuous robot can be reduced. Also costs for the mechanical backbone, which is currently mainly based on aluminum and steel parts, might be brought down if 3D printing technologies are extended to these components. In general there could be savings derived from a high degree of integration that is possible if 3D printing techniques are used for manufacturing of actuators (e.g. bellows etc.) within future developments.

Regarding masses of both the discrete and the continuum worm-like robotic mechanism, Table A.2 reveals a complete assembly of individual weights of all components, which were already referenced in subsection 3.6.7.

Table A.1: Acquisition cost for setup

Component	*Type designation*	*Quantity*	*Unit prize*	*Lump sum prize*
Valves	Parker MDPRO	24	60 Euro	1440 Euro
Pressure sensors	SMC PSE-510-M5-Q	12	100 Euro	1200 Euro
PAM	Festo DMSP-10-160N-RM-CM	12	70 Euro	840 Euro
3D printed plastics parts	*customized*	n/a	n/a	200 Euro
Pressure controllers	*customized*	12	10 Euro	120 Euro
Pneumatic fittings	diverse	n/a	n/a	50 Euro
Power supply	PC power supply	1	20 Euro	20 Euro
Consumables	diverse	n/a	n/a	50 Euro
Components for discrete robot type only:				
Aluminum supporting structure	*customized*	1	300 Euro	300 Euro
Segment main controllers	Arduino Nano V3.0 ATmega328P-AU	3	12 Euro	36 Euro
Angle sensors	ams AS5145H	6	5 Euro	30 Euro
Diametric magnets	Arnold Magnetics AS5000-MD6H-1	6	1 Euro	6 Euro
Sum – discrete robot				**4292 Euro**
Components for continuum robot type only:				
Aluminum supporting structure	*customized*	1	150 Euro	150 Euro
Stretch sensors	Images Scientific Instruments Inc. Stretch Sensor	12	12 Euro	144 Euro
Segment main controllers	Teensy 3.1 MK20DX256VLH7 Cortex-M4	4	25 Euro	100 Euro
Compression springs	standard 30x2,7x10 spring steel	12	7 Euro	84 Euro
Gyroscope and acceleration sensor	MPU6050 breakout	4	10 Euro	40 Euro
Sum – continuous robot				**4438 Euro**

Table A.2: Masses of components

Component	*Mass – discrete*	*Mass – continuous*
Control electronics		
Arduino board / Teensy board	6 g	5 g
Arduino/Teensy shuttle board	8 g	8 g
Pressure controller board	12 g	12 g
Actuators and sensors		
Valve	63 g	63 g
Pressure sensor PSE510	10 g	10 g
Angle sensor board / stretch sensor	2 g	2 g
Muscles DMSP-10-160-RM-CM incl. connectors	85 g	85 g
Mechanics		
Rotary encoder connector	12 g	—
Pressure controller connector	2 g	—
Bell half-shell	33 g	—
Cardan joint	48 g	—
Aluminum block air cluster	14 g	—
Disc 1/2 / plate	115 g/101 g	103 g
Rod 1/2/3/4 / spring	84/103/103/22 g	83 g
Valve connector half-shell / cluster	7 g	27 g
Muscle U-connector	8 g	—
Muscle end connector POM DMSP10	2.8 g	—
Arduino board connector for segment 3 half-shell /Teensy board connector	8 g	—
Fitting straight M5	4.8 g	4.8 g
Fitting Y	8.3 g	8.3 g
Fitting T DMSP10 (Festo QSMTL-G1/8-6)	11.1 g	11.1 g
Chain element	3.7 g	—
PU tube (per meter)	19.6 g	19.6 g
Calibration tube	26.2 g	26.2 g
Calibration weight connector	151.4 g	151.4 g
Calibration connector	71.1 g	71.1 g

A.2 Muscle characteristics

In order to complement the muscle characteristics plots from section 5.2, which only show triangular surface plots of muscles one to six, characteristics for the remaining muscles seven to twelve based on the muscle calibration procedure are depicted in Figure A.1.

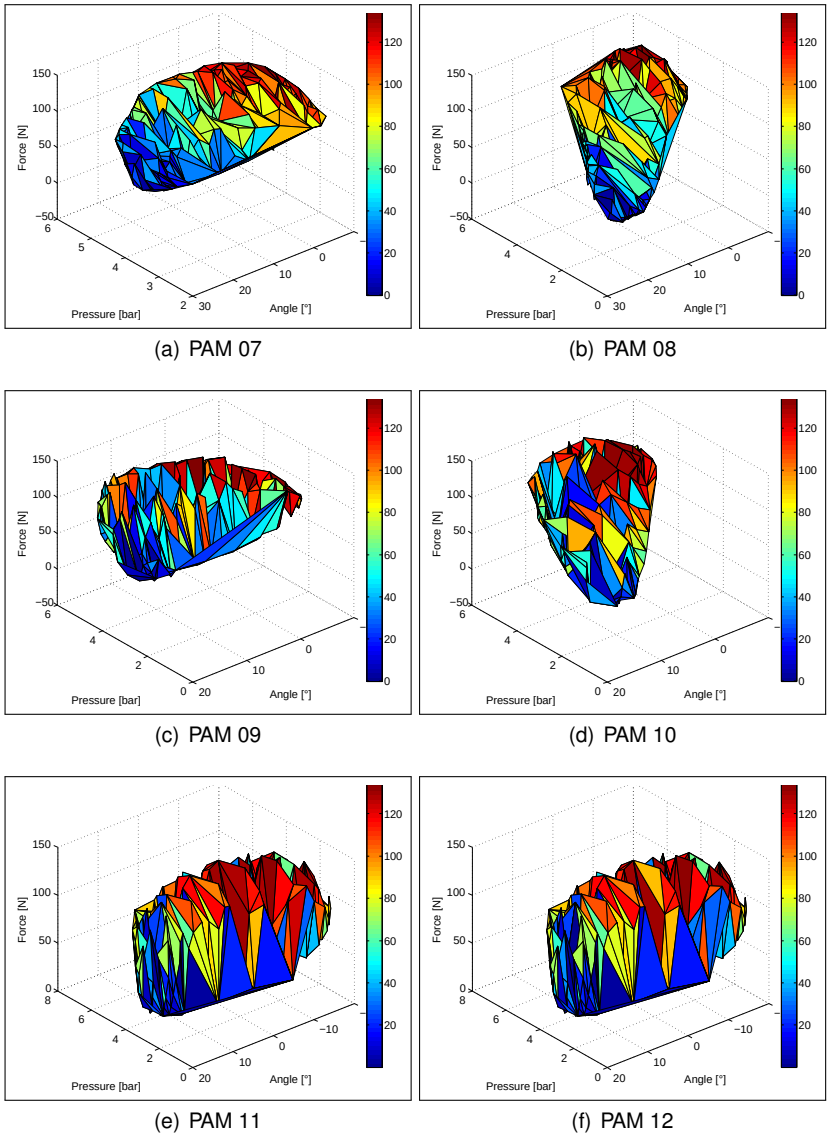

(a) PAM 07 (b) PAM 08

(c) PAM 09 (d) PAM 10

(e) PAM 11 (f) PAM 12

Figure A.1: Muscle characteristics (II)

A.3 Movement tests

In addition to the experimental results shown in Chapter 6, further movement test plots are illustrated in the following.

For the discrete worm-like robotic mechanism case based on three modular segments, movement tests according to subsection 6.1.2 were conducted. Closed loop results were mentioned in subsection 6.1.2, open loop and triple speed (3 °/s) experimental outcomes are provided in Figure A.2 and Figure A.3. Movement diagrams with long tubes (3 m in length), carried out at triple speed as well, are shown in Figure A.4, which are a continuation of the plots of subsection 6.1.3.

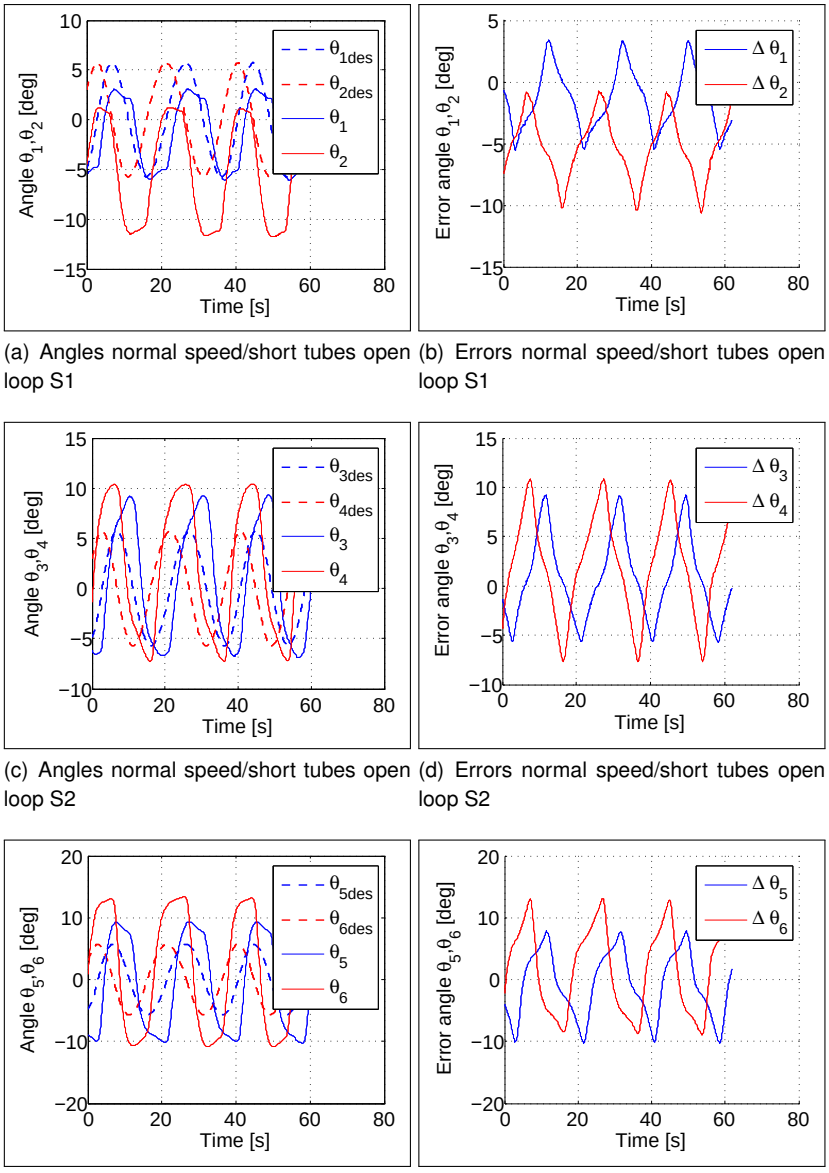

(a) Angles normal speed/short tubes open loop S1

(b) Errors normal speed/short tubes open loop S1

(c) Angles normal speed/short tubes open loop S2

(d) Errors normal speed/short tubes open loop S2

(e) Angles normal speed/short tubes open loop S3

(f) Errors normal speed/short tubes open loop S3

Figure A.2: Movement diagrams open loop

For the continuum worm-like robotic mechanism case, supplementary to the position, velocity and acceleration tests of one segment as already highlighted in subsection 6.2.1, experiments in order to determine the angles (azimuth, elevation, roll), angular velocities and accelerations shall be shown in what follows (cf. Figure A.5).

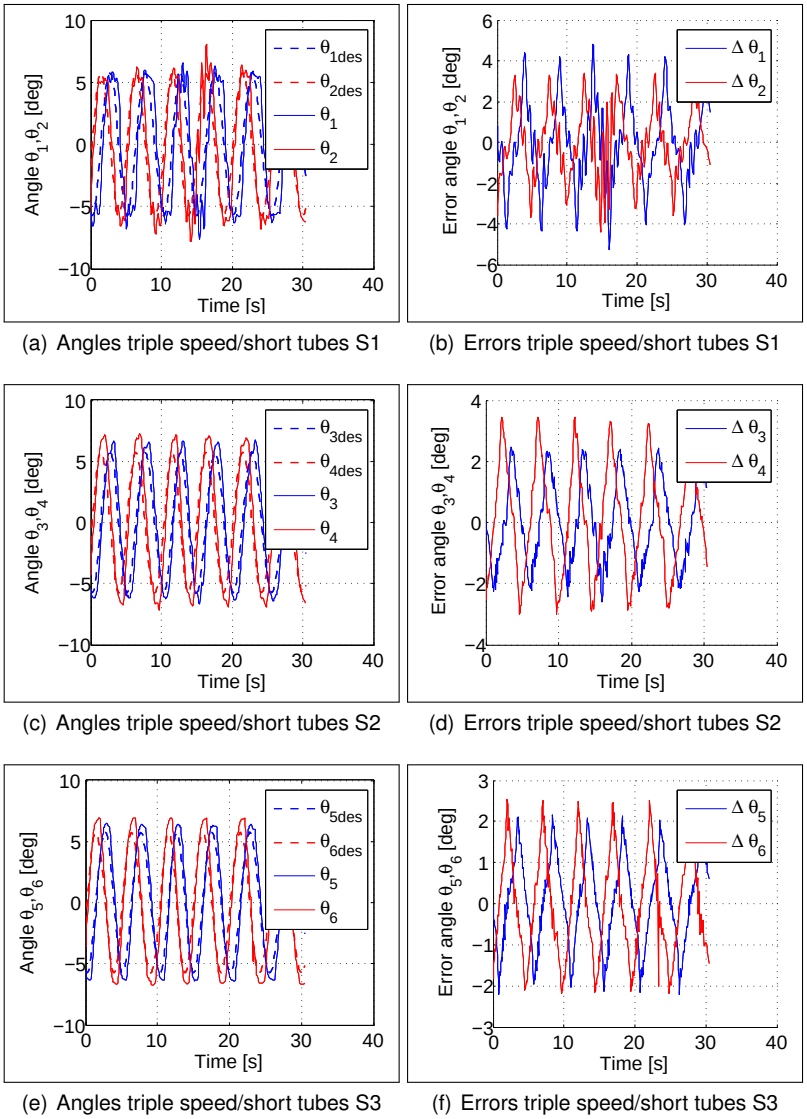

(a) Angles triple speed/short tubes S1 (b) Errors triple speed/short tubes S1

(c) Angles triple speed/short tubes S2 (d) Errors triple speed/short tubes S2

(e) Angles triple speed/short tubes S3 (f) Errors triple speed/short tubes S3

Figure A.3: Movement diagrams at triple speed

The same experiments are carried out with a set of four continuum style segments, which contribute to the tests within subsection 6.2.2 (cf. Figure A.6).

Furthermore, position control measurements are considered for the one-segment tests (cf. subsection 6.2.1). Additional open loop experiments with stretch sensor recording are investigated below. Different movements, such as right and left, up and down, circular, and randomized are included (cf. Figures A.7, A.8, A.9 and A.10).

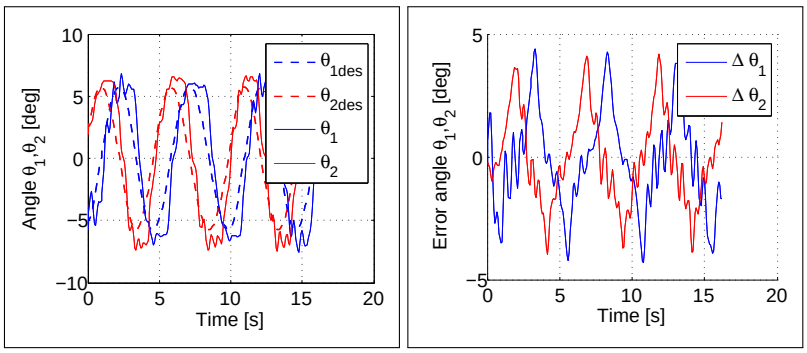

(a) Angles triple speed/3 m tubes S1 (b) Errors triple speed/3 m tubes S1

(c) Angles triple speed/3 m tubes S2 (d) Errors triple speed/3 m tubes S2

(e) Angles triple speed/3 m tubes S3 (f) Errors triple speed/3 m tubes S3

Figure A.4: Movement diagrams with long tubes at triple speed

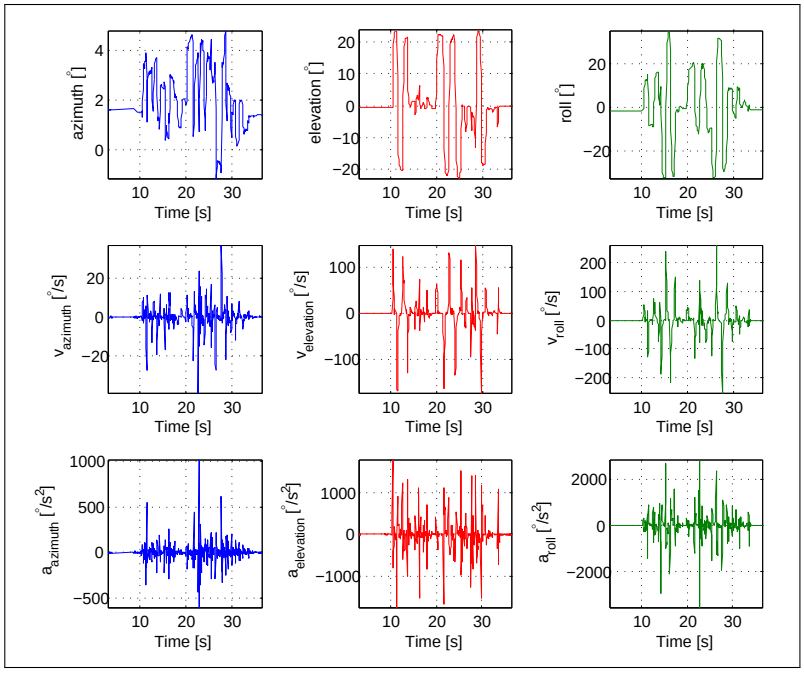

Figure A.5: Angle, rotational velocity and acceleration tests with one segment – continuum case

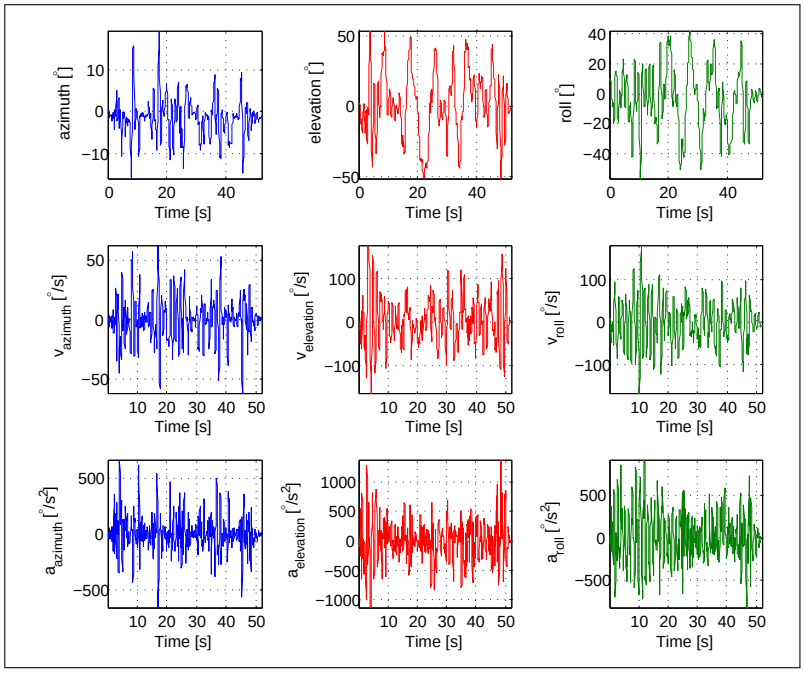

Figure A.6: Angle, rotational velocity and acceleration tests with four segments – continuum case (cf. [33])

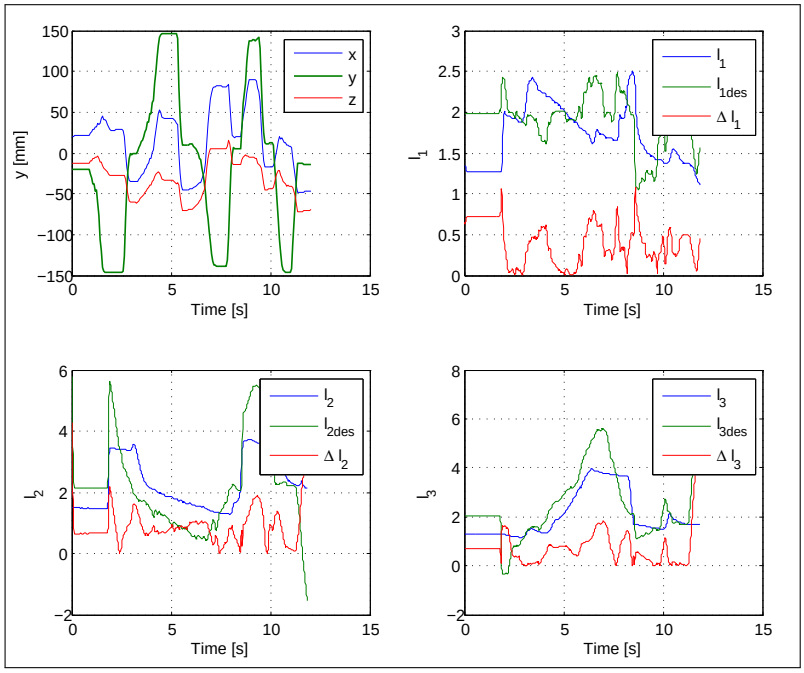

Figure A.7: Open loop right and left movement of one segment – continuum case

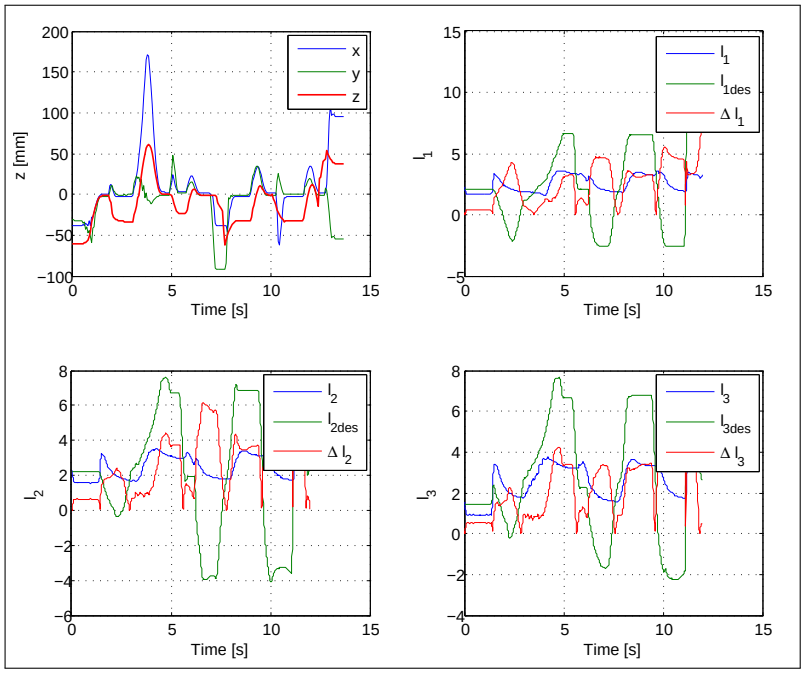

Figure A.8: Open loop up and down movement of one segment – continuum case

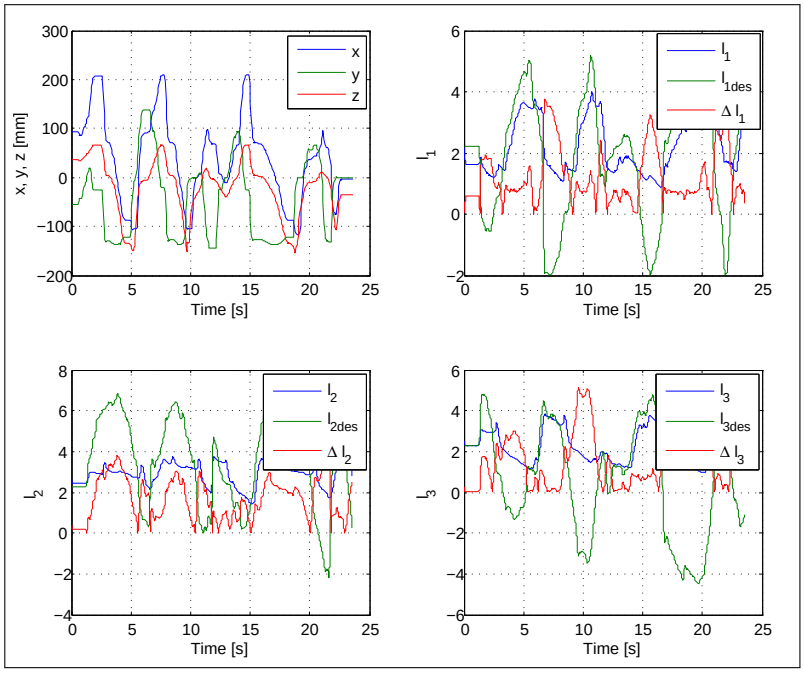

Figure A.9: Open loop circular movement of one segment – continuum case

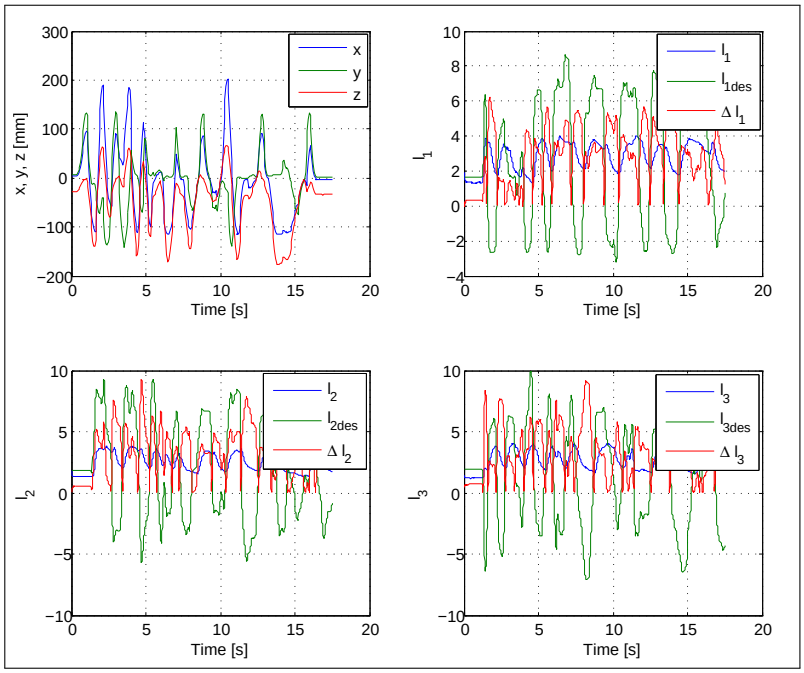

Figure A.10: Open loop randomized movement of one segment – continuum case

References

[1] A. Albu-Schäffer, C. Ott, U. Frese, and G. Hirzinger. Cartesian impedance control of redundant robots: recent results with the DLR-light-weight-arms. In *Robotics and Automation, 2003. Proceedings. ICRA '03. IEEE International Conference on*, volume 3, pages 3704–3709, September 2003. 8

[2] A. Albu-Schäffer, C. Ott, U. Hagn, and T. Ortmaier. Method for controlling a robot arm, and robot for implementing the method. Patent, 2010. US7,646,161B2. 20

[3] T. Aoki, A. Ochiai, and S. Hirose. Study on slime robot: development of the mobile robot prototype model using bridle bellows. In *Robotics and Automation, 2004. Proceedings. ICRA '04. 2004 IEEE International Conference on*, volume 3, pages 2808–2813, April 2004. 23

[4] T. Aoki, H. Ohno, and S. Hirose. Design of Slim Slime Robot II (SSR-II) with Bridle Bellows. In *Intelligent Robots and Systems, 2002. IEEE/RSJ International Conference on*, volume 1, pages 835–840, 2002. 23

[5] A. Baldwin. Realizable models of muscle function. In *First Rock Biomechanics Symposium. Proceedings*, pages 139–148, New York, April 1969. Plenum Press. 18

[6] A. Barber. *Pneumatic Handbook*. Elsevier Science, Amsterdam, 1997. ISBN 9781856172493. 13

[7] A. Bartow, A. Kapadia, and I. D. Walker. A contractor muscle based continuum trunk robot. *International Journal of Systems Applications, Engineering & Development*, 8:198–206, 2014. 24

[8] D. Bergemann, B. Lorenz, and A. Thallemer. Actuating means. Patent, 2002. US6349746B1. 19

[9] T. Beullens. Hydraulic or pneumatic drive device. Patent Application, 1989. US4841845A. 18

[10] R. Bischoff, J. Kurth, G. Schreiber, R. Köppe, A. Albu-Schäffer, A. Beyer, O. Eiberger, S. Haddadin, A. Stemmer, G. Grunwald, and G. Hirzinger. The KUKA-DLR Lightweight Robot arm – a new reference platform for robotics research and manufacturing. In *Robotics (ISR), 2010 41st International Symposium on and 2010 6th German Conference on Robotics (ROBOTIK)*, pages 1–8. VDE Verlag, 2010. ISBN 9783800732739. 7

[11] G. Butter (KUKA Aktiengesellschaft, Public Relations). Premiere for the LBR iiwa - KUKA exhibit at Hanover Fair both innovative and visionary. http://www.kuka-ag.de/NR/rdonlyres/B489826D-85E0-499C-96D9-14A21B0D7253/17959/presseinfo_130325_en.pdf, March 2013. [Online; press release, accessed December 12, 2013]. 20

[12] M. Calisti, M. Giorelli, G. Levy, B. Mazzolai, B. Hochner, C. Laschi, and P. Dario. An octopus-bioinspired solution to movement and manipulation for soft robots. *Bioinspiration & Biomimetics*, 6(3):036002, 2011. 23

[13] K. Caluwaerts, M. D'Haene, D. Verstraeten, and B. Schrauwen. Locomotion without a brain: physical reservoir computing in tensegrity structures. *Artificial Life*, 19(1), 2013. 136

[14] C.-P. Chou and B. Hannaford. Measurement and modeling of McKibben pneumatic artificial muscles. *Robotics and Automation, IEEE Transactions on*, 12(1):90–102, 1996. 82

[15] L. Clusserath and U. Grunewald. Multi-functional cleaning robot. Patent Application, 2013. US2013/0174880A1. 126

[16] P. Corcoran. Two Wires and 30 Years : A Tribute and Introductory Tutorial to the I2C Two-Wire Bus. *Consumer Electronics Magazine, IEEE*, 2(3):30–36, 2013. 93

[17] P. Corke. *Robotics, Vision and Control – Fundamental Algorithms in MATLAB*, volume 73 of *Springer Tracts in Advanced Robotics*. Springer, 2011. ISBN 9783642201431. 67

[18] J. Craig. *Introduction to Robotics: Mechanics and Control*. Addison-Wesley series in electrical and computer engineering: Control engineering. Addison-Wesley, 1989. ISBN 9780201095289. 62, 67, 74

[19] P. Croser and F. Ebel. *Pneumatik Grundstufe*. Springer, 1997. ISBN 3540620893. 18

[20] F. Daerden. *Conception and Realization of Pleated Pneumatic Artificial Muscles and their Use as Compliant Actuation Elements*. PhD thesis, Vrije Universiteit Brussel, Faculteit Toegepaste Wetenschappen, Vakgroep Werktuigkunde, July 1999. 17, 19, 81

[21] J. Denavit and R. S. Hartenberg. A kinematic notation for lower-pair mechanisms based on matrices. *Trans. ASME E, Journal of Applied Mechanics*, 22:215–221, June 1955. 61

[22] DIN Deutsches Institut für Normung e.V. Feuerlöschschläuche – Druckschläuche und Einbände für Pumpen und Feuerwehrfahrzeuge, 2008. Norm. DIN 14811. 128

[23] DIN Deutsches Institut für Normung e.V. Strahlrohre für die Brandbekämpfung – Teil 2: Hohlstrahlrohre PN16, 2010. Norm. DIN EN 150182-2. 128

[24] DIN Deutsches Institut für Normung e.V. Strahlrohre für die Brandbekämpfung – Teil 3: Strahlrohre mit Vollstrahl und/oder einem unveränderlichen Sprühstrahlwinkel PN 16, 2010. Norm. DIN EN 150182-3. 128

[25] DIN Deutsches Institut für Normung e.V. Industrieroboter – Sicherheitsanforderungen – Teil 2: Robotersysteme und Integration, 2011. Norm. ISO 10218-2:2011. 2

[26] DIN Deutsches Institut für Normung e.V. Roboter und Robotikgeräte - Sicherheitsanforderungen für nicht-industrielle Roboter - Nicht-medizinische Haushalts- und Assistenzroboter, 2011. Norm. prEN ISO 13842:2011. 2

[27] M. Doll, R. Neumann, and O. Sawodny. Energy efficient use of compressed air in pneumatic drive systems for motion tasks. In *Fluid Power and Mechatronics (FPM), 2011 International Conference on*, pages 340–345, August 2011. 18

[28] S. Dongjun, I. Sardellitti, and O. Khatib. A hybrid actuation approach for human-friendly robot design. In *Robotics and Automation, 2008. ICRA 2008. IEEE International Conference on*, pages 1747–1752, 2008. 19, 119

[29] H. Dresig and F. Holzweißig. *Maschinendynamik*. Springer, Berlin Heidelberg, 2005. ISBN 3540225463. 77

[30] C. Duriez. Real-time haptic simulation of medical procedures involving deformations and device-tissue interactions. eprint http://tel.archives-ouvertes.fr/docs/00/79/94/95/PDF/HDR_duriez.pdf, 2013. Université Lille. Habilitation thesis. 80

[31] M. Eder. Entwicklung und prototypische Umsetzung eines durch Fluidmuskeln angetriebenen wurmförmigen Arbeitsmechanismus mit interner Druckluft-Versorgung, December 2007. Technische Universität München. Diploma thesis. 29, 30, 32

[32] M. Eder, M. Karl, A. Knoll, and S. Riesner. Compliant worm-like robotic mechanism with decentrally controlled pneumatic artificial muscles. In *Innovative Engineering Systems (ICIES), 2012 First International Conference on*, pages 243–248, December 2012. 31, 46, 85, 88, 89, 92, 98, 99

[33] M. Eder, M. Karl, A. Knoll, and S. Riesner. Continuum Worm-like Robotic Mechanism with Decentral Control Architecture. In *Automation Science and Engineering (CASE 2014), IEEE International Conference on*, pages 866–871, August 2014. 54, 66, 91, 113, 116, 144

[34] M. Eder, M. Karl, F. Schultheiß, J. Schürmann, A. Knoll, and S. Riesner. Design of an inherently safe Worm-like Robot. In *Safety Security and Rescue Robotics (SSRR 2013), 11th IEEE International Symposium on*, October 2013. 56, 64, 72, 78, 84, 89, 90, 101, 105, 120

[35] K. Ehrlenspiel, A. Kiewert, and U. Lindemann. *Kostengünstig Entwickeln und Konstruieren: Kostenmanagement bei der integrierten Produktentwicklung*. VDI-Buch. Springer London, Limited, 2007. ISBN 9783540742234. 58

[36] H. Exner, R. Freitag, H. Geis, R. Lang, J. Oppolzer, P. Schwab, E. Sumpf, U. Ostendorff, and M. Reik. *Hydraulics, Basic Principles and Components*. Bosch Rexroth AG, Würzburg, 2011. ISBN 9783981487930. 18

[37] V. Falkenhahn, A. Hildebrandt, and O. Sawodny. Trajectory optimization of pneumatically actuated, redundant continuum manipulators. In *American Control Conference (ACC), 2014*, pages 4008–4013, June 2014. 122

[38] V. Falkenhahn, T. Mahl, A. Hildebrandt, R. Neumann, and O. Sawodny. Dynamic modeling of constant curvature continuum robots using the Euler-Lagrange formalism. In *Intelligent Robots and Systems (IROS), 2014 IEEE/RSJ International Conference on*, September 2014. accepted. 80

[39] P. Ferrara. Robot Arm. Patent Application, 2009. US2009/0182436A1. 20, 135

[40] Festo AG & Co. KG. Festo Fluidic Muscle DMSP/MAS. http://www.festo.com/rep/en_corp/assets/pdf/info_501_en.pdf, 2002. [Online; information brochure, accessed December 13, 2013]. 48, 82

[41] Festo AG & Co. KG. Fluidic Muscle. Established areas of application. http://www.festo.com/net/SupportPortal/Files/340811/Fluidic4_en.pdf, 2002. [Online; information brochure, accessed December 12, 2013]. 48, 87

[42] Festo AG & Co. KG. Airic's Arm: Robot Arm with Fluidic Muscles. http://www.festo.com/rep/en_corp/assets/pdf/Airics_arm_en.pdf, 2007. [Online; brochure number 50115 en 04/2011, accessed December 12, 2013]. 21

[43] Festo AG & Co. KG. Antriebsvorrichtung. Utility model, 2010. DE202010016983U1. 23

[44] Festo AG & Co. KG. Pneumatic lightweight structures. http://www.festo.com/rep/en_corp/assets/pdf/Pneumatic_lightweight_structures.pdf, 2010. [Online; brochure number 50139 en 04/2010, accessed December 17, 2013]. 135

[45] Festo AG & Co. KG. Adaptive gripper DHDG – Subject to change – 2011/01. http://www.festo.com/net/SupportPortal/Files/53886/AdaptiveGripper_DHDG_en.pdf, 2011. [Online; brochure number 135196 en 2011/01, accessed December 12, 2013]. 124

[46] Festo AG & Co. KG. Bionic Tripod 3.0. http://www.festo.com/net/ SupportPortal/Files/46268/Brosch_Tripod_3_en_RZ_110311_lo_einzel.pdf, 2011. [Online; brochure number 54766 en 4/2011, accessed December 12, 2013]. 23

[47] Festo AG & Co. KG. Robotino XT. http://www.indanc.com/downloads/pdf/Festo/Festo_Rob otino.pdf, 2011. [Online; brochure number 54762 en 04/2011, accessed December 16, 2013]. 124, 125

[48] Festo AG & Co. KG. Robotino XXT. http://www.festo-didactic.com/ov3/media/customers/1100/flyer_robotinoxxt_en.pdf, 2014. [Online; brochure, accessed June 4, 2014]. 124

[49] M. Fischer, R. Kaminski, R. Neumann, and A. Hildebrandt. Fluid-operated manipulator. Patent Application, 2012. US2012/0210818A1. 22, 135

[50] Y. Gao, F.-Y. Wang, and Z.-Q. Zhao. *Flexible Manipulators: Modeling, Analysis and Optimum Design*. Intelligent Systems Series. Academic Press, Elsevier, 2012. ISBN 9780123970367. 75

[51] R. H. Gaylord. Fluid actuated motor system and stroking device. Patent Application, 1958. US2844126A. 13, 16, 18

[52] I. Godage, E. Guglielmino, D. Branson, G. Medrano-Cerda, and D. Caldwell. Novel modal approach for kinematics of multisection continuum arms. In *Intelligent Robots and Systems (IROS), 2011 IEEE/RSJ International Conference on*, pages 1093–1098, September 2011. 63

[53] G. Granosik and J. Borenstein. The OmniTread serpentine robot with pneumatic joint actuation. In *Robot Motion and Control, 2005. RoMoCo '05. Proceedings of the Fifth International Workshop on*, pages 105–110, 2005. 136

[54] R. M. Greenhill. Braided sheath air muscle with substantially fixed perimeter bladder. Patent Application, 2007. GB2435308A. 18

[55] R. M. Greenhill, G. R. Walker, J. H. Elias, and M. P. Godden. Actuator system comprising an artificial air muscle. Patent Application, 2003. WO03/74238A1. 21, 22

[56] H.-W. Grollius. *Grundlagen der Pneumatik*. Hanser, München, 1997. ISBN 9783446229778. 18

[57] R. Ham, T. Sugar, B. Vanderborght, K. Hollander, and D. Lefeber. Compliant actuator designs. *Robotics Automation Magazine, IEEE*, 16(3):81–94, September 2009. 4, 7, 8

[58] M. W. Hannan and I. D. Walker. Kinematics and the Implementation of an Elephant's Trunk Manipulator and Other Continuum Style Robots. *Journal of Robotic Systems*, 20:45–63, 2003. 7

[59] H. Hauser, A. J. Ijspeert, R. M. Füchslin, R. Pfeifer, and W. Maass. Towards a Theoretical Foundation for Morphological Computation with Compliant Bodies. *Biol. Cybern.*, 105(5-6):355–370, Dec. 2011. 136

[60] H. Hauser, A. J. Ijspeert, R. M. Füchslin, R. Pfeifer, and W. Maass. The role of feedback in morphological computation with compliant bodies. *Biological Cybernetics*, 106:595–613, 2012. 136

[61] B. He, Z. Wang, Q. Li, H. Xie, and R. Shen. An Analytic Method for the Kinematics and Dynamics of a Multiple-Backbone Continuum Robot. *International Journal of Advanced Robotic Systems*, 10(84), 2013. 69

[62] S. Hesse. *Der Fluidic Muscle in der Anwendung: 150 Praxisbeispiele mit dem Pneumatischen Muskel*. Blue Digest on Automation, Esslingen, 2003. 48

[63] A. Hildebrandt, U. Böhle, and L. Blassmann. Faltenbalg. Patent Application, 2013. DE102011107580A1. 135

[64] A. Hildebrandt, R. Neumann, and O. Sawodny. Optimal System Design of SISO-Servopneumatic Positioning Drives. *Control Systems Technology, IEEE Transactions on*, 18(1):35–44, January 2010. 24

[65] A. Hildebrandt, O. Sawodny, R. Neumann, and A. Hartmann. Cascaded control concept of a robot with two degrees of freedom driven by four artificial pneumatic muscle actuators. In *American Control Conference, 2005. Proceedings of the 2005*, volume 1, pages 680–685, 2005. 19, 81, 82, 84

[66] D. Hisseine and B. Lohmann. Robust control for a flexible-link manipulator using sliding mode techniques and nonlinear H∞ control design methods. In *Robotics and Automation, 2001. Proceedings 2001 ICRA. IEEE International Conference on*, volume 4, pages 3865–3870, May 2001. 91

[67] IFR Statistical Department. World Robotics 2012: Industrial Robots: Statistics, Market Analysis, Forecasts, Case Studies and Profitability of Robot Investment, 2012. 1

[68] IFR Statistical Department. *World Robotics 2012: Service Robots: Statistics, Market Analysis, Forecasts, Case Studies*. VDMA, 2012. 1

[69] IFR Statistical Department. *World Robotics 2012: Service Robots: Statistics, Market Analysis, Forecasts, Case Studies*. VDMA, 2013. 1

[70] IFR Statistical Department. World Robotics 2013: Industrial Robots: Statistics, Market Analysis, Forecasts, Case Studies and Profitability of Robot Investment, 2013. 1

[71] G. Immega and M. Kukolj. Axially contractable actuator. Patent Application, 1990. US4939982. 18

[72] ISO International Organization for Standardization. Manipulating industrial robots - vocabulary, 12.09.2010. Norm. ISO/DIS 8373. 2, 3, 5

[73] H. Janocha. *Actuators – basics and applications*. Springer, Heidelberg, 2004. ISBN 3540615644. 10

[74] M. Jäntsch, S. Wittmeier, K. Dalamagkidis, A. Panos, F. Volkart, and A. Knoll. Anthrob – A Printed Anthropomimetic Robot. In *Humanoid Robots (Humanoids 2013). Proceedings. IEEE-RAS International Conference on*, pages 342–347, 2013. 21

[75] M. Jäntsch, S. Wittmeier, and A. Knoll. Distributed control for an anthropomimetic robot. In *Intelligent Robots and Systems (IROS), 2010 IEEE/RSJ International Conference on*, pages 5466–5471, 2010. 21

[76] C. Jessen, J. Sauer, and M.-M. Speckle. Modulare Antriebsvorrichtung. Patent, 2013. DE102012006610B3. 23, 135

[77] B. Jones and I. Walker. Kinematics for Multisection Continuum Robots. In *IEEE Transactions on Robotics*, volume 22, pages 43–55, February 2006. 63, 64

[78] B. Jones and I. Walker. Limiting-case Analysis of Continuum Trunk Kinematics. In *Robotics and Automation, 2007 IEEE International Conference on*, pages 1363–1368, April 2007. 63, 64

[79] T. R. Kane and D. A. Levinson. The Use of Kane's Dynamical Equations in robotics. *The International Journal of Robotics Research*, 2(3):3–21, September 1983. 75

[80] A. Karguth and O. Mollenhauer. Transmission mechanism. Patent Application, 2001. US2011/0266508A1. 21

[81] M. Karl. Control of a worm-like robot actuated by pneumatic artificial muscles, September 2012. Technische Universität München. Bachelor thesis. 85

[82] K. Kassow, E. H. Oestergaard, and K. Stoey. Programmable robot and user interface. Patent Application, 2007. WO2007/099511A2. 7, 20, 21

[83] T. Kerscher, J. Albiez, J.-M. Zollner, and R. Dillmann. Evaluation of the Dynamic Model of Fluidic Muscles using Quick-Release. In *Biomedical Robotics and Biomechatronics, 2006. BioRob 2006. The First IEEE/RAS-EMBS International Conference on*, pages 637–642, 2006. 82

[84] R. Kornbluh, R. Pelrine, J. Eckerle, and J. Joseph. Electrostrictive polymer artificial muscle actuators. In *Robotics and Automation, 1998. Proceedings. 1998 IEEE International Conference on*, volume 3, pages 2147–2154, 1998. 136

[85] KUKA Robot GmbH. LBR iiwa. The all-rounder. Sensitive, flexible and safe. http://www.kuka-labs.com/NR/rdonlyres/310A3034-1F44-47D7-8B37-F681BFCF7757/0/LBR_iiwa_Data_Sheet_EN_130715.pdf, 2014. Online; brochure, accessed June 5, 2014. 20

[86] P. X. M. La Hera. *Underactuated Mechanical Systems: Contributions to trajectory planning, analysis, and control*. PhD thesis, Department of Applied Physics and Electronics, Umeå University, 2011. ISBN 9789174591491. 39

[87] P. Labenda. Safeguarding trafficability of a wheeled, snake-like reconnaissance robot on rough terrain by a shared control system based on fuzzy logic. In *Industrial Technology (ICIT), 2013 IEEE International Conference on*, pages 187–192, 2013. 130

[88] F. Lange. Verfahren zur Kraftregelung. Patent Application, 2001. DE102009040194A1. 7

[89] T. Lens. *Physical Human-Robot Interaction with a Lightweight, Elastic Tendon Driven Robotic Arm*. PhD thesis, TU Darmstadt, 2013. 21

[90] P. Liljebäck, Ø. Stavdahl, and A. Beitnes. SnakeFighter – Development of a Water Hydraulic Fire Fighting Snake Robot. In *Control, Automation, Robotics and Vision, 2006. ICARCV '06. 9th International Conference on*, pages 1–6, 2006. 129

[91] P. Liljebäck, Ø. Stavdahl, and K. Y. Pettersen. Modular Pneumatic Snake Robot: 3D Modelling, Implementation And Control. In *IFAC Proceedings series, 16th IFAC World Congress*, pages 21–28, Amsterdam, 2006. Elsevier Science and Technology. ISBN 9780080451084. 129

[92] U. Lindemann. *Human Behavior in Design. Topic III: Methods, tools and prerequisites. Cognitive Outsourcing in the Conceptual Phase of the Design Process*. VDI-Buch. Springer, 2003. ISBN 9783662078112. 26

[93] U. Lindemann. *Methodische Entwicklung technischer Produkte*. VDI-Buch. Springer, 2009. ISBN 9783642014239. 27

[94] J. W. Login and A. Kascoutas. Method and apparatus for automatic opening and closing of a vehicle fuel door during robotic vehicle refueling. Patent Application, 2001. WO0153192A1. 125

[95] M. Löhrke. Cleaning system and cleaning process. Patent, 2013. US8528576B2. 126, 127

[96] S. Ma, G. Lan, Y. Tanabe, R. Sasaki, and K. Inoue. A Serpentine Robot Based on 3 DOF Coupled-driven Joint. In *Robotics and Biomimetics, 2004. ROBIO 2004. IEEE International Conference on*, pages 70–75, 2004. 136

[97] T. Mahl, A. Hildebrandt, and O. Sawodny. Forward Kinematics of a Compliant Pneumatically Actuated Redundant Manipulator. In *Industrial Electronics and Applications (ICIEA), 2012 7th IEEE Conference on*, pages 1267–1273, July 2012. 60, 63

[98] T. Mahl, A. Hildebrandt, and O. Sawodny. A Variable Curvature Continuum Kinematics for Kinematic Control of the Bionic Handling Assistant. *Robotics, IEEE Transactions on*, 30(4):935–949, August 2014. 63

[99] T. Mahl, A. E. Mayer, A. Hildebrandt, and O. Sawodny. A Variable Curvature Modeling Approach for Kinematic Control of Continuum Manipulators. In *American Control Conference (ACC), 2013*, pages 4945–4950, June 2013. 63

[100] A. Maity and S. Majumder. Serpentine robot locomotion: An implementation through piecewise sine function. In *Robotics and Biomimetics (ROBIO), 2011 IEEE International Conference on*, pages 1615–1620, 2011. 136

[101] A. Maity, S. Majumder, and S. Ghosh. An experimental hyper redundant serpentine robot. In *Systems Man and Cybernetics (SMC), 2010 IEEE International Conference on*, pages 3180–3185, 2010. 136

[102] D. Mankau. Pneumatisches oder hydraulisches Auslenkelement. Patent application, 2007. EP1865208A2. 135

[103] R. V. Martinez, C. R. Fish, X. Chen, and G. M. Whitesides. Elastomeric Origami: Programmable Paper-Elastomer Composites as Pneumatic Actuators. *Advanced Functional Materials*, 22(7):1376–1384, 2012. 135

[104] B. Mazzolai, L. Margheri, M. Cianchetti, P. Dario, and C. Laschi. Soft-robotic arm inspired by the octopus: II. From artificial requirements to innovative technological solutions. *Bioinspiration & Biomimetics*, 7(2):025005, 2012. 23

[105] J. M. McBean. Design and control of a voice coil actuated robot arm for human-robot interaction. Master's thesis, Massachusetts Institue of Technology, Massachusetts, USA, 2004. 9

[106] W. McMahan, V. Chitrakaran, M. Csencsits, D. Dawson, I. Walker, B. Jones, M. Pritts, D. Dienno, M. Grissom, and C. Rahn. Field trials and testing of the OctArm continuum manipulator. In *Robotics and Automation, 2006. ICRA 2006. Proceedings 2006 IEEE International Conference on*, pages 2336–2341, May 2006. 24

[107] K. Melo, J. Leon, A. di Zeo, V. Rueda, D. Roa, M. Parraga, D. Gonzalez, and L. Paez. The Modular Snake Robot Open Project: Turning Animal Functions into Engineering Tools. In *Safety Security and Rescue Robotics (SSRR 2013), 11th IEEE International Symposium on*, October 2013. 129, 130

[108] D. Merkle, B. Schrader, and M. Thomes. *Hydraulik Grundstufe*. Springer, Berlin, 1997. ISBN 3540620915. 18

[109] A. P. M. M. Moelands and H. Schutte. Two-wire bus-system comprising a clock wire and a data wire for interconnecting a number of stations. Patent, 1981. US4689740. 93

[110] A. H. Morin. Elastic diaphragm. Patent Application, 1953. US2642091. 18

[111] M. Nakamura, S. Goto, and N. Kyura. *Mechatronic Servo System Control – Problems in Industries and their Theoretical Solutions*. Springer, Berlin, 2004. ISBN 3540210962. 7

[112] M. A. Nasseri, M. Eder, E. Dean-Leon, S. Nair, D. Zapp, M. Maier, C. P. Lohmann, and A. Knoll. The Introduction of a New Robot for Assistance in Ophthalmic Surgery. In *Engineering in Medicine and Biology Society (EMBC'13), 35th Annual IEEE International Conference of*, July 2013. 9

[113] M. A. Nasseri, M. Eder, D. Eberts, S. Nair, M. Maier, D. Zapp, C. P. Lohmann, and A. Knoll. Kinematics and Dynamics Analysis of a Hybrid Parallel-Serial Micromanipulator Designed for Biomedical Applications. In *Advanced Intelligent Mechatronics (AIM2013), Proceedings of the International Conference on*, July 2013. 9

[114] S. Neppalli, M. A. Csencsits, B. A. Jones, and I. D. Walker. Closed-Form Inverse Kinematics for Continuum Manipulators. *Advanced Robotics*, 23(15):2077–2091, 2009. 7, 63, 69, 74

[115] H. Ohno and S. Hirose. Design of slim slime robot and its gait of locomotion. In *Intelligent Robots and Systems, 2001. Proceedings. 2001 IEEE/RSJ International Conference on*, volume 2, pages 707–715, 2001. 129

[116] R. Olfati-Saber. *Nonlinear Control of Underactuated Mechanical Systems with Application to Robotics and Aerospace Vehicles*. PhD thesis, Department of Electrical Engineering and Computer Science, Massachusetts Institute of Technology, 2001. 39

[117] C. Onal and D. Rus. A modular approach to soft robots. In *Biomedical Robotics and Biomechatronics (BioRob), 2012 4th IEEE RAS EMBS International Conference on*, pages 1038–1045, June 2012. 23

[118] Parker Hannifin Corp. MD PRO Miniature Proportional Valve. http://www.parker.com/literature/Literature%20Files/Precision%20Fluidics%20Division/UpdatedFiles/MDPRO.pdf, 2014. Online; brochure, accessed June 5, 2014. 45

[119] C. Paul. Morphological computation: A basis for the analysis of morphology and control requirements. *Robotics and Autonomous Systems*, 54(8):619–630, 2006. Morphology, Control and Passive Dynamics. 136

[120] C. Pein. Piezoventil. Patent, 2012. DE102012001775B3. 135

[121] R. Pfeifer and G. Gómez. Morphological computation – connecting brain, body, and environment. In B. Sendhoff, E. Körner, O. Sporns, H. Ritter, and K. Doya, editors, *Creating Brain-Like Intelligence*, volume 5436 of *Lecture Notes in Computer Science*, pages 66–83. Springer Berlin Heidelberg, 2009. ISBN 9783642006159. 136

[122] Q. T. Pham, J. Poole, C. Prest, J. Stevick, and T. A. Waniuk. Layer-by-layer construction with bulk metallic glasses. Patent application, 2013. US20130309121A1. 135

[123] J. Poole, C. Prest, J. Stevick, and T. A. Waniuk. Layer-by-layer construction with bulk metallic glasses. Patent application, 2013. US20130306198A1. 135

[124] V. Potkonjak, B. Svetozarevic, K. Jovanovic, and O. Holland. The Puller-Follower Control of Compliant and Noncompliant Antagonistic Tendon Drives in Robotic Systems. *International Journal of Advanced Robotic Systems*, 8(5):143–155, 2011. 21

[125] G. Pratt and M. Williamson. Series elastic actuators. In *Intelligent Robots and Systems 95. 'Human Robot Interaction and Cooperative Robots', Proceedings. 1995 IEEE/RSJ International Conference on*, volume 1, pages 399–406, August 1995. 82

[126] F. Preisach. Über die magnetische Nachwirkung. In *Zeitschrift für Physik*, volume 94, pages 277–302. Springer, 1935. ISBN 3540615644. 91

[127] R. F. Reinhart and M. Rolf. Learning versatile sensorimotor coordination with goal babbling and neural associative dynamics. In *Development and Learning and Epigenetic Robotics (ICDL), 2013 IEEE Third Joint International Conference on*, pages 1–7, August 2013. 70

[128] S. Riesner, M. Eder, and B. Vaksic. Vorrichtung zur sicheren Kollaboration zwischen Mensch und Roboter. Patent Application, 2013. DE102012108418A1. 2

[129] O. Rödig. Automatic fuel filling installation. Patent Application, 2001. WO0140104A1. 125

[130] M. Rolf. Goal babbling with unknown ranges: A direction-sampling approach. In *Development and Learning and Epigenetic Robotics (ICDL), 2013 IEEE Third Joint International Conference on*, pages 1–7, August 2013. 70

[131] M. Rolf and J. Steil. Constant curvature continuum kinematics as fast approximate model for the Bionic Handling Assistant. In *Intelligent Robots and Systems (IROS), 2012 IEEE/RSJ International Conference on*, pages 3440–3446, October 2012. 7, 63, 64, 65, 66, 80

[132] M. Rolf, J. Steil, and M. Gienger. Online Goal Babbling for rapid bootstrapping of inverse models in high dimensions. In *Development and Learning (ICDL), 2011 IEEE International Conference on*, volume 2, pages 1–8, 2011. 70, 71

[133] W. Rone and P. Ben-Tzvi. Continuum Robot Dynamics Utilizing the Principle of Virtual Power. *Robotics, IEEE Transactions on*, 30(1):275–287, February 2014. 75

[134] A. Sabanovic, L. Fridman, and S. Spurgeon. *Variable structure systems: from principles to implementation*. Institution of Electrical Engineers, London, 2004. ISBN 9781849190008. 91

[135] B. Schrauwen, D. Verstraeten, and J. V. Campenhout. An overview of reservoir computing: theory, applications and implementations. In *Proceedings of the 15th European Symposium on Artificial Neural Networks*, pages 471–482, 2007. 136

[136] S. Schuberth. Inverse Kinematik eines pneumatisch gesteuerten Roboterarms, September 2013. Technische Universität München. Bachelor thesis. 68

[137] F. Schultheiß. Modellierung, Reglerentwurf und Simulation eines PAM-aktuierten Roboterarms, June 2013. Technische Universität München. Semesterarbeit. 68, 118, 120

[138] J. Schürmann. Dynamic analysis and simulation of a modular worm-like robot comprising 3 segments, July 2013. Technische Universität München. Bachelor thesis. 79

[139] M. Sfakiotakis, A. Kazakidi, N. Pateromichelakis, J. Ekaterinaris, and D. Tsakiris. Robotic underwater propulsion inspired by the octopus multi-arm swimming. In *Robotics and Automation (ICRA), 2012 IEEE International Conference on*, pages 3833–3839, May 2012. 23

[140] R. F. Shepherd, F. Ilievski, W. Choi, S. A. Morin, A. A. Stokes, A. D. Mazzeo, X. Chen, M. Wang, and G. M. Whitesides. Multigait soft robot. *Proceedings of the National Academy of Sciences*, 2011. eprint http://www.pnas.org/content/early/2011/11/21/1116564108.full.pdf+html. 23

[141] D. Shin, F. Seitz, O. Khatib, and M. Cutkosky. Analysis of torque capacities in hybrid actuation for human-friendly robot design. In *Robotics and Automation (ICRA), 2010 IEEE International Conference on*, pages 799–804, 2010. 19

[142] B. Siciliano. Kinematic control of redundant robot manipulators: A tutorial. *Journal of Intelligent and Robotic Systems*, 3(3):201–212, 1990. 63

[143] B. Siciliano and O. Khatib. *Springer Handbook of Robotics*. Springer, 2008. ISBN 9783540239574. 67

[144] J.-J. E. Slotine and W. Li. *Applied Nonlinear Control*. Prentice Hall, first edition, 1991. ISBN 0130408905. 91

[145] M. Smaoui, X. Brun, and D. Thomasset. A Robust Differentiator-Controller Design for an Electropneumatic System. In *Decision and Control, 2005 and 2005 European Control Conference. CDC-ECC '05. 44th IEEE Conference on*, pages 4385–4390, December 2005. 91

[146] M. Smaoui, X. Brun, and D. Thomasset. Systematic control of an electropneumatic system: integrator backstepping and sliding mode control. *Control Systems Technology, IEEE Transactions on*, 14(5):905–913, September 2006. 91

[147] M. M. J. Tavera. *Mechatronics conceptual design of a fire fighting robot*. PhD thesis, Universidade Federal do Rio de Janeiro, COPPE, Rio de Janeiro, 2008. 128

[148] R. Tedrake. Underactuated Robotics: Learning, Planning, and Control for Efficient and Agile Machines. *Course Notes for MIT 6.832*, 2009. Massachusetts Institute of Technology. 39

[149] M. B. Thomas. *Advanced Servo Control of a Pneumatic Actuator*. PhD thesis, Ohio State University, 2003. 91

[150] A. Transeth and K. Pettersen. Developments in Snake Robot Modeling and Locomotion. In *Control, Automation, Robotics and Vision, 2006. ICARCV '06. 9th International Conference on*, pages 1–8, 2006. 129

[151] D. Trivedi, A. Lotfi, and C. Rahn. Geometrically Exact Models for Soft Robotic Manipulators. *Robotics, IEEE Transactions on*, 24(4):773–780, August 2008. 13, 75

[152] D. Trivedi, C. D. Rahn, W. M. Kier, and I. D. Walker. Soft robotics: Biological inspiration, state of the art, and future research. *Applied Bionics and Biomechanics*, 5(3):99–117, September 2008. 33

[153] V. Utkin. Variable structure systems with sliding modes. *Automatic Control, IEEE Transactions on*, 22(2):212–222, April 1977. 91

[154] D. Verstraeten, B. Schrauwen, M. D'Haene, and D. Stroobandt. 2007 Special Issue: An Experimental Unification of Reservoir Computing Methods. *Neural Networks*, 20(3):391–403, April 2007. 136

[155] V. Vibhute and A. Kshirsagar. Identification of Hysteresis and Relaxation Parameters in Stretch Sensor. In *International Journal of Advanced Electrical and Electronics Engineering (IJAEEE)*, volume 1, pages 15–22, 2012. 91

[156] R.-J. Wang and H.-P. Huang. Active Variable Stiffness Elastic Actuator: design and application for safe physical human-robot interaction. In *Robotics and Biomimetics (ROBIO), 2010 IEEE International Conference on*, pages 1417–1422, December 2010. 3

[157] K. Watanabe, H. Nagayasu, N. Kawakami, and S. Tachi. Mechanical Compliance Control System for a pneumatic robot arm. In *SICE Annual Conference, 2008*, pages 2789–2794, 2008. 10

[158] R. J. Webster and B. A. Jones. Design and Kinematic Modeling of Constant Curvature Continuum Robots: A Review. *The International Journal of Robotics Research*, 2010. 63

[159] J. M. Yarlott. Fluid actuator. Patent Application, 1972. US3645173A. 18

[160] K. Young, V. Utkin, and U. Ozguner. A control engineer's guide to sliding mode control. In *IEEE Transactions on Control Systems Technology*, volume 7, pages 328–342, May 1999. 91

[161] M. Zeller, R. Sharma, and K. Schulten. Motion Planning of a Pneumatic Robot Using a Neural Network. *Control Systems, IEEE*, 17(3):89–98, June 1997. 80

[162] H. Zhang, J. Gonzalez-Gomez, Z. Me, S. Cheng, and J. Zhang. Development of a low-cost flexible modular robot GZ-I. In *Advanced Intelligent Mechatronics, 2008. AIM 2008. IEEE/ASME International Conference on*, pages 223–228, 2008. 135

[163] L. Zhang, Q. Huang, Y. Li, J. Gao, H. Li, and L. Wu. Research and development of throwable miniature reconnaissance robot. In *Mechatronics and Automation (ICMA), 2012 International Conference on*, pages 1254–1259, 2012. 130

[164] C. Zheng. Implementation of Reactive Control for a Miniature Surveillance Robot. In *Information Technology and Computer Science, 2009. ITCS 2009. International Conference on*, volume 2, pages 510–513, 2009. 130

[165] C. Zheng. The control system and experiments of a miniature autonomous reconnaissance robot. In *Automation and Logistics (ICAL), 2011 IEEE International Conference on*, pages 131–136, 2011. 130

[166] J. Zhou and Y. Yu. Simulation and control of reconfigurable modular robot arm based on close-loop real-time feedback. In *Computer Engineering and Technology (ICCET), 2010 2nd International Conference on*, volume 3, pages V3–35–V3–40, 2010. 136